VYSOKÉ UČENÍ TECHNICKÉ V BRNĚ
BRNO UNIVERSITY OF TECHNOLOGY

FAKULTA STROJNÍHO INŽENÝRSTVÍ
ÚSTAV MATERIÁLOVÝCH VĚD A INŽENÝRSTVÍ

FACULTY OF MECHANICAL ENGINEERING
INSTITUTE OF MATERIALS SCIENCE AND ENGINEERING

PŘÍPRAVA ELEKTROKERAMICKÝCH MATERIÁLŮ PRO POKROČILÉ APLIKACE

PROCESSING OF ELECTROCERAMIC MATERIALS FOR ADVANCED APPLICATIONS

DOKTORSKÁ PRÁCE
DOCTORAL THESIS

AUTOR PRÁCE Ing. MARTIN KACHLÍK
AUTHOR

VEDOUCÍ PRÁCE prof. RNDr. KAREL MACA, Dr.
SUPERVISOR

ŠKOLITEL SPECIALISTA Ing. KLÁRA ČÁSTKOVÁ, Ph.D.
SUPERVISOR SPECIALIST

BRNO 2015

ABSTRAKT

Disertační práce se zabývá přípravou pokročilých keramických materiálů se zajímavými fyzikálními vlastnostmi. Materiály, připravené v rámci této práce, byly vyrobeny tuho-fázovými popř. hydrotermálními syntézami. První ze zkoumaných materiálů je elektrokeramika $EuTiO_3$ s perovskitovou mřížkou. Absence termodynamických dat tohoto systému vedla k rozsáhlému experimentálnímu výzkumu vhodných podmínek jeho přípravy. Tři směsi různých práškových prekurzorů (Eu_2O_3 s Ti_2O_3 nebo TiO_2 – rutil či anatas) byly homogenizovány mletím v planetovém mlýnu a formovány izostatickým tlakem 300 MPa. Vzniklé keramické polotovary diskového tvaru byly slinovány konvenčními metodami v redukčních atmosférách (Ar + 7 % H_2 nebo pouze čistý H_2) popř. pokročilou slinovací metodou Spark Plasma Sintering (SPS). Následně byl studován vliv slinovací metody, teploty, složení atmosféry a prodlevy na finální hustotu a fázovou čistotu vzorků. Tento výzkum vyústil v úspěšnou přípravu jednofázové $EuTiO_3$ objemové keramiky s relativní hustotou vyšší než 95 % teoretické hustoty (%TH). S ohledem na dostupnou literaturu jsou tyto materiály jedinými publikovanými vzorky fázově čisté $EuTiO_3$ keramiky s tak nízkou porozitou. Důležitost těchto výsledků je podložena čtyřmi publikacemi v impaktovaných časopisech, kde byly vlastnosti měřené na těchto vzorcích prezentovány. Spektra infračervené odrazivosti byla porovnána s výsledky v literatuře. Byla tak demonstrována nezbytnost fázově čistých vzorků s minimálním porozitou pro měření jejich reálných (neovlivněných) fyzikálních vlastností.

Další výzkum byl zaměřen na hydrotermální syntézu (HTS) keramického prášku $Eu_{0,5}Na_{0,5}TiO_3$. Prezentované HTS byly uskutečněny ve vysoce zásaditém prostředí vodných roztoků NaOH nebo KOH při teplotách 220 – 250 °C. Experimenty s různými koncentracemi prekurzorů ($EuCl_3$ a $TiCl_4$) a redukčních činidel vedly k přípravě jednofázového práškového perovskitu $Eu_{0,5}Na_{0,5}TiO_3$ s krychlovými částicemi s rozměry pod 1 μm.

Jiný titaničitan - $MgTiO_3$ – byl syntetizován tuho-fázovou reakcí směsi práškových prekurzorů MgO a TiO_2. Směsi byly mechanicky aktivovány v kulovém mlýnu po dobu 0, 10, 40, 80 nebo 160 min. Keramická tělesa byla formována izostatickým tlakem 300 MPa a slinována pomocí dvou různých přístupů. První sada vzorků byla slinována metodou Two-step Sintering (TSS) na teplotách 1300 °C (30 min) a následně 1200 °C (20 h). Druhá část vzorků byla slinována nejprve konvenčně při 1300 °C popř. 1400 °C po dobu 30 min a následně ještě pomocí metody Hot Isostatic Press (HIP) na 1200 °C popř. 1280 °C. V případě HIP-ovaných vzorků při 1280 °C po 3 hodiny v inertní Ar atmosféře o tlaku 200 MPa byly získány fázově čisté keramické vzorky $MgTiO_3$ s relativní hustotou nad 93 %TH.

Poslední z prezentovaných materiálů je $Ba(Ca)Ti(Zr)O_3$ bezolovnatá piezokeramika, která byla připravena tuho-fázovou reakcí práškových směsí mletých v planetovém kulovém mlýnu za rozdílných podmínek. Keramická tělesa lisovaná izostatickým tlakem (300 MPa) byla dále zhutněna beztlakým slinováním na teplotách 1200, 1300, 1400 popř. 1500 °C po dobu 1 h na vzduchu. Byly studovány potřebné podmínky pro přípravu jednofázové perovskitové $Ba_{0,85}Ca_{0,15}Ti_{0,9}Zr_{0,1}O_3$ keramiky s požadovanou mikrostrukturou. Úspěšně tak byly připraveny vzorky fázově čisté $Ba(Ca)Ti(Zr)O_3$ keramiky o relativní hustotě až 96 %TH.

Prezentované výsledky potvrzují význam volby vhodné metody výroby a potřebných parametrů k získání pokročilých elektrokeramických materiálů s požadovanou mikrostrukturou i fázovým složením a tudíž i pro správné stanovení jejich fyzikálních vlastností.

ABSTRACT

The doctoral thesis is focused on processing of advanced ceramic materials with interesting physical properties. The materials were prepared by solid-state resp. hydrothermal syntheses. The first investigated material described in this work is $EuTiO_3$ perovskite ceramics. Absence of thermodynamic data of this system led to extensive experimental research of proper processing conditions. Three mixtures of different powder precursors (Eu_2O_3 with Ti_2O_3 resp. TiO_2 – rutile or anatase) were homogenized by planetary ball mill and formed by isostatic pressure of 300 MPa. These cylindrical green bodies were sintered conventionally in reducing atmospheres (Ar + 7 % H_2 resp. pure H_2) or by Spark Plasma Sintering (SPS). The influence of the sintering technique, temperature, atmosphere composition and dwell time on final density and phase purity was discussed. The investigation resulted in successful processing of phase pure $EuTiO_3$ ceramic with relative density higher than 95 % of theoretical density (%TD). According author's best knowledge, it is up to now the best bulk $EuTiO_3$ ceramic sample. The importance of this achievement is also declared by four publications in respected journals where the properties of these samples were presented. The infra-red reflectivity spectra of prepared materials were compared with data from literature. It was proven that only single phase samples with low content of porosity are suitable for establishing their real (undistorted) physical properties.

The next research was aimed on processing of $Eu_{0.5}Na_{0.5}TiO_3$ ceramics by hydrothermal syntheses (HTS). The HTS were performed in highly alkaline environment of NaOH resp. KOH solution at temperature range 220 – 250 °C. The experiments with varied precursors ($EuCl_3$ and $TiCl_4$) and reductant agent concentrations led to processing of pure $Eu_{0.5}Na_{0.5}TiO_3$ perovskite ceramic powder with submicron cubic particles.

Another titanate - $MgTiO_3$ - was synthetized by solid-state reaction from MgO and TiO_2 powder mixtures. The mixtures were mechanically activated in ball mill for 0, 10, 40, 80 resp. 160 min. The green bodies were formed by isostatic pressure of 300 MPa and sintered by two different approaches. The first batch of samples was sintered by two-step sintering technique at 1300 °C (30 min) and 1200 °C (20 h). The second set was sintered conventionally at 1300 °C resp. 1400 °C for 30 min and post-sintered by Hot Isostatic Press (HIP) at 1200 °C resp. 1280 °C. The phase pure $MgTiO_3$ samples with relative density higher than 93 %TD were reached after post-sintering by HIP at 1280 °C for 3 hours in Ar atmosphere and pressure of 200 MPa.

The last studied material was $Ba(Ca)Ti(Zr)O_3$ lead-free piezoceramics, which was prepared by solid-state reaction from powder mixtures milled by planetary ball mill at different conditions. The pressure-less sintering of isostatically pressed bodies (300 MPa) at 1200, 1300, 1400 resp. 1500 °C for 1 h in air was performed. The processing condition needed for single phase perovskite $Ba_{0.85}Ca_{0.15}Ti_{0.9}Zr_{0.1}O_3$ ceramics with required microstructure were studied. The single phase $Ba(Ca)Ti(Zr)O_3$ sample with relative density 96 %TD was successfully prepared.

Our results proved the importance of careful choice of the processing techniques and their variables for reaching of desired microstructure and phase composition of advanced electroceramics and therefore for proper evaluation of their physical properties.

KLÍČOVÁ SLOVA
Pokročilá keramika, elektrokeramika, elektromagnetické vlastnosti, syntéza v tuhé fázi, slinování

KEY WORDS
Advanced ceramics, electroceramics, electromagnetic characteristics, solid-state reaction, sintering

KACHLÍK, M. *Příprava elektrokeramických materiálů pro pokročilé aplikace.* Brno: Vysoké učení technické v Brně, Fakulta strojního inženýrství, 2015. 98s. Vedoucí disertační práce prof. RNDr. Karel Maca, Dr.

KACHLÍK, M. *Processing of electroceramic materials for advanced applications.* Brno: Brno University of Technology, Faculty of Mechanical Engineering, 2015. 98p. Supervisor of dissertation thesis prof. RNDr. Karel Maca, Dr.

PODĚKOVÁNÍ
Autor práce děkuje za aktivní pracovní i osobní vedení svému školiteli Prof. RNDr. Karlu Macovi, Dr. a školiteli specialistovi Ing. Kláře Částkové, Ph.D. Současně se poděkování vztahuje na celý kolektiv Odboru keramiky a polymerů na Ústavu materiálových věd a inženýrství na FSI VUT v Brně a všem spolupracujícím českým i zahraničním institucím za příkladnou duševní, fyzickou i materiální pomoc při řešení této disertační práce.

ACKNOWLEDGMENT
The author of this thesis thanks to his supervisor Prof. RNDr. Karel Maca, Dr. As well as to supervisor specialist Ing. Klára Částková, Ph.D. for active professional and personal leadership. The gratitude belongs also to whole team of the Department of Ceramics and Polymers at the Institute of Material Engineering - Faculty of Mechanical Engineering at Brno University of Technology and to all collaborated foreign institutions for mental, physical and material support.

PROHLÁŠENÍ
Prohlašuji, že jsem disertační práci vypracoval samostatně, a že všechny použité literární zdroje jsem správně a úplně citoval. Dizertační práce je z hlediska obsahu majetkem Fakulty strojní VUT v Brně a může být využita ke komerčním účelům jen se souhlasem vedoucího disertační práce a děkana FSI VUT.

……..
podpis doktoranda

Contents

1. Introduction

In the last decades the importance of ferroelectric (energetically independent FeRAM memories, capacitors, sensors, etc.) and ferromagnetic (artificial magnets, hard drives, etc.) materials in electronic applications increased significantly. The materials providing both of these polarization types (together with magnetoelectric effect – the ability to control electric polarization by magnetic field and conversely) in a single phase are called multiferroics (multiferroic magnetoelectrics). Such materials would lead to new generation of electronic devices with increased memory capacity and enhanced speed (future substitute of semiconducting RAM memories). The problem is that only a few known materials exhibit at least partially these characteristics. Some of them are missing one of the spontaneous polarization type (ferroelectricity or/and ferromagneticity), the others have only weak (or even none) magnetoelectric effect or the working temperature is too low for common applications. As it follows from the physical background, ferroelectric and ferromagnetic behaviour can only rarely exist together. For example, the transition metal d electrons (which are essential for magnetism) reduce the tendency for off-center ferroelectric distortion. Consequently, an additional driving force must be present for ferromagnetism and ferroelectricity to occur simultaneously.

Although these materials are far away from everyday application, studying of their properties help to understand of their origin and possible interactions. Deeper knowledge of these physical phenomena would lead to more precise modelling and designing of new ceramic materials or future electronic devices.

This work is organized by a following manner:

- Theoretical part
- Experimental background
- Experimental results and their discussion

The main benefit of this work would be exploiting of the experimental infrastructure and experience for producing of various modern electroceramics materials with improved microstructure. Such materials are then used for measuring of their undistorted functional properties (properties which are not influenced by microstructural and phase imperfections).

2. Theory and terminology

2.1. Electric properties

2.1.1. Insulators

The word "insulator" has an origin in the Latin word "insula", which means island. Whereas in conductors the movement of charges is easy, in the insulators the charges are prisoned in the islands. So as an electric "insulator" can be called a material, which has so small amount of current carriers (free electrons or ions) or their movement is so restricted, that we consider them as electrically non-conducting materials. On the other hand, thanks to this limited amount of the charge carriers, it is still possible to measure their resistivity respective conductivity.

From that point of view the most important property of this brand of materials is the resistivity ρ (eq. 1; where E [V·m^{-1}] is intensity of electric field in the certain point of the insulator or conductor, J [A·m^{-2}] is current density in the same point) [1]

$$\rho = \frac{E}{J}\ [\Omega m]. \tag{1}$$

Whereas resistivity ρ is the intense material property, resistance R is the characteristic of the specific electronic device (eq. 2; where L [m] is the length of measured sample, S [m^2] is the surface area of the cross-section perpendicular to the length of the sample)

$$R = \rho \cdot \frac{L}{S}\ [\Omega]. \tag{2}$$

There is nothing ideal in the nature and the insulators are no exception. Resistivity vary with a temperature, so insulating materials need to be chosen for exact application considering e.g. working temperature, design of device and the economic aspects. This bring us to the subgroups of insulators, where the resistivity is not single required property.

2.1.2. Dielectrics (Paraelectrics)

These materials are basically insulators with capability of polarization by an external electric field. This polarization disappears after removal of the external field. As it will be describe later in this chapter, at least very weak ability of polarization has every non-conducting material, but the term "dielectrics" is usually used only in case of materials, where the potency of polarization is important for their applications.

First research of such materials began in the work of Michael Faraday in 1837 [1]. He noticed that amount of charge in capacitors (in case of same input parameters) is changing with different types of material (dielectrics) between its

electrodes. Faraday named this characteristic as dielectric constant, but it is called relative permittivity ε_r [-] now. Its value indicates how many times the capacity C [F] of capacitor is increased with presence of a dielectric instead of vacuum between electrodes (eq. 3; where ε_0 is permittivity of vacuum ($\approx 8.85 \cdot 10^{-12}$ F·m^{-1}), S [m^2] is common surface of both electrodes and d [m] is the perpendicular distance between them) [1, 2]

$$\mathrm{C} = \varepsilon_\mathrm{r} \cdot \varepsilon_0 \cdot \frac{\mathrm{S}}{\mathrm{d}} \ [\mathrm{F}]. \tag{3}$$

The relative permittivity is also possible to express as a ratio of (absolute) permittivity ε [F·m^{-1}] and permittivity of vacuum ε_0 [F·m^{-1}]

$$\varepsilon_\mathrm{r} = \frac{\varepsilon}{\varepsilon_0} \ [-]. \tag{4}$$

Another material characteristic describing the polarizability is the (di)electric susceptibility χ_e [-]. Large value of susceptibility reflects great material ability of polarization in the response to an external electric field. The relation between dielectric susceptibility and relative permittivity is given by equation 5. It means that for vacuum this value is equal zero

$$\chi_\mathrm{e} = \varepsilon_\mathrm{r} - 1 \ [-]. \tag{5}$$

The basic relationships between polarization density P [C·m^{-2}], intensity of electric field E [V·m^{-1}], electric induction (electric displacement) D [C·m^{-2}], relative permeability ε_r [-] and electric susceptibility χ_e [-] are given by following equations (Eq. 6 and 7)

$$\mathrm{P} = \varepsilon_\mathrm{o} \cdot \mathrm{E} \cdot \chi_\mathrm{e} \ [\mathrm{C} \cdot \mathrm{m}^{-2}], \tag{6}$$

$$\mathrm{D} = \varepsilon_\mathrm{o} \cdot \mathrm{E} + \mathrm{P} = \varepsilon_\mathrm{o} \cdot \mathrm{E} \cdot \left(1 + \chi_\mathrm{e}\right) = \varepsilon \cdot \mathrm{E} \ [\mathrm{C} \cdot \mathrm{m}^{-2}]. \tag{7}$$

From the point of view of the atomic, molecular and micro-structure there are several types of dielectric polarization:

Electronic

By influence of an external electric field there is a displacement between atomic nucleus and its electrons (see Fig. 1a). Because all materials contain atoms, this effect occurs in each material. On the other hand macroscopic polarization is possible only in case of covalently bonded and pure materials, which don't have any permanent dipoles in the structure. Anyway the formed dipole moments are very small as well as the resulting polarization [3].

Ionic

Material with ionic bond can by polarized by ionic mechanism, therefore it is common polarization mechanism in most of the ceramic materials. After placing into the external electric field, the bonds between the ions are elastically deformed (see Fig. 1b). The contribution to polarization capability caused by this phenomenon is usually very small as well as displacement of the ions from the equilibrium positions. Even such a little displacement can change the overall dimensions of a material [3].

Dipolar

Generally it is being observed in dielectrics, which have permanent dipoles in their structures. Application of an external electric field leads to alignment of these dipoles according the orientation of the field (see Fig. 1c). This strong type of polarization (also called "Orientation" or "Molecular") is unusual in the ceramic materials, where reorientation would lead to destruction of their crystal structure. But there exist very important exceptions for example in some of the perovskite ceramics [3].

Interfacial

This type of polarization, sometimes called "Space charge", can occur in the non-conducting materials with conductive impurities or inclusions (conductive second phase). Other possibility of interfacial polarization is conducting material, where charge is prevented from "long distance movement" for example by grain or phase boundaries (see Fig. 1d). When such a dielectrics are placed into an electric field, charge (electron) pile up is established in agreement with the direction of the field [3].

Dielectric losses

The phenomena occurs during polarization of dielectrics, when part of the energy given by external electric field is changed into the heat. In general, relative permittivity ε_r [-] is a complex number with real part ε_r', which is normally used in calculations of capacitor characteristic in static electric field. Imaginary part ε_r'' represents dielectric losses and its influence has to be consider especially in alternating electric field (Eq. 8).

$$\varepsilon_r = \varepsilon_r' - j \cdot \varepsilon_r'' \; [-] \tag{8}$$

For example, a capacitor connected in an alternative current (AC) circuit is alternately charged and discharged each half cycle. During the change of polarity of the electrodes, the charges must be displaced through the dielectric first in one direction and then in the other.

Dielectric losses depend on the material and on frequency of AC. Heating through dielectric losses are widely employed industrially for thermosetting glues or plastics before moulding, for drying of a lumber, etc.

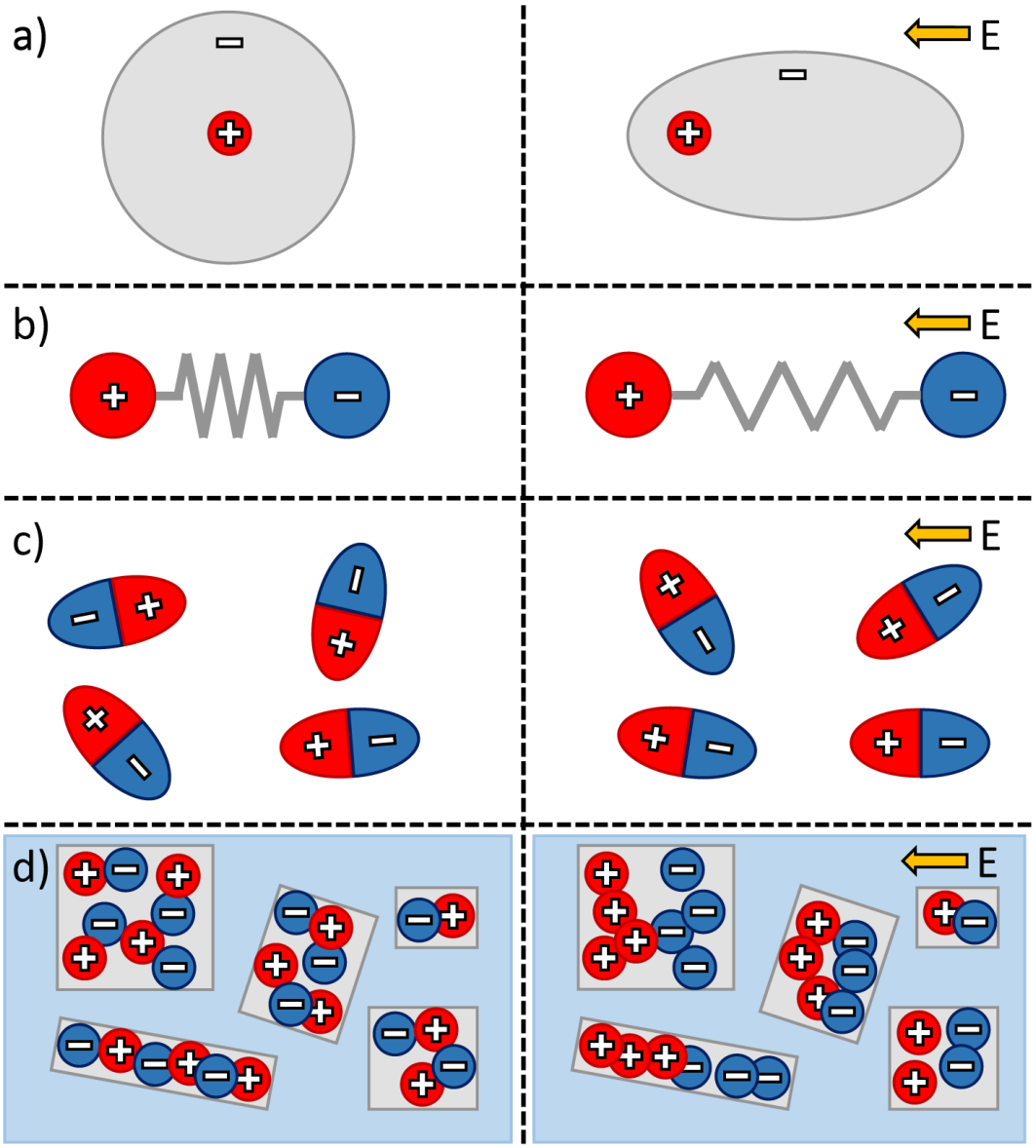

Fig. 1 Electronic (a), Ionic (b), Dipolar (c) and Interfacial (d) polarization mechanisms in dielectric materials.

2.1.3. Piezoelectrics

The word “piezo” comes from Greek and means “push” or “squeeze”. The effect known as piezoelectricity was discovered by brothers Pierre and Jacques Curie in 1880 [4].

Piezoelectricity is reversible mechanic-electrical phenomenon, which is divided into two effects - “direct effect” and “inverse effect” (see Fig. 2). In the case of direct effect, the applied elastic deformation (change of dimension) causes polarization (electric field creation). The inverse effect (also called electrostriction) describes phenomenon, when an external electric field applied to a material causes a change of its dimensions (together with polarization) [5].

Piezoelectrics are sub-group of dielectric materials, which crystallographic system does not have the centrum of symmetry [3]. This asymmetry of crystals is also the reason of anisotropic behaviour of piezoelectric materials. The quantities and constants of single crystal materials need to be consider as a tensors (direction-depended characteristic) [6]. Mathematical expressions of these phenomena are difficult, but they can be simplified for polycrystalline materials with homogenous microstructure (see Eq. 9 and 10; where *d* is piezoelectric charge constant [$C \cdot N^{-1}$], σ is the mechanical stress [$N \cdot m^{-2}$], ε^{σ} is the dielectric permittivity at constant stress [$F \cdot m^{-1}$] and s^{E} is the specific elastic compliance at constant electric field [$m^2 \cdot N^{-1}$])

$$D = d \cdot \sigma + \varepsilon^{\sigma} \cdot E \, [C \cdot m^{-2}], \tag{9}$$

$$S = s^{E} \cdot \sigma + d \cdot E \, [-]. \tag{10}$$

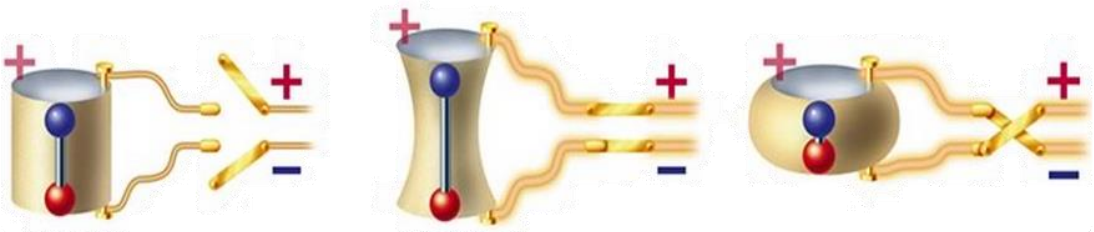

Fig. 2 The inverse piezoelectric effect.

Piezoelectricity is exploited in many devices such microphones, speakers, sonars, ultrasonic transducers, actuators, etc.

2.1.4. Pyroelectrics

The pyroelectricity is similar to the piezoelectricity, but electric field is induced by heat (temperature change) instead of strain (dimensional change).This phenomena was firstly observed in 1824 in quartz crystals. The pyroelectricity occurs in crystal (polar structure) materials without the centrum of symmetry (same as in the piezoelectrics), but with at least one axis of symmetry. This phenomena is temperature dependent, because dipole moments in the material are changing with dilatation of the crystal. The subordination of terms describing electrical behaviour of materials is shown in the Fig. 3. Pyroelectric thermometer can measure temperature change (sensitivity can be even 0.001 K), but not temperature itself [3]. Pyroelectric constant *p* can by defined by Eq. 11.

$$p = \frac{\delta E}{\delta T} \, [C \cdot m^{-2} \cdot K^{-1}]. \tag{11}$$

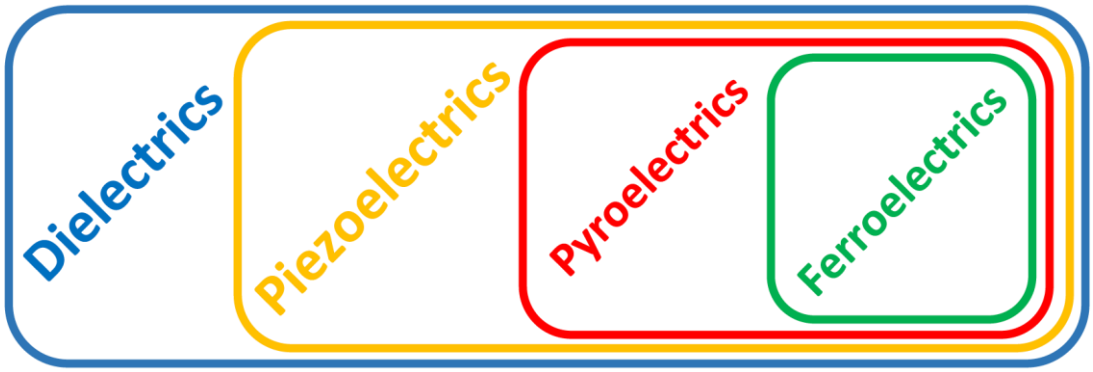

Fig. 3 Schematic diagram of electric terms subordination.

2.1.5. Ferroelectrics

The ferroelectrics are basically dielectric materials with spontaneous polarization. It means that they retain polarized even after removing of the external electric field. This behaviour can be observed after phase transition from high-temperature dielectric (paraelectric) phase to the low-temperature ferroelectric one at the Currie temperature T_C [K]. Onset of the spontaneous polarization is accompanied by sharp increase of relative permittivity, because at T_C an infinitely small electric field would cause large polarization [7].

Areas with the same (or similar) dipole orientation called "domains" are localized in their microstructure. Before a first contact with the external electric field, the domain structure is oriented randomly, so in macroscopic scale such a material can be still considered as an unpolarised one. Orientation of domains can be changed by applying an external electric field. The change of polarization direction corresponds to the direction and intensity of the field. Magnitude of (remanent) polarization is given by the of hysteresis loop, which shape depends on the material (see Fig. 4).

Ferroelectrics are widely used in data storage devices (FeRAM memories) and because of high relative permittivity close to the T_C for capacitors. They are also used in actuators and electromechanical transducers thanks to change of dimensions accompanying polarization process [8].

In ferroelectric materials with an ionic bond, short-range repulsion forces between neighboring electron clouds dominate at the temperatures higher than T_C, what results in the symmetric unpolarised state. With decreasing temperature (below T_C) the stabilizing forces associated with the polarization of the ions become stronger than the short-range repulsive ion-ion interactions. This results to the shifting of the stable ion positions from the symmetrical ones (creating distorted dipole structure). The polarized state becomes stable, even in the absence of an applied field [7].

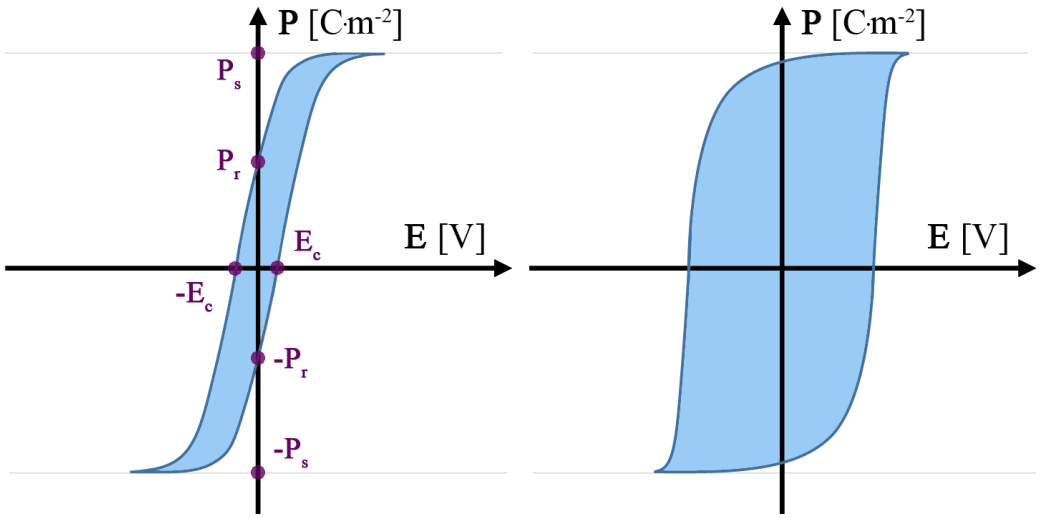

Fig. 4 Ferroelectric hysteresis loops of material with low (a) resp. high (b) remanent polarization (P_s – saturation polarization, P_r – remanent polarization, E_c – coercive field).

The ceramics with perovskite structure (stoichiometry ABO_3) are frequent subject of ferroelectricity studies because of their simple "cubic" lattice structure. There exist two complementary models of ferroelectric phase transitions. These materials usually allow the shift of the smaller cation (B) to one of ⟨111⟩ directions, but the strain in lattice can stabilize different displacement. The ferroelectricity is observed when local minimums of potential energy are situated in these directions (see Fig. 5).

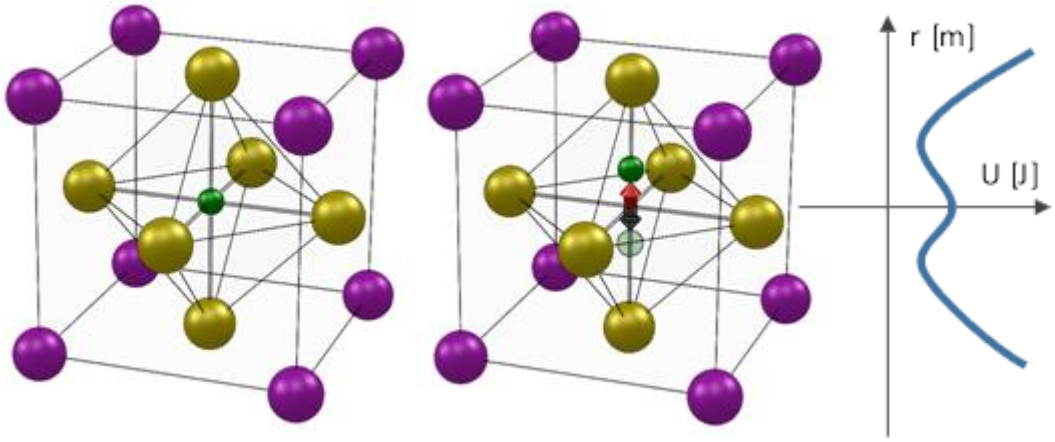

Fig. 5 "B" cation shift in the perovskite structure with double-well potential energy characteristic.

According to the "order-disorder" model there is always a shift in the positions of the "B" cations. Displacement in all of ⟨111⟩ directions is usually possible at the high temperatures, but with lowering temperature the number of these directions decreases giving orthorhombic (3 possible directions), tetragonal (2 possible directions) or rhombohedral symmetry (1 possible direction). This model predicts a large change of

entropy at the phase transition, which is not observed by experiments, but the model may be applicable in higher-temperatures, where any phase transformation does not occur [7].

On the other hand, "soft-mode" model predicts that the B cation displacement is stable only below the Curie temperature. At higher temperatures there is active the force which pushes the B cation back to the centre of symmetry. This force is caused by so-called "soft-mode" phonon. The influence of this phonon decreases with lowering temperature and expires at T_C, where its frequency is equal zero [7]. With absence of force which kept the B cation in the central position, the displacement occurs spontaneously (the ferroelectricity may be observed).

Although the function of B cations is essential for (spontaneous) polarization in perovskites, the identity of the A cations can have also crucial effect on the resulting ferroelectricity of the material. For example the strain caused by formation of new mixed orbitals from the original ones (hybridization of oxygen 2p orbitals) helps establishing long-range ordering, which is required for phase transition. Equally important for perovskite titanates (what is widely used type of perovskites - A$\mathbf{Ti^{+4}}O_3$) is fact that Ti^{4+} ion is formally in a d^0 state. It means that the lowest unoccupied energy levels are these "d" states which tend to hybridize with oxygen 2p orbitals. Most of the other ferroelectric perovskites like a zirconites (A$\mathbf{Zr^{+4}}O_3$) or niobates (A$\mathbf{Nb^{+5}}O_3$) contain also d^0 state [7].

Quantum paraelectrics

This not well understood phenomenon is considered as a kind of "incipient ferroelectricity", when the creation of domain structure is suppressed by quantum fluctuation. The "soft-mode" phonon frequency never become stable like in common ferroelectrics [9]. The dielectric permittivity increases with decreasing temperature, but it saturates below a temperature T_a [10] (see Fig. 6). It is believed that the zero point quantum fluctuations prevent freezing of a ferroelectric soft mode and stabilize the paraelectric phase below T_a [10].

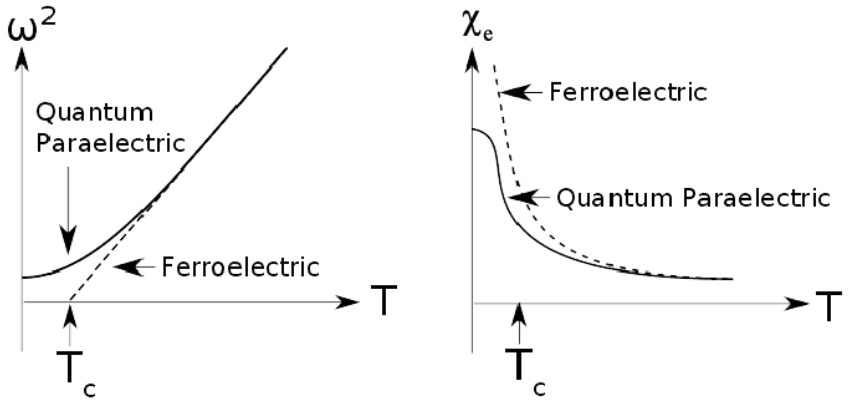

Fig. 6 Ferroelectric "soft-mode" frequency ω [s^{-1}] and dielectric susceptibility χ_e [-] as a function of temperature T [K] in case of ferroelectric and quantum paraelectric material.

2.2. Magnetic properties

Many magnetic properties and characteristics are analogous to those electric ones. For example magnetic polarization J [T = Wb·m^{-2}] corresponds to the electric polarization density P [C·m^{-2}], the intensity of magnetic field H [A·m^{-1}] corresponds to the intensity of electric field E [V·m^{-1}], the magnetic induction (magnetic flux density) B [T = Wb·m^{-2}] corresponds to the electric induction (electric displacement) D [C·m^{-2}], permeability μ [H·m^{-1}] corresponds to permittivity ε [F·m^{-1}] and magnetic susceptibility χ_m [-] corresponds to electric susceptibility χ_e [-]. New unit is magnetization M [A·m^{-1}]. The relationships between magnetic variables are given by Eq. 12 – 15

$$\mu_r = \frac{\mu}{\mu_o} \; [-], \tag{12}$$

$$\chi_m = \mu_r - 1 \; [-], \tag{13}$$

$$J = \mu_o \cdot H \cdot \chi_m = \mu_o \cdot M \; [T], \tag{14}$$

$$B = \mu_o \cdot H + J = \mu_o \cdot H \cdot (1 + \chi_m) = \mu \cdot H \; [T]. \tag{15}$$

Every electron in an atom has its orbital and spin dipole moment. Magnetic moment is the vector characteristic. If the summary of all these vectors for every electron in every atom of the sample (the vector resultant) gives a macroscopic magnetic field, the material can be considered as a magnetic one. There are three basic types of magnetic materials (diamagnetics, paramagnetics and ferromagnetics) [1].

2.2.1. Diamagnetics

These materials are kind of magnetic analogy of electric insulators (insulators can be weakly polarized, but they are not usually called "dielectrics"). Diamagnetic behaviour occurs in every material, but it is so weak, that it can be covered up by any other type of magnetism. After placing any material into the external magnetic field, there are induced weak magnetic dipole moments (oriented in the opposite direction than the external field) in its atoms. The resultant (macroscopic) magnetic field is also very weak and it disappears when the material is removed from the external magnetic field [1].

Most of the ceramic materials don't have any other magnetic behaviour so they can be considered as diamagnetics. Diamagnetic ceramics do not have any commercial applications (from the magnetic behaviour point of view) with exception of superconductive ceramic materials [3].

2.2.2. Paramagnetics

Paramagnetism can be observed in the materials, which are consisted from atoms with natural magnetic dipole moments (e.g. atoms with unpaired electrons), which are randomly oriented so the material doesn't exhibit any macroscopic (resulted) magnetic moment. These are especially materials which contain actinides, transition and rare earth elements. After placing a paramagnetic sample into an external magnetic field, existing dipole moments in the sample try to be oriented in the same direction as the external field. The orientation of such a macroscopic magnetic moment is in opposite direction than in case of diamagnetics. If the external magnetic field is not homogenous, paramagnetics are attracted from the area with lower magnetic induction into the area with higher one.

Random atom collisions (result of disordered thermal motion) disrupt the alignment with the external field and reduce the magnitude of the resulting magnetic dipole moment of the sample. It means that with increasing temperature the macroscopic dipole moment is decreasing. In the 1895 Pierre Curie discovered by his experiments the equation expressing the dependence of magnetization M of sample on the temperature T and induction of the external magnetic field B_{ext} (see Eq. 16; where C is the Curie material constant, N_A is Avogadro constant, R is the gas constant, μ_B is Bohr magneton = 9.27400915e-24 $J \cdot T^{-1}$, N is the number of magnetic entities, g is the Landé g-factor, J is the angular momentum quantum number) [1, 3]

$$\mathrm{M} = \mathrm{C} \cdot \frac{\mathrm{B_{ext}}}{\mathrm{T}} = \frac{\mathrm{N_A} \cdot {\mu_\mathrm{B}}^2 \cdot \mathrm{N} \cdot \mathrm{g}^2}{\mathrm{R}} \cdot \mathrm{J} \cdot (\mathrm{J} - 1) \cdot \frac{\mathrm{B_{ext}}}{\mathrm{T}} [\mathrm{A} \cdot \mathrm{m}^{-1}]. \quad (16)$$

2.2.3. Ferromagnetics

The ferromagnetic materials undergo at the Curie temperature (θ_C in case of magnetic properties) phase transition from low-temperature ferromagnetic to the high-temperature paramagnetic one. As well as in the case of paramagnetics the origin of ferromagnetic behaviour comes from unpaired electron spins, but there is also an interaction between adjacent dipoles because of quantum phenomena [3].

For example iron (Fe), cobalt (Co), nickel (Ni), gadolinium (Gd), dysprosium (Dy) and alloys of these (or some others even non-ferromagnetic) elements are ferromagnetic. The reason is quantum mechanical exchange interaction between the 3d orbitals of adjacent atoms. It means that electron spins of an atom are influenced by the neighbouring atoms resulting in identical electron spins (dipole orientation). Such a material induces macroscopic magnetic moment even without applying external magnetic field. This phenomena is called spontaneous magnetization [1].

The first theory which tried to explain ferromagnetic behaviour was Curie-Weiss theory [11]. Weiss predicted internal "molecular field" which can be considered as predecessor of present understanding of ferromagnetism. His explanation of experimentally obtained data of susceptibility by Curie-Weiss law is still valid for many magnetic material (see Fig. 7). On the other hand his theory says that magnetic

moment of every atom or molecule should be in paramagnetic phase same like in the ferromagnetic one, what is not observed in the experiments. Also according the localized-moment theory the magnetic dipole moment of atoms should correspond to integer number of its electrons and this is again in a conflict with measured data.

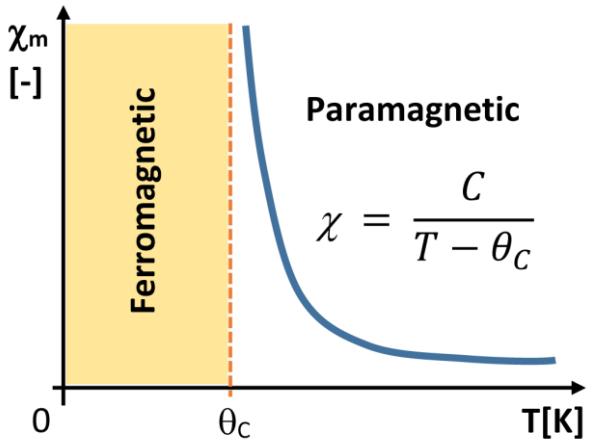

Fig. 7 Dependence of temperature *T* on the magnetic susceptibility (Curie-Weiss law is applicable for high-temperature paramagnetic phase).

Next theory is the Stoner one [12], which again describes the exchange energy as a driving force of ferromagnetism. Exchange energy exhibits a minimum when unpaired electrons of neighboring atoms have the same spin. On the other hand this phenomena causes the increase of band energy needed for movement of electrons from the fully occupied lower-energy band to higher-energy band. This is the reason why not every metallic element is ferromagnetic. In ferromagnetic transition metals (Fe, Ni, Co) the Fermi energy goes through 3d and 4s bands. This energy arrangement causes that valence electrons occupy both of them. Electrons, which move to the higher empty state and invert their spin, need to increase their own kinetic energy. Whereas 4s band is very broad and has low density of energy states at Fermi level; the 3d band is narrow with high density of the states. It means that the energy needed for skipping to empty state is much lower in 3d band than in 4s band. The exchange energy mechanism dominates when the increase of kinetic energy is lower than the decrease caused by adjustment of electron spins. Higher amount of electrons near the Fermi level decreases the energy needed for the spin reversing. For example in nickel the exchange energy decrease is so strong, that 5 electrons are located in one 3d band and the other contains 0.54 holes. Thanks to that, the saturation magnetization of Ni is 0.54 μ_B per one atom in the sample [7].

Magnetic dipoles with the identical orientation are localized in the small areas called “domains”. Before applying external magnetic field, this domain structure is oriented randomly. During magnetization two concurrent processes are running. With increasing intensity of external magnetic field, domains with the similar magnetic dipole orientation are enlarging (1st process). The others are gradually reoriented to direction parallel with the external field (their orientation is than the same or more

similar to the orientation of the field – 2nd process). These processes together influence the shape of the magnetization (hysteresis) curves (Fig. 8) [1, 3].

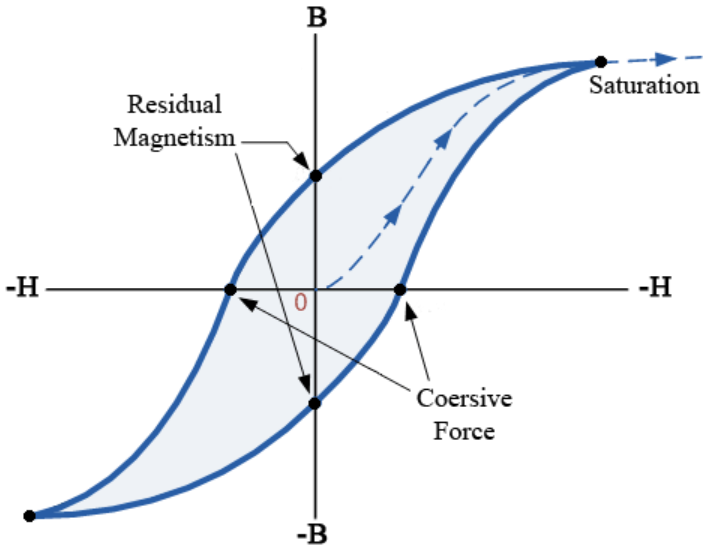

Fig. 8 Ferromagnetic hysteresis loop.

Anti-ferromagnetics

It was already stated that ferromagnetic behaviour is caused by quantum mechanical exchange interaction between the 3d orbitals of adjacent atoms. This phenomena is mathematically represented by so-called "exchange integral" *J*. For values higher than zero ($J > 0$) magnetic dipoles are spontaneously line up (because of above mentioned interactions) and material is ferroelectric below θ_C. But for values of exchange integral lower than zero ($J < 0$) adjacent dipoles line up anti-parallel causing anti-ferroelectricity below Néel temperature T_N. Macroscopic magnetic moment is equal zero in this case [3, 7] (see Fig. 9).

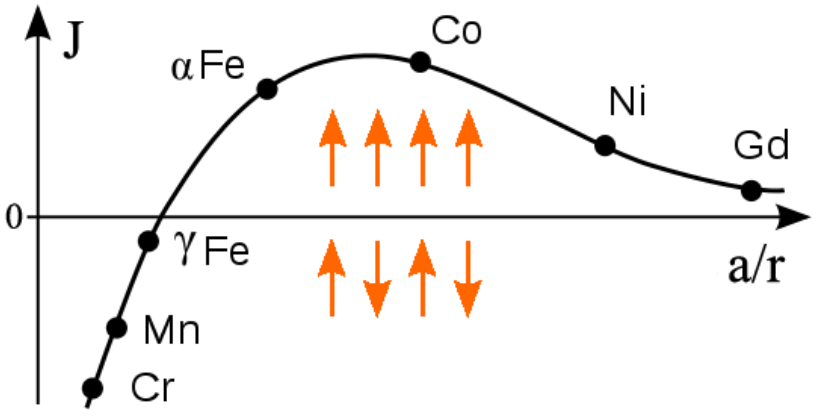

Fig. 9 Bethe-Slater curve represents the exchange energy (exchange integral J) for transition metals as a function of the ratio of the interatomic distance *a* to the radius of the 3d electron shell *r*.

Ferrimagnetics

In this special type of magnetic setup one type of magnetic moment (one type of ions) is aligned in the lattice structure, whereas the second weaker one is aligned in the opposite direction (see Fig. 10). Ferrimagnetism is as well as ferromagnetism lost above the θ_C. These two phenomena are similar also in the cooperative alignment between magnetic dipoles, what leads to the existence of macroscopic magnetic moment even without applying the external magnetic field. Most of the ferrimagnetic ceramics have the (inverse) spinel, garnet or magnetoplumbite structure.

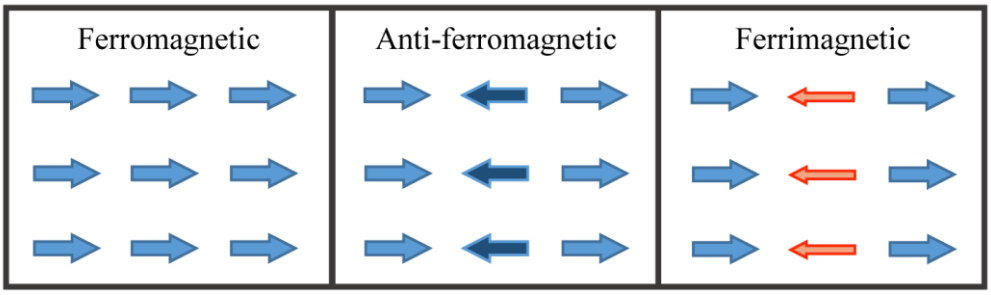

Fig. 10 Schema of ferromagnetic, anti-ferromagnetic and ferrimagnetic magnetic moment setup.

2.3. Multiferroics

In the above text, some types of ferroic behaviour were described. Generally it can be stated that ferroics are materials with spontaneous ordering even in absence of external field. In ferroelectrics it is spontaneous polarization, in ferromagnetics spontaneous magnetization and in ferroelastics spontaneous deformation (deformation occurs spontaneously and can be switched by stress field).

The first definition of "multiferroics" was published by H. Schmid in 1994 [13], where the multiferroics are described as materials in which two or all three of the properties "ferroelectricity", "ferromagnetism" and "ferroelasticity" occur simultaneously in the same phase. The most common use of this term is for the materials which are ferroelectric and ferromagnetic (see Fig. 11). Broader explanation of multiferroics takes into account also other types of magnetic ordering, such a ferrimagnetism and anti-ferromagnetism [14].

Most of the published multiferroic materials belong to class of "complex oxides". These compounds contain usually two or more transition metal cations and oxygen. The intermediate ionic-covalent nature of transitionmetal-oxygen bonds leads to strong polarizability and the highly localized transition-metals with 3d electrons usually lead to some kind of magnetic order. Also other materials such fluorides or selenides could be equally interesting [14, 15].

Magnetoelectrics

The term "magnetoelectric" was firstly used by Debye in 1926 [16]. Magnetoelectrics are defined as the materials which electrical polarization can be tuned by external magnetic field and/or magnetization can be tuned by external electric field (see Fig. 11).

Magnetoelectric behaviour in the multiferroics is highly attractive from the point of view of memory device applications. For example present magnetic random access memories (RAM) need for "writing" (magnetization) high current densities, which causes heating of such devices and makes further miniaturization impossible. In the case of magnetoelectric multiferroics it would be possible to change the orientation of magnetic domains by external electric field. However, currently these phenomena are primarily interesting from the point of view of basic research rather than of applications [17].

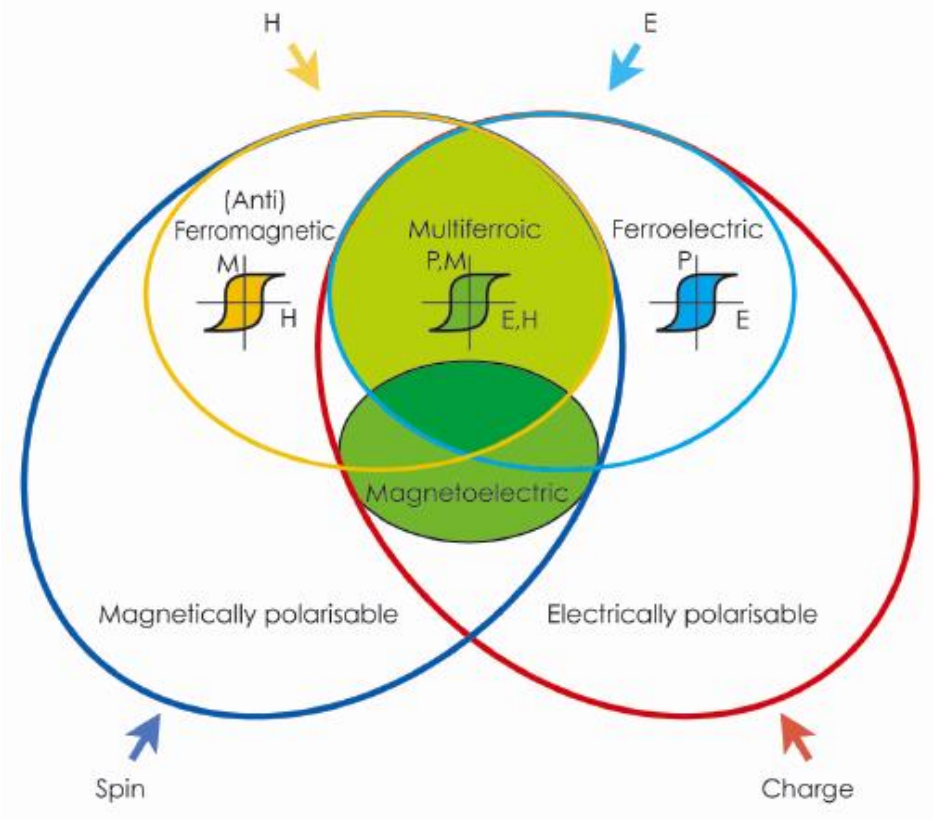

Fig. 11 Multiferroics combining ferroelectric and ferromagnetic behaviour.

The linear magnetoelectric binding is mostly very weak. It was published that the magnitude of linear magnetoelectric effect is dependent on the magnitude of the magnetic permeability and the dielectric permittivity [18]. Both of these quantities exhibits their own maximum at the Curie temperatures (T_C in case of permittivity and θ_C for permeability) and therefore material engineers try to tailor the materials so, that these transition temperatures are very similar and also close to room temperature (RT).

Although the research of multiferroics run since sixties of last century, the steep development of these materials began with 21st century (Fig. 12).

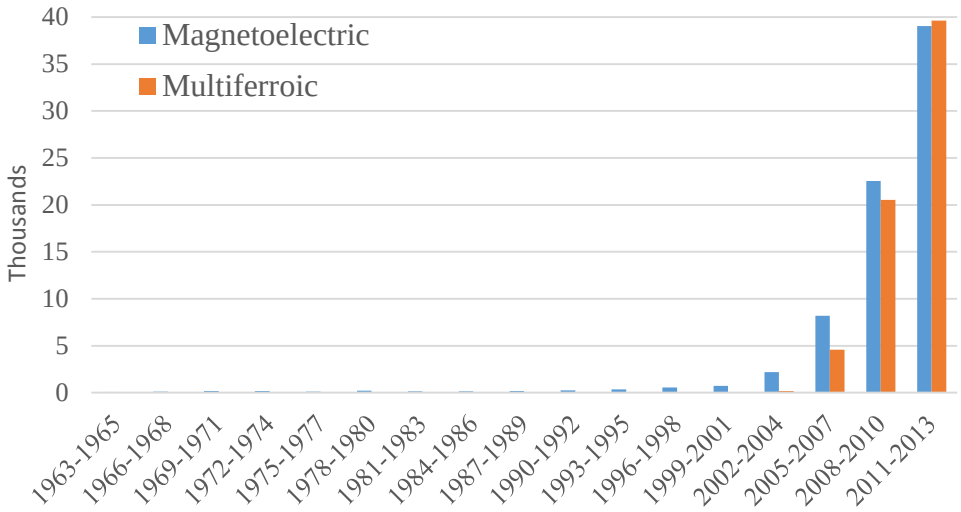

Fig. 12 Number of publication with the key-word "Magnetoelectric" or "Multiferroic" in the Web of knowledge database since 1990.

There are known only several multiferroic materials and according to author's best knowledge, it was found only one material which exhibits multiferroic behaviour up to room temperature (T_R) up to now - $BiFeO_3$ [19]. Unfortunately this ceramic material belongs to multiferroics with weak magnetoelectric (ME) effect as the major part of multiferroics. In the recent time material $Sr_3Co_2Fe_{24}O_{41}$ was studied, because it exhibits strong ME effect at T_R, but its ferroelectricity is conditioned by presence of external magnetic field [20]. The condition of single phase material is also sometimes "broken" in case of composites.

How it was already mentioned above, these materials have very appealing applications in future (the multi-state memory devices) [21], but in present time they serve more as a subject of basic research.

2.3.1. Requirements for magnetoelectric multiferroics

The symmetrical, structural, chemical and other conditions needed for establishing ferromagnetic and ferroelectric order with ME effect in one phase was summarized by N. A. Hill et al. [7]:

Symmetry

The symmetry requirements are important, but they are not probably the reason why only a little number of multiferroic materials is known. There are 31 point groups, which allow ferroelectric order and the same number of them, which allow ferromagnetic ordering. These two sets have common 13 point groups, where both of spontaneous ordering is possible (1, 2, 2′, *m*, *m*′, 3, 3*m*′, 4, 4*m*′*m*′, *m*′*m*2′, *m*′*m*′2′, 6 and 6*m*′*m*′).

Conductivity

As it was mentioned in the chapter 2.1. "Electric properties", dielectrics and ferroelectrics are kind of sub-brand of electric insulators, otherwise the external electrical field would induce electrical current instead of polarization in the material. Strong magnetic behaviour is observed mostly in the metals and their alloys (Fe, Ni, Co, etc.). The reason is not their metallicity but high density of states at the Fermi level. Unfortunately this characteristic usually also results in good conductivity.

It could be a problem if only strong ferromagnetic ordering is the field of our interest, but extended definition of multiferroics considers also presence of other magnetic ordering as ferrimagnetic and anti-ferromagnetic. Most of the known materials with these types of magnetic ordering are electric insulators. Despite of this extended definition only small number of such a materials are known.

Occupancy of the "d" orbital

Because of simple (high symmetrical) structure of perovskites, these materials are often used for ME effect study. Presence of the "*d* electrons" is usually required for any magnetic ordering in these materials (because they create localized magnetic moments). On the other hand common ferroelectric perovskite oxide (ABO_3) has usually B cation with "d^0" electron orbital occupancy. It seems that partial occupancy of *d* orbital in the B cation mostly suppress its tendency to move from the central position and create an electric dipole moment (ferroelectric phase).

After simple comparison of the Shannon ionic radii [22] of some common "d^0 cations" (Ti^{+4}, Nb^{+5}, Zr^{+4}) with "d^n cations" (Ti^{+3}, Mn^{+3}, V^{+4}) it can be considered that this phenomenon is not a function of B cation size.

Another possible reason for such a behaviour is that material undergoes different type of distortion than the ferroelectric one (dislocation of B cation from central symmetry). The example can be shown in $LaMnO_3$, where the Mn^{+3} ion is in d^4 configuration. This material exhibits Jahn-Teller distortion, in which the elongated axes of the oxygen octahedra are oriented parallel to each other along the crystallographic *c* axis (orbital ordering occurs simultaneously with it). Same situation is observed also in $YTiO_3$ and YVO_3 when neither of them is ferroelectric [23].

3. Processing of advanced ceramics

3.1. Powder processing

There are three basic approaches of ceramic powder processing. They are mechanical, chemical, vapour phase processes and of course their combinations.

Mechanical methods usually work with roughly grinded derivatives of naturally occurring minerals. By alternation of milling and sieving steps it is possible to obtain ceramic powder with desired distribution of particle size. Mainly due to low cost, these processes are commonly used for manufacturing of traditional ceramics where the mass production is needed.

Chemical processes provide some advantages in comparison with mechanical methods. For example in the case of sol-gel methods, the morphology and purity of resulted powder can be precisely controlled. These processes are widely used for producing of advanced ceramic powders and nanopowders [3].

Vapour phase methods are also used for ceramic powder production, but these techniques are very expensive and their ability to prepare bigger amount of powder is limited. On the other hand, they are able to produce ceramic nanopowders with particle sizes in range of few nanometers.

Solid State Synthesis

This combination of mechanical and chemical methods is quite simple, cheap and fast. It is based on proper mixing of ceramic powder precursor (usually oxides, carbonites or hydroxides) and heating such a mixture at elevated temperature allowing diffusion of ions. The success of this technique depends on thermodynamic (temperature, pressure, atmosphere, etc.), kinetics (dwell time) and chemical condition of the system. The biggest disadvantage is particle growth (surface energy minimization).

Precipitation Synthesis

This technique belongs to chemical methods and it is the most often used "wet method" for synthetizing perovskite materials (ABO_3). The basic principle is creating of solution *A* and *B* salts, which is precipitated by strong basis (usually NaOH or KOH solution). The sources of A and B ions are mostly chlorides, hydroxides and nitrides. Creation of unagglomerated particles can be supported by addition of surfactant.

Hydrothermal Synthesis

The hydrothermal synthesis (HTS) allows to control the thermodynamic stability of the system due to low reaction temperatures, longer dwell times and increased pressure. That is also why this method is often used for syntheses with particle size controlling. The pressure chemical reactors with chemically resistant insert (e.g. Teflon) are used to content reactions in the highly alkaline environments.

3.2. Powder modification

In the case of advanced ceramic powder, it is sometimes necessary to change its characteristic. Whereas chemical and phase purity is result of powder synthesis (mostly unchangeable), the morphology can be partly modified (e.g. particle size, particle size distribution, particle shape, particle structure and homogeneity in case of multiphase powder mixtures).

3.2.1. Milling and mixing

The most common technique for particle size reduction is milling. The milling (or mixing) effect is realized by intensive movement and impacts of milling media. There are many types of this process, but the most commonly used are (planetary) ball milling, attrition milling, vibratory milling and fluid-energy milling [3].

Manual mixing

This is the oldest, cheapest and simplest method how to homogenize powder materials and break their agglomerates. The process mostly goes in the mortar, which is usually made from traditional ceramic with glaze, brass, steel etc. In the case of advanced ceramic materials the agate mortars are used. The efficiency of manual mixing strongly depends on the human factor, so the repeatability is ordinary "imperfect".

Planetary ball milling

This technique is one of the most effective method, when the planetary movement energy of the milling bowls is converted to the high kinetic energy of milling balls inside. In case of high-energy ball milling the energy is high enough to establish appropriate thermodynamic condition for precursors' reaction, which would not normally react at the room temperature [24, 25]. The process can run in dry or wet conditions; also different atmospheres are sometimes used. Milling bowls and elements are made from many types of material and volumes (e.g. steel, agate, alumina, zirconia, tungsten carbide, etc.) see Fig. 13. Anyway in this work mostly the zirconia and polyamide milling bowls were used with combination of zirconia milling balls.

Fig. 13 Milling bowls and elements with different volumes and materials.

Attrition mill

In the attrition mill the powder particles (together with milling elements) are drifted by stirring arms mounted on an axial shaft. So in comparison with ball milling the milling vessel is static.

Vibratory milling

This method is a progressive technique where the powder and milling media are placed in the drum (bowl) which is continuously vigorously shaken.

Fluid energy milling

This technique also called "jet milling" uses for particle size reduction the collisions of particles in the high-velocity fluid (usually compressed air or super-heated steam). The powder is added to this fluid and injected into the grinding chamber at sonic (or almost sonic) speed. The chamber is designed to minimalize the impact of particle to its walls [3].

3.2.2. Sieving

Sieving is a method for narrowing (sharping) the particle size distribution by sorting out the powder particles according the sieve size. In the case of advanced ceramic powders, sieving is mostly used for separation of the fine powder from extremely big particles and agglomerates, which would lead to the defects formation in the bulk ceramics. The reason is simple - sieving is normally not applicable to particles smaller than 5μm. The term "mesh size" is used for designation of the sieves – it is actually the number of holes per linear inch. The sieving time can be shortened by using the specialized vibration devices, where the setup of sieves is placed [3].

3.2.3. Granulation

This processing step is used for easier dry shaping of the ceramic green body (pressing). Because of friction and inconvenient shape of the particles, it is very difficult to compact homogenous bulk ceramic precursor. Fine powders are therefore granulated (the most commonly by spray-drying) into to spherical powder granules of 20-250 μm in the size. The organic additives are usually used to ensure the plasticity and sufficient handling strength of the precursor after compaction [26].

3.3. Green body shaping

All shaping methods of advanced ceramic powders have the same aim - a fabrication of green body with required shape, relative density and as homogenous microstructure as possible.

3.3.1. Dry-shaping methods

Uniaxial pressing

This simple type of pressing is the most common method of advanced ceramic powder compacting. Uniaxial pressing can be done with one or two moving piston in one axis. Two piston layout (see Fig. 14 left) provides more homogenous stress field resulting in more homogenous green body. Anyway this technique is usually used for mass production of simple shaped precursors of low height. With increasing high of bodies the rate of inhomogeneity rises too (particle friction problem). The pressed ceramic green body is consistent more or less because of Van der Waals forces which are not strong enough to keep the ceramic precursor in one piece due to inhomogeneous (relief) stress field. To prevent such a scenario, polymer binder additives are used as well as lower compression stresses (in comparison with isostatic pressing).

Isostatic pressing

Cold isostatic press (see Fig. 14 right) means that the pressing forces are compacting the ceramic powder at room temperature from all directions resulting in more homogenous structure than the previous method. Isostatic pressure is achieved through hydrostatic pressure of liquid media (usually distilled water with lubricant). The powder is placed in a flexible (rubber or other polymer) mold. The flexibility of the mold is also the reason of irregularity of the final shape, so usually the dimension and shape correction (e.g. grinding) are necessary. Besides the higher homogeneity, very high pressures (up to 1000 GPa, but more common are values around 300 MPa) are also important advantage of isostatic pressing. As an indirect influence of homogenous stress field the binder additives are usually not necessary [26].

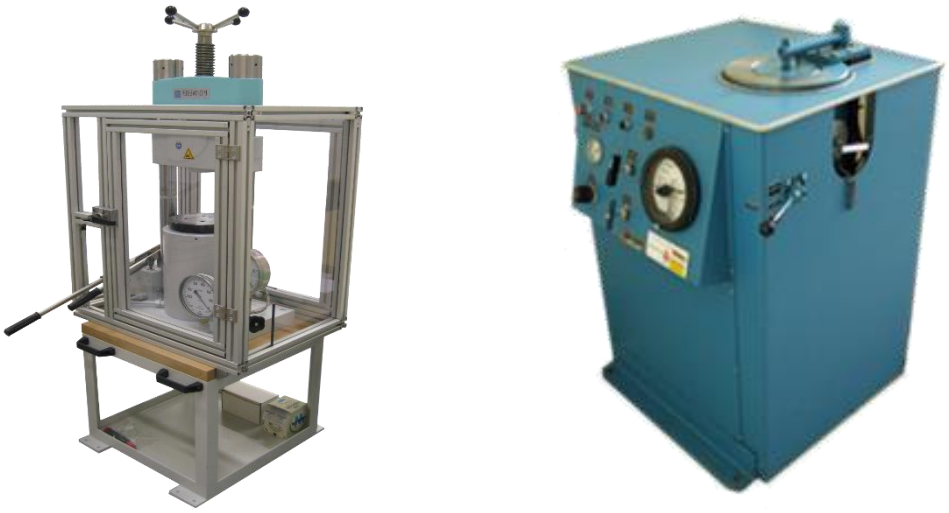

Fig. 14 Manual uniaxial press – PO Weber (left) and cold isostatic press - Autoclave Engineers (right) which were used for part of presented experiments.

3.3.2. Wet shaping methods

These techniques use colloidal suspensions of ceramic powders. Well dispersed and stable suspension is probably the most important condition for regular particle packing in the consolidated green bodies.

Slip casting

Particle deposition is caused by flow of liquid from suspension through the porous mould (usually made of gypsum). The pores are big enough to ensure the sufficient liquid flow but smaller than ceramic particles. The capillary forces create suction pressure up to 0.1 MPa [26], which can be even increased by external pressure on the suspension (pressure filtration) or by centrifugal forces (centrifugal casting).

Direct casting

In contrast to slip casting, the moulds are not porous so the most important feature of these methods is the capability to change uniform dispersion of particles in the colloidal suspensions directly to compact green body without removing of solvent. The key step in reaching such a phenomena is gelation process (physical or chemical) [26].

3.3.3. Plastic shaping methods

These techniques are specific because the green bodies are formed by ceramic-additive mixture deformation. Under certain stress and temperature this mixture plastically flow into the die. The shape of the die has to be precisely designed, because after drying and firing significant dimensions changes occurs. Even through difficult designing of the die, green bodies with a complicated shape can be manufactured. The most important methods in this brand are "injection moulding" and "extrusion" [26].

3.4. Sintering

Simple definition of this important processing step says that sintering is high-temperature process of transforming a compacted powder into the solid (bulk) body. Driving force of this diffusion process is a decrease of the Gibbs free energy (Eq. 17; where G [J] is Gibbs free energy, V [m^3] is volume of the system, p [Pa] is pressure, S_{ent} [$J \cdot K^{-1}$] is entropy, T [K] is temperature, γ [$J \cdot m^{-2}$] is the specific surface energy – either solid-gas or solid-solid, and S [m^2] is the interface surface)

$$dG = V \cdot dp - S_{ent} \cdot dT + \gamma \cdot dS \text{ [J]}. \quad (17)$$

The decrease of Gibbs free energy is caused by need of the system to reduce its surface energy in response to external temperature, pressure or chemical reaction (or their combinations). Last two of them do not lead to consolidation, but help to decrease the sintering time or the temperature needed for the sintering process.

There are two mechanisms of lowering the free surface energy. The first one is the reduction of the particles' surface (grain growth) and the second one is the change of (energy consuming) interphase "solid-gas" to (less energetically demanding) interphase "solid-solid" (consolidation). These phenomena are described by Eq. 18

$$\Delta(\gamma \cdot S) = \gamma^{sg} \cdot \Delta S + \Delta\gamma^{sg \rightarrow ss} \cdot S \text{ [J]}. \quad (18)$$

The grain growth would lead to the decrease of the system free energy but not to material consolidation. From the point of view of dense bulk ceramics processing, the key process is the second one (consolidation). These two processes are running (more or less) continuously. So it could be stated, that during sintering it is generally impossible to separate them and densify sample without any grain growth (see Fig. 15) [26].

Unfortunately, the grain growth is in most of applications of advanced ceramics undesirable, due to degradation of important mechanical properties (hardness [27], flexural strength [28, 29], mechanical and biological wear resistance [30, 31]).

Consolidation driving force was already described in the text above, but equally important is the way of mass transport during the sintering. In the case of advanced ceramics, the main transport mechanism is the diffusion. Diffusion is temperature activated process (that is why the high temperature is needed for ceramics consolidation), which can be according its path divided into surface diffusion, volume diffusion and grain boundary diffusion. The last two of them are the most important for densification of ceramic precursor, because only they are able to deliver the mass from the grain boundaries to empty space between particles and cause shrinkage. The sintering process can be divided into three basic stages such as necks formation, open porosity and closed porosity (Fig. 16).

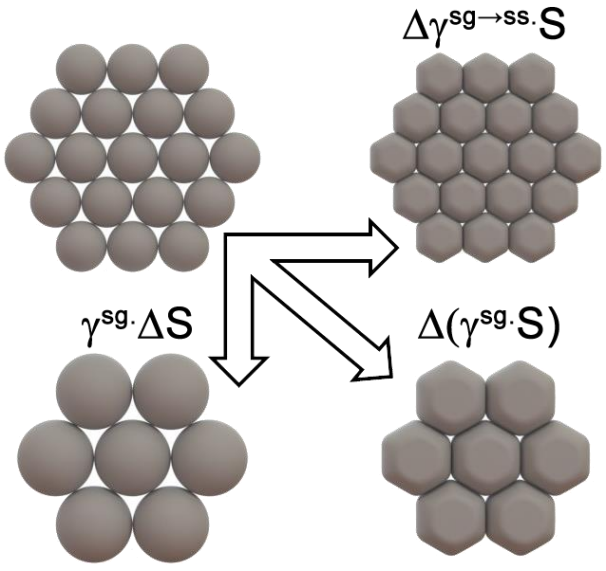

Fig. 15 Schema of surface energy decrease by grain growth and/or consolidation during sintering [26].

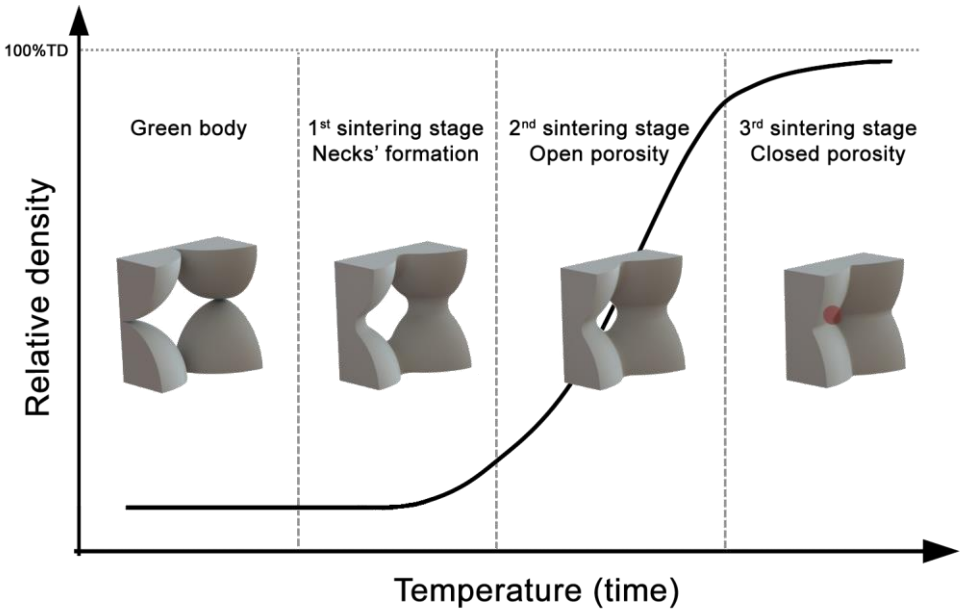

Fig. 16 The typically shaped sintering (densification) curve divided into three main phases of the sintering process.

The first stage is defined by formation of necks between the ceramic particles in contact. There are many theoretical models trying to describe this process [3, 32, 33] and most of them are dealing with ideal spherical particles. This stage is characteristic by a very small shrinkage, but thanks to necks formation the strength is increasing (in comparison with green body). In the second phase the porosity can be described as a network of tubular pores reminding kind of sponge. After the relative density of ceramics reaches approximately 92 % of the theoretical density (%TD), the pores get closed so they are no longer connected to each other or with the outer body surface (closed porosity is established) [26].

Most of the advanced ceramic applications require a minimum amount of defects (cracks or pores), but especially in the case of functional ceramics (e.g. electroceramics) also chemical and phase purity are needed. From the point of view of these challenging requirements many unique sintering techniques were developed. These methods can be divided into two basic groups, "pressure-less" and "pressure-assisted" sintering.

3.4.1. Pressure-less sintering

This is the oldest and simultaneously the most widely used sintering technique, because it is cheap and undemanding (only conventional high-temperature furnace is needed). In this method the heating rates (usually 1-25°C·min^{-1}), sintering temperature, dwell time and in case of specialized device also a pressure and composition of the furnace atmosphere can be controlled.

The influence of heating regime on the final relative density and grain size of ceramic sample is still discussed in the literature. According to conventional sintering models, the sinterability of ceramics is defined by the starting microstructure (green body density and particle size). It would mean that sintered ceramic samples (made from the same green-body precursor) with the same final densities will also have the same microstructure (grain size), no matter which heating regime was used [34-36]. Another theories say that grain size in the sample with required relative density can be influenced by proper choice of heating regime. The most reported theory in this field is Two-Step Sintering (TSS) [37]. In the first step the green body is sintered till the point, when supercritical pores disappear from the microstructure (usually between 75-95 % of theoretical density). The second step begins with steep cooling to lower temperature, where the ceramic sample stays until the required relative density is reached (typically 10 – 20 hours). This method is used for sintering many ceramic materials [38, 39], but the biggest decrease of grain growth in comparison with conventional heating regimes were published in case of materials with cubic structure (e.g. $BaTiO_3$ [40], $SrTiO_3$ [41, 42] and c-ZrO_2 [20, 39]).

Also other types of sintering methods with unconventional type of heating belong to the group of pressure-less sintering. For example microwave sintering enables very high heating rates (up to 1000°C·min^{-1}) because the heating is not realized by heat transfer (convection of radiation), but by energy conversion. The biggest disadvantage of this method is a huge material dependence, because every material absorbs the energy from microwaves differently [43].

Below you can find the description of furnaces which were used for experiments described in this thesis.

Conventional furnace

The Nabertherm furnace (see Fig. 17 – left) can be used for the annealing or sintering in air atmosphere. The maximum temperature is 1700 – 1750 °C thanks to super-kanthal heating elements. The temperature in the furnace chamber is measured by thermocouple PtRh6 – PtRh30 (type B).

Vacuum furnace

For part of the experiments the vacuum furnace Degussa (see Fig. 17 - middle) with kanthal heating elements was used. The furnace can operate in high vacuum (up to 10 Pa) as well as in inert or slightly reducing stationary atmospheres (10 – 10^5 Pa). The temperature in the furnace chamber is measured by thermocouple of type PtRh6 – PtRh30. Maximum operating temperature is 1500 – 1550 °C.

Hydrogen furnace

The Novex furnace (see Fig. 17 - right) was used for all experiments with hydrogen atmosphere in this work. The furnace has tungsten heating elements and can reach sintering temperature up to 1900 °C (in the hydrogen atmosphere). The temperature is measured by thermocouple WRe3 – WRe25.

Fig. 17 Conventional furnace Nabertherm (left), Vacuum furnace Degussa (middle) and hydrogen furnace Novex (right).

3.4.2. Pressure-assisted sintering

These methods are often very effective, but they are mostly also very expensive (especially the devices themselves). That is why these techniques are used mostly only in cases, where conventional pressure-less sintering does not provide satisfying results. Applied pressure increases the driving force of sintering, therefore shorter dwell times or lower sintering temperatures can be used in the process. A few examples of such methods are described below.

Hot Isostatic Pressing (HIP)

Absence of sample shape limitation is the most important advantage of this method. It means that the parallel bottom and top plains or any other symmetry requirements are not needed. This sintering method is usually used for ceramic samples with closed porosity (pre-sintered samples). The necessity of closed porosity can be bypassed by the hermetic metal or glass case around a sample with open porosity. Mostly, the case is casted around the ceramic precursor, because it has to copy the sample surface precisely.

Operation of HIP as well as the machine cost is very expensive, therefore it is usually used only for samples which cannot reach full density by conventional sintering methods or higher sintering temperature would lead to uncontrolled grain growth. Whole process runs usually in the inert argon atmosphere.

Hot pressing

In this method any pre-sintering step is not necessary (powder materials are usually used), but sintering of porous ceramics is also possible. Conventional heating

is used as well as in the case of HIP, but the pressure is not applied on the sample by atmosphere but by pistons. The most common material of dies is graphite, because of its high creep resistance at high temperatures. That is also one of the reasons why the process need to run in non-oxidizing atmosphere. This device is cheaper than HIP, but the disadvantages are the carbon pollution and inhomogeneous microstructure of the sample.

Spark Plasma Sintering (SPS)

This advanced technique is similar to "Hot pressing", but the most important difference is the type of heating. SPS uses for heating the pulse direct current which goes through the carbon die and sample (in the case of conductive sample). This allows very high heating rates (up to 500°C·min^{-1}). There were reported fully dense ceramic samples with very small grain size (below 100 nm) in case of nano-powder ceramic precursors. This is possible because of high heating rates and short dwell times at sintering temperature (only a few minutes). The effect of electro-magnetic field (coming from the pulse direct current) is still a subject of discussion. Because of graphite dies, the high vacuums is usually used in this method [44-47].

The furnace FCT Systeme GmbH (available in the University of Duisburg-Essen; see Fig. 18) was used for all experiments using Spark-Plasma Sintering technique. The graphite die with two piston layout and inner diameter 18 mm was used as a heating element (also as a die for forming the green bodies). This setup allows to use a powder as a starting material.

Fig. 18 FCT Spark-Plasma Sintering furnace and schema of the principle [26].

The whole procedure of die preparation is shown in Fig. 19 by step 1-10 (1 - spraying one side of graphite foil by Boron nitride; 2 – rolling up of the graphite foil; 3 – putting of the rolled foil into the die and gently polishing of its inner surface

by one of the graphite pistons; 4 – inserting of two graphite foils to cover the downer piston; 5 – adding the powder material; 6 – gentle levelling of the powder; 7 – pulling out the piston; 8 – inserting of two graphite foils and then the upper piston; 9 – pressing of the graphite die by uniaxial press; 10 – inserting of the die into the SPS device and completing of the setup).

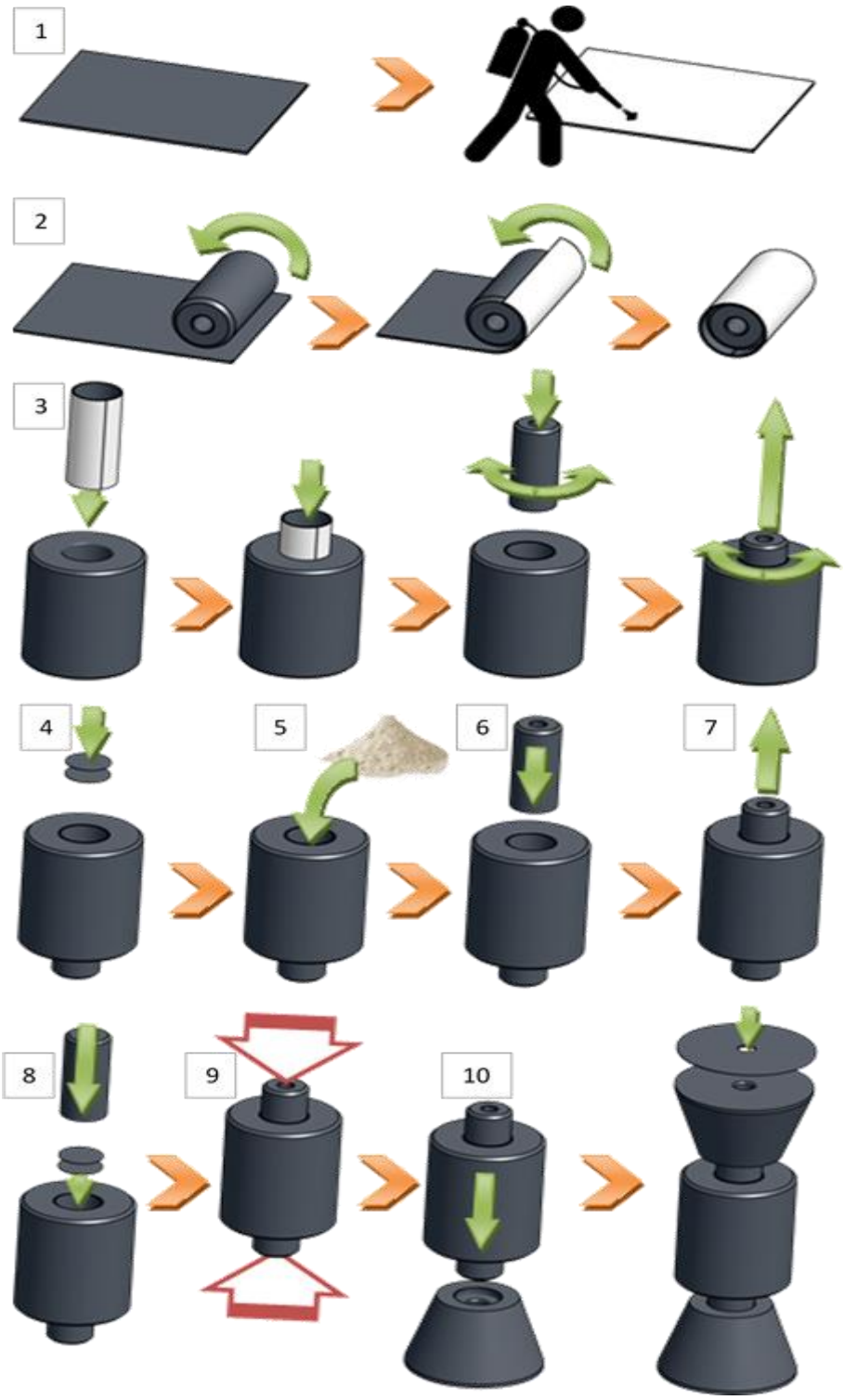

Fig. 19 The whole procedure of the SPS sample forming into a graphite die.

3.5. Analytical methods

All analytical and measuring techniques summarized below were used in the different phases of the experiments described in the later chapters. The basic information and type of measuring device will be described here, the additional information will be given later in the relevant experimental part.

3.5.1. Secondary electron microscopy

Morphology of ceramic powders and bulk bodies were studied by secondary electron microscope (SEM) Philips XL30 (Netherland). Samples of bulk ceramics were polished, thermally etched (usually 50 °C bellow the sintering temperature for 3 min). The contrast was in some cases enhance by Au-Pd layer. If needed, tentative chemical compositions of observed samples were established by Energy-Dispersive X-ray spectroscopy (EDX).

3.5.2. X-ray diffraction

The phase compositions were determined by 3 types of X-ray diffractometers. The first two were PANalytical X'Pert Pro MPD, powered by a Philips PW3040/60 X-ray generator and fitted with an X'Celerator* detector. Diffraction data were acquired by exposing samples to Cu-Kα X-ray radiation, which has a characteristic wavelength λ = 1.5418 Å (University Duisburg-Essen) resp. λ = 1.5405 Å (CNR Genova). X-rays were generated from a Cu anode supplied with 40 kV and a current of 40 mA. Another type of PANalytical X'Pert device (Co–Kα_1; λ = 1.78892 Å) was used for XRD analysis at Brno University of Technology. Phase identification was carried out by software PANalytical High Score Plus.

3.5.3. Nitrogen adsorption

The specific surface area of ceramic powders S_{BET} [m^2/g] was established by nitrogen adsorption with ChemBET 3000 (Quantachrome, USA) device. From the S_{BET} value can be calculated approximate diameters for the ball shaped particles D_{BET} [m] according following equation (Eq. 19).

$$D_{BET} = \frac{6}{S_{BET} \cdot \rho_{theor}} \; [m] \tag{19}$$

3.5.4. Mercury intrusion porosimetry

The size and distribution of the open pores was measured by a mercury porosimeter 440 Pascal (Porotec, Germany). This method works with the principle of low wettability of mercury to most surfaces. Under increasing pressure (up to 330 MPa) the mercury penetrates open pores of decreasing radius (the model calculates with pores of cylindrical shape, higher pressure push the mercury to smaller pores)

Measurements were performed on dried samples under the vacuum. The open pore distribution was used for tentacle comparison of ceramic green body sinterability.

3.5.5. Density measurement

The densities of green as well as fully sintered ceramic bodies were established according Archimedes principle using measuring density kit (EN 623-3). The weights were measured with analytical laboratory scales Mettler Toledo AG 64 (accuracy 0.0001 g). Ceramic samples were firstly dried at 110 °C for at least 30 min and the dry mass was measured. The samples were placed into the vacuum chamber a kept under the vacuum for 30 min and then they were flooded by distilled water. The vacuum was maintained for next 30 min and then let under water at normal pressure again for 30 min. The "soaked" samples were weighted under the water using density kit. The last step was drying out the samples by filtration paper and weighing for the third time. Using these three masses and theoretical density ρ_{theor} [kg·m^{-3}] the relative density ρ_{rel} [%TD], relative open porosity V_{Orel} [vol.%] and relative closed porosity V_{Crel} [vol.%] were calculated.

3.5.6. Infra-red reflectivity

IR reflectivity measurements were performed using a Fourier Transform IR Spectrometer Bruker IFS 113v at room temperature with a resolution of 2 cm^{-1}. The samples were grinded and polished on one side to obtain mirror-like surfaces.

4. Aims of doctoral thesis

According to available literature review in the field of magneto-electric ceramic materials the following aims of doctoral theses were established:

- Preparation of dense phase-pure perovskite ceramics with interesting (multi-)ferroic properties
- Study of influence of the processing route on the final microstructure and the magneto-electric properties of presented materials

The main goal was to utilize the available infrastructure of Department of Ceramics and Polymers and long-year experience for producing of dense and phase pure magnetoelectric materials. The materials were chosen in close cooperation with our research partners for their promising functional physical properties. (Our partners are: Institute of Physics ASCR, University of Duisburg-Essen, Institute for Energetics and Interphases – CNR Genova, Institute of Technical Sciences of SASA – Belgrade). The selected electroceramics materials for the purpose of this thesis are $EuTiO_3$, $Eu(Na)TiO_3$, $MgTiO_3$, $Ba(Ca)Ti(Zr)O_3$.

The main motivation is huge lack of such materials for proper evaluation of "undistorted" physical properties (unaffected by material defects like porosity, pollutants, etc.)

5. $EuTiO_3$

5.1. State of the art

This rare-earth perovskite system exhibits in the bulk form quantum paraelectricity (the ferroelectric behaviour was observed only in the epitaxial thin films under large biaxial compressive strain [48]). It also exhibits anti-ferromagnetic ordering (G-type) below $T_N \approx 5.3K$ [49]. This material belongs to the group of magneto-dielectrics. It means that its permittivity can be tuned by an external magnetic field (see Fig. 20) [50]. Such a behaviour could be used in future capacitors with tunable capacity.

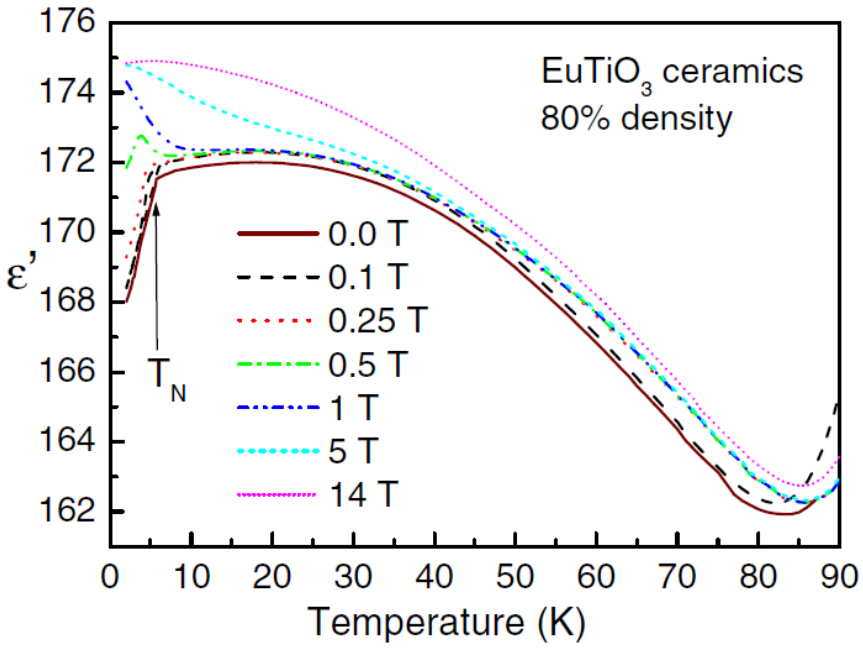

Fig. 20 Temperature dependence of the permittivity in $EuTiO_3$ ceramics measured at 1 kHz and at various magnetic fields. Critical temperature to AFM phase is marked [50].

One of the main problem is that physical characteristics measured on this system are highly sensitive to phase and chemical purity as well as to relative density. In the work of Kamba et al. [50] it was shown, that insufficient relative density of the measured bulk sample reduces the IR reflectivity, therefore it decreases the sensitivity of the measuring (Fig. 21). The presence of secondary phases distorts the shape of spectrum and together with insufficient relative density made the interpretation of measured data difficult or even irrelevant. Europium is sufficiently stable in the divalent state (Eu^{2+}) when substitutes the divalent alkaline earth ion in the perovskite lattice. First processing of europium titanate was published by Bourst et al. in 1953 [51], when a small sample of phase pure Eu_2O_3 was mixed with a stoichiometric amount of TiO_2 (anatase). These oxides were thoroughly mixed together in a mortar,

and then heated up for two hours at 1200 °C in hydrogen atmosphere inside a platinum boat. The product was black and XRD analysis confirms cubic lattice - expected for perovskite $EuTiO_3$.

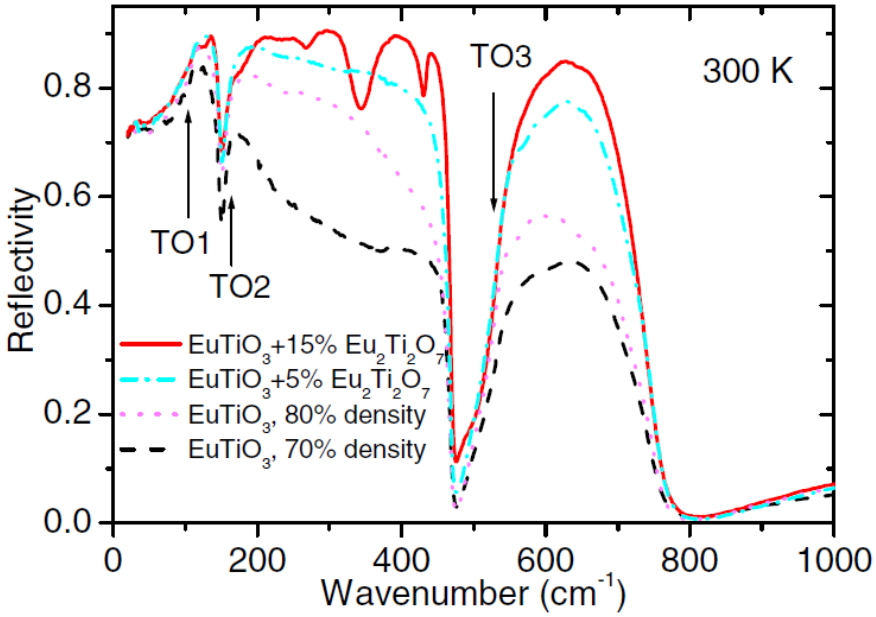

Fig. 21 Room-temperature IR reflectivity spectra of $EuTiO_3$ ceramics. Transverse phonon frequencies of three perovskite modes are marked [50].

Similar solid state reaction of powder oxide precursors in reducing atmosphere is usually used for $EuTiO_3$ synthesis [52]. Mostly the final product is a powder or thin film [48, 53], only a few publications deal with a bulk body fabrication and often reported problems are high porosity or insufficient phase purity (unsuitable for magneto-electric properties characterization). The clear example of complications during the $EuTiO_3$ bulk ceramics processing is given in the work of Kamba et al. [50]. In this work, stoichiometric amounts of precursors were mechanically activated by planetary ball milling and this mixture was pressed into the pellets by a uniaxial press at 650 MPa or by a cold isostatic press at 300 MPa. These samples were annealed at 1500°C in reducing atmosphere (Ar + 10 % H_2). The resulting $EuTiO_3$ ceramics contained 20-30 % of porosity, therefore these high-porous samples were crushed and milled again until the fine powder was reached. This powder was sintered by SPS at 1150-1200°C for 3-5 min and (uniaxial) pressure 75-100 MPa. Resulting samples exhibited relative density higher than 90 % of theoretical density (90 %TD). Unfortunately the content of secondary pyrochlore phase $Eu_2Ti_2O_7$ (polluting phase) was 5-15 %.

The particular goal of this investigation was to prepare dense bulk $EuTiO_3$ ceramics of high purity, ideal for establishing of its functional properties. According to available experimental infrastructure the solid-state syntheses in different types of atmospheres was chosen.

5.2. Experiments

5.2.1. Precursor materials

Eu_2O_3

This powder material was supplied by Verochem (CZ) and its purity was 99.99 %, the maximal impurity contents are summarized in Table 1. Specific surface area was established by nitrogen adsorption S_{BET} = 7.55 $m^2 \cdot g^{-1}$. According to SEM observation, the powder was consisted of particles of about 100 nm large, what is in agreement with S_{BET} ($D_{BET} \approx 110$ nm). The XRD analysis showed single Eu_2O_3 phase with cubic lattice. The morphology as well as XRD diffractogram are showed in the Attachment (A-Fig. 1 and A-Fig. 2).

Table 1 Maximal content of impurities in Eu_2O_3 (Ver) powder.

	[10^{-4} wt.%]		[10^{-4} wt.%]		[10^{-4} wt.%]
Sm_2O_3	5	Gd_2O_3	5	Tb_4O_7	5
Ho_2O_3	5	Er_2O_3	5	Tm_2O_3	5
Lu_2O_3	5	Y_2O_3	5	CaO	9
Fe_2O_3	3	SiO_2	19	PbO	3
CuO	3	NiO	3	Dy_2O_3	5
Yb_2O_3	5	ZnO	5	Cl	80

Ti_2O_3

This powder material was supplied by Verochem (CZ) and its purity is 99.9%, the maximal impurity contents are summarized in Table 2. Specific surface area was established by nitrogen adsorption S_{BET} = 0.46 $m^2 \cdot g^{-1}$. According to SEM observation, the powder consists of particles of about 10 μm large, which are crating agglomerates up to 60 μm. The disagreement of these values with S_{BET} ($D_{BET} \approx 2.9$ μm) are caused by irregular shape of particles (agglomerates). The XRD analysis showed single Ti_2O_3 phase with rhombohedral lattice. The morphology and XRD diffractogram are showed in the Attachment (A-Fig. 3 and A-Fig. 4).

Table 2 Maximal content of impurities in Ti_2O_3 (Ver) powder.

	[10^{-4} wt.%]		[10^{-4} wt.%]		[10^{-4} wt.%]
Si	45	Fe	30	Al	450
Cr	10	Ni	3	Ca	10
Cu	10	Zr	10	Mg	78
S	320	Mn	11	Sn	3.8
C	340				

TiO_2-A

This powder material was supplied by Verochem (CZ) and its purity is 99.99%, the maximal impurity contents are summarized in Table 3. Specific surface area was established by nitrogen adsorption S_{BET} = 9.75 $m^2 \cdot g^{-1}$. According to SEM observation, the powder consists of particles of about 200 nm large, what is in agreement with S_{BET} ($D_{BET} \approx 150$ nm). The XRD analysis showed single TiO_2 anatase phase with tetragonal lattice. The morphology as well as XRD diffractogram are showed in the Attachment (A-Fig. 5 and A-Fig. 6).

Table 3 Maximal content of impurities in TiO_2-A (Ver) powder.

	[10^{-4} wt.%]		[10^{-4} wt.%]		[10^{-4} wt.%]
Si	45	Na	10	Zn	10
Al	10	Co	10	Cr	10
Mg	10	Cu	50	Mg	78
Fe	50	Mn	11	Ca	20
K	10	As	10	Pb	10
Li	10	Ni	10	V	10

TiO_2-R

This powder material was supplied by Verochem (CZ) and its purity is 99.99%, the maximal impurity contents are summarized in Table 4. Specific surface area was established by nitrogen adsorption S_{BET} = 3.40 $m^2 \cdot g^{-1}$ ($D_{BET} \approx 440$ nm). According to SEM observation, the powder is consisted of the particles of about 800 nm large, which are agglomerated to blocks with size up to 6 μm. The XRD analysis showed single TiO_2 rutile phase with tetragonal lattice. The morphology as well as XRD diffractogram are showed in the Attachment (A-Fig. 7 and A-Fig. 8).

Table 4 Maximal content of impurities in TiO_2-R (Ver) powder.

	[10^{-4} wt.%]		[10^{-4} wt.%]		[10^{-4} wt.%]
Si	1	Ni	5	Zn	2
Na	2	Al	2	Cr	1
Co	1	Cu	20	Mg	2
K	3	Ca	5	Fe	10
As	2	Pb	10	V	10

5.2.2. Powder mixture processing

Stoichiometric calculations

According the chemical Eq. 20 the mass ratio of the powder compounds in the mixture 1 (MIX 1) was established (Eq. 21 for Eu_2O_3 and Eq. 22 for Ti_2O_3). The same calculations (Eq. 24 for Eu_2O_3 and Eq. 25 for TiO_2) were proceed for the Eq. 23 which is valid for mixture 2 (MIX 2) with anatase and mixture 3 (MIX 3) with rutile. The basic chemical composition of individual mixtures is summarized in the Table 5.

Table 5 Summary of the chemical composition of individual mixtures.

Mixture #	Composition
MIX 1	Eu_2O_3 + Ti_2O_3
MIX 2	Eu_2O_3 + TiO_2-A
MIX 3	Eu_2O_3 + TiO_2-R

$$Eu_2O_3 + Ti_2O_3 \Leftrightarrow 2 \cdot EuTiO_3 \tag{20}$$

$$w(Eu_2O_3) = \frac{M(Eu_2O_3) \cdot 100}{M(Eu_2O_3) + M(Ti_2O_3)} = \frac{351.917 \cdot 100}{351.917 + 143.757} \doteq 70.998[wt\%] \tag{21}$$

$$w(Ti_2O_3) = \frac{M(Ti_2O_3) \cdot 100}{M(Eu_2O_3) + M(Ti_2O_3)} = \frac{143.757 \cdot 100}{351.917 + 143.757} = 29.002[wt\%] \tag{22}$$

$$Eu_2O_3 + 2 \cdot TiO_2 + H_2 \Leftrightarrow 2 \cdot EuTiO_3 + H_2O \tag{23}$$

$$w(Eu_2O_3) = \frac{M(Eu_2O_3) \cdot 100}{M(Eu_2O_3) + 2 \cdot M(TiO_2)} = \frac{351.917 \cdot 100}{351.917 + 2 \cdot 79.878} \doteq 68.778[wt\%] \tag{24}$$

$$w(TiO_2) = \frac{2 \cdot M(TiO_2) \cdot 100}{M(Eu_2O_3) + 2 \cdot M(TiO_2)} = \frac{2 \cdot 79{,}878 \cdot 100}{351.917 + 2 \cdot 79.878} \doteq 31.222[wt\%] \tag{25}$$

Homogenisation of mixtures

The mixtures MIX 1, MIX 2 and MIX 3 with the composition calculated above were homogenized manually in agate mortar for 15-20 min in 4-5 g batches (only in the case of some initial experiments). Otherwise, these mixtures were

homogenized by planetary ball milling for 10 hour to decrease the possible negative effect of wide particle size distribution of input powders. Zirconia balls (∅5mm) were used as milling elements in the zirconia resp. polyamide (PA) bowls. The milling was performed in an isopropanol (wet conditions) and the ratio between masses of powder mixture and milling elements was 1:10.

Drying and additional mechanical treatment

The resulting suspensions were dried for 48 hour at room temperature followed by 2 hours at 80 °C. The powder mixtures formed large blocks (approx. 1-10 mm^2 with thickness ca 2 mm). Such a form was unsuitable for following shaping process, so next 15 min of mechanical treatment in the agate mortar for each mixture was performed.

Annealing

The powder mixtures (MIX 1-3) were annealed in reducing atmosphere Ar + 7 % H_2 at 700 °C for 2 hours with heating and cooling rates 15 $°C \cdot min^{-1}$ respective in the pure H_2 atmosphere (other conditions remained same).

5.2.3. Green body shaping

The shaping of a green body is the key step in the bulk ceramic processing. The shaping method should be optimal for the following sintering technique, therefore two shaping methods were used in following experiments (one for *"conventional sintering"* and second for *"spark-plasma sintering"*). The homogenized and dried mixtures 1-3 (without annealing) were used as starting powder material for all bulk body processing experiments.

Green body shaping for conventional sintering

The forming of the green bodies from MIX 1-3 was performed by cold isostatic pressing (Fig. 14 – right). Powder was placed in the cylindrical (∅30 mm – 5 mm) latex mold, which was then isostatically pressed at 300 MPa for 5 min. The flexibility of the mold caused the irregularity of the final shape, so following shape correction (hand-operated mechanical grinding) was performed.

Green body shaping for SPS

The mixtures homogenized by planetary ball milling as well as manually in a mortar were used as a starting powder materials. In the case of all experiments included in this work, the graphite die with two piston layout and inner diameter 18 mm was used. Graphite die filled by desired powder mixture was pressed by the force of 3000 N in the uniaxial press (Fig. 14 – left), therefore the pressure used for green body forming (before sintering) was approximately 12 MPa.

5.2.4. Sintering

Conventional (pressureless) sintering

Initial sintering experiments of isostatically pressed bodies were performed in the mixed atmosphere of argon and hydrogen (Ar + 7% H_2) at the temperature 1500 °C for 2 hours (Fig. 17 – middle). The heating and cooling rates were 15 °C·min^{-1}. The experiments were performed in stationary atmosphere (1 bar). The pressure chamber was three times vacuumed and then again filled by desired atmosphere before each experiment (to minimalize the content of residual oxygen).

Following set of experiments was performed in the pure hydrogen atmosphere (100% H_2) at the temperature 1300 °C, 1400 °C, 1500°C resp. 1650°C for 2 hours. The heating and cooling rates were again 15 °C·min^{-1}. In the case of experiment at 1500°C only sample prepared from MIX 2 was sintered due to insufficient amount of powder precursors. Samples were placed into the airtight furnace (Fig. 17 – right), which was then kept under nitrogen flow for 20 min to prevent residual oxygen presence. The chamber was then heated to the sintering temperature under constant flow of hydrogen (1.1 bar).

Spark plasma sintering

During SPS experiments (see Fig. 18) the sintering temperature was 1100 °C – 1500 °C with dwell time 1 – 10 min and uniaxial pressure 10 – 40 MPa. The heating and cooling rates were 100 °C·min^{-1}. The whole sintering regime ran under vacuum of ca 100 Pa (residual argon atmosphere). The airtight chamber was three times vacuumed and then again filled by argon atmosphere to minimalize the content of residual oxygen.

5.3. Results

5.3.1. Milling of powder mixtures

The morphologies of resulted mixtures are shown in the A-Fig. 9, A-Fig. 10 and A-Fig. 11. A mechanical energy of milling was sufficient for breaking most of the agglomerates of the input powder materials. The energy of milling was insufficient to decrease primary particle sizes except Ti_2O_3 powder.

The phase composition of all the mixtures was checked by XRD diffraction measurements. The resulting diffractograms showed only unreacted mixtures of entering powder materials without any sign of contamination during mixtures processing.

5.3.2. Annealing of powder mixtures

The temperature and/or reduction potential of atmospheres were not sufficient (from the thermodynamic point of view) for successful solid state reaction according Eq. 19 resp. Eq. 22 in any of annealing experiments. The only observed change in the

phase composition was partial reduction of TiO_2 (MIX 2 - anatase and MIX 3 - rutile) to Ti_2O_3. Example of this phase composition change is shown in Fig. 22 (MIX 3 in Ar + 7 % H_2). Any significant differences were observed in case of annealing experiments in H_2 atmosphere (the same temperatures and dwell times).

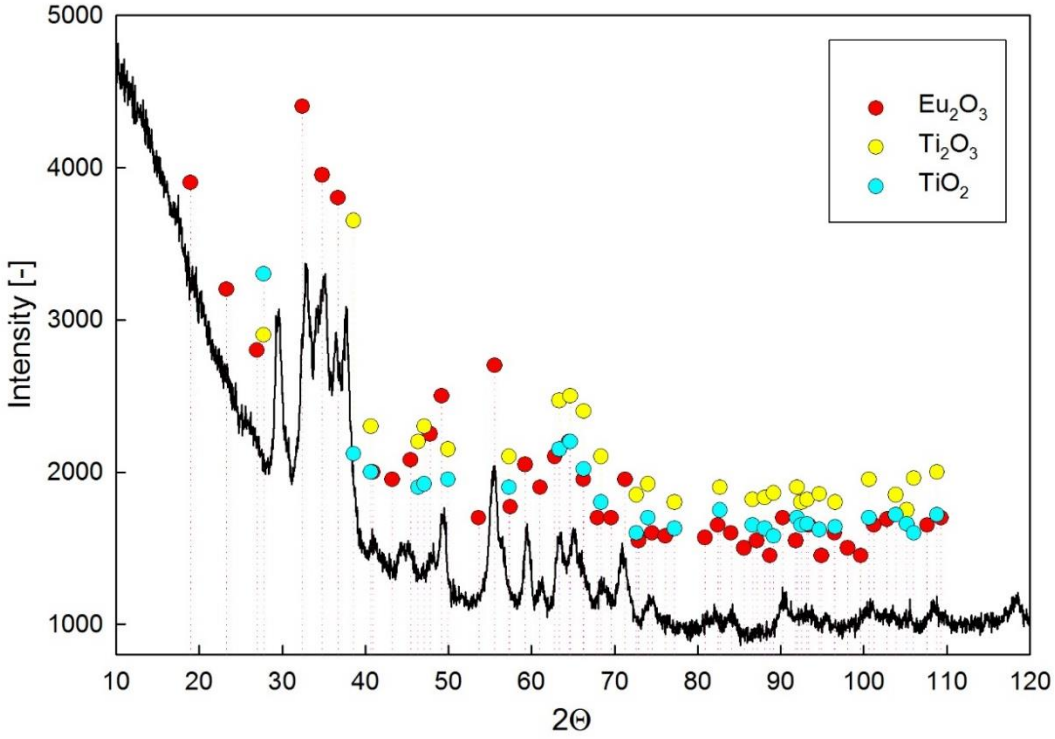

Fig. 22 Phase composition of MIX 3 after annealing at 700 °C in Ar + 7 % H_2 atmosphere.

5.3.3. Processing of bulk bodies

Conventional pressure-less sintering

The pores size distribution in the cold isostatic pressed bodies was measured to evaluate the sinterability of the green bodies. All samples exhibited unimodal pore size distribution, so the sinterability was evaluated from the size of the biggest pores presented in the samples. In case of the sample from MIX 1 the pore size distribution ended around 80 nm (pore radius 40 nm). The samples prepared from MIX 2 and MIX 3 had almost the same pore size distribution with the biggest values around 60 nm (pore radius 30 nm). These results (except porosity of MIX 3) are shown in the Fig. 23 together with one sample which was prepared from MIX 2 and homogenized in polyamide bowl (other parameters of green body processing were identical). This difference shows the importance of using ZrO_2 milling bowls for proper de-agglomeration and homogenization of powder precursors.

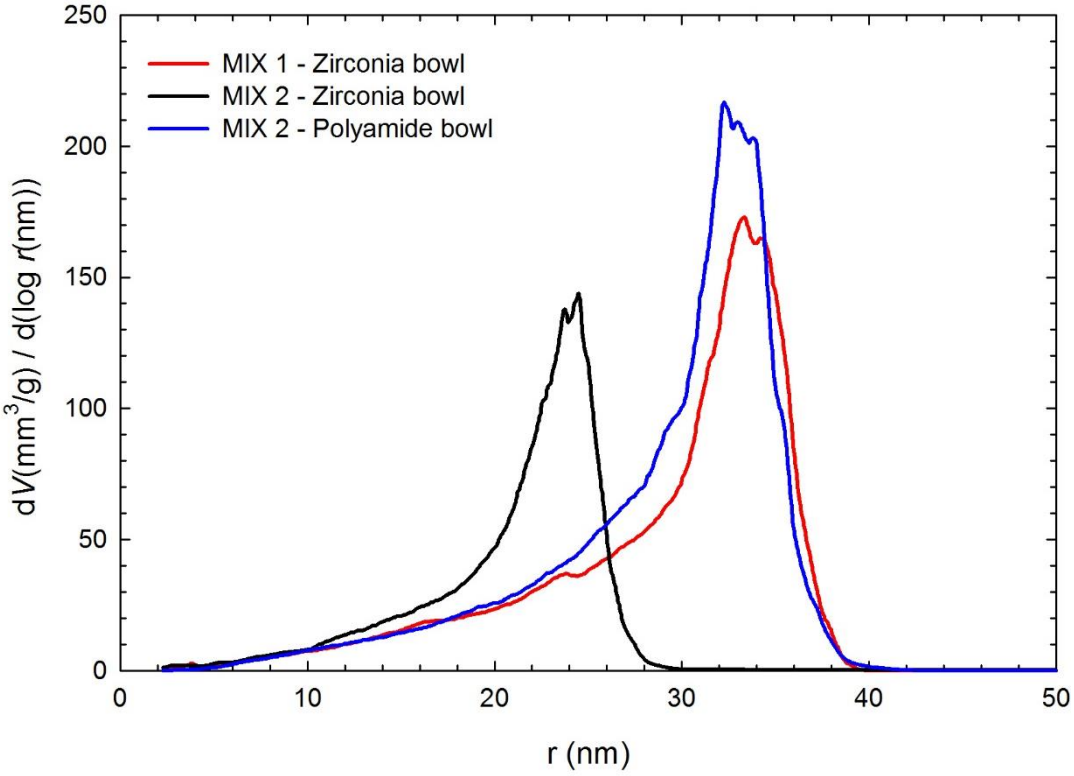

Fig. 23 The pore size distribution of cold isostatic pressed bodies (300 MPa).

The phase compositions of all sintered samples contained the single perovskite phase $EuTiO_3$. The example of XRD diffractogram is shown in Fig. 24.

Relative sample density and open (Vo_{rel}) to close (Vc_{rel}) porosity ratio strongly depended on the sintering temperature (Table 6). With increasing sintering temperature the content of open porosity decrease up to 1500 °C, at higher temperature open porosity surprisingly raised again (the probable reason is discussed in the next chapter - 5.4). At 1400 °C the open porosity change into a closed one as the relative density of samples exceed 90 %TD. The exception is the sample prepared from MIX 1 which relative density is still below 90 %TD at 1400 °C. The porosity is also strongly depended on sintering atmosphere, as it can be seen in the case of samples sintered in slightly reducing atmosphere Ar + 7 % H_2. Whereas the closed porosity content do not exceed the value of 10 vol.% (samples sintered in pure H_2), the closed porosity was over this level in the case of this batch of samples.

From the three starting mixtures with the same atomic ratios the MIX 2 and MIX 3 reaches significantly higher densities than the MIX 1. The highest values of final density 95 %TD was reached at the temperature of 1400 °C for 2 h in the pure H_2 atmosphere with MIX 2 (Eu_2O_3 + TiO_2-A).

This sample had homogenous microstructure with grain size approx. 1–5 μm and closed pores had diameter approx. 1 μm (see Fig. 25). According author's best knowledge, it is up to now the best bulk $EuTiO_3$ ceramic sample.

Table 6 Summary of pressure-less sintering experiments results.

Type of mixture	Sintering		ρ_{rel}	Vo_{rel}	Vc_{rel}	Phase composition
	Temperature	Atmosphere	[%TD]	[vol.%]	[vol.%]	
MIX 1	1300 °C	H_2	75.4	24.3	0.3	$EuTiO_3$
MIX 2	1300 °C	H_2	88.2	10.3	1.5	$EuTiO_3$
MIX 3	1300 °C	H_2	87.4	11.2	1.4	$EuTiO_3$
MIX 1	1400 °C	H_2	88.7	10.7	0.6	$EuTiO_3$
MIX 2	1400 °C	H_2	95.1	0.8	4.1	$EuTiO_3$
MIX 3	1400 °C	H_2	93,4	0.7	5.9	$EuTiO_3$
MIX 2	1500 °C	H_2	93.6	0.7	5.7	$EuTiO_3$
MIX 1	1500 °C	Ar + 7 % H_2	88.5	0.1	11.4	$EuTiO_3$
MIX 2	1500 °C	Ar + 7 % H_2	71.1	0.3	28.6	$EuTiO_3$
MIX 3	1500 °C	Ar + 7 % H_2	71.6	1.4	27.0	$EuTiO_3$
MIX 1	1650 °C	H_2	86.5	4.7	8.9	$EuTiO_3$
MIX 2	1650 °C	H_2	75.1	18.2	6.7	$EuTiO_3$
MIX 3	1650 °C	H_2	71.2	22.1	6.7	$EuTiO_3$

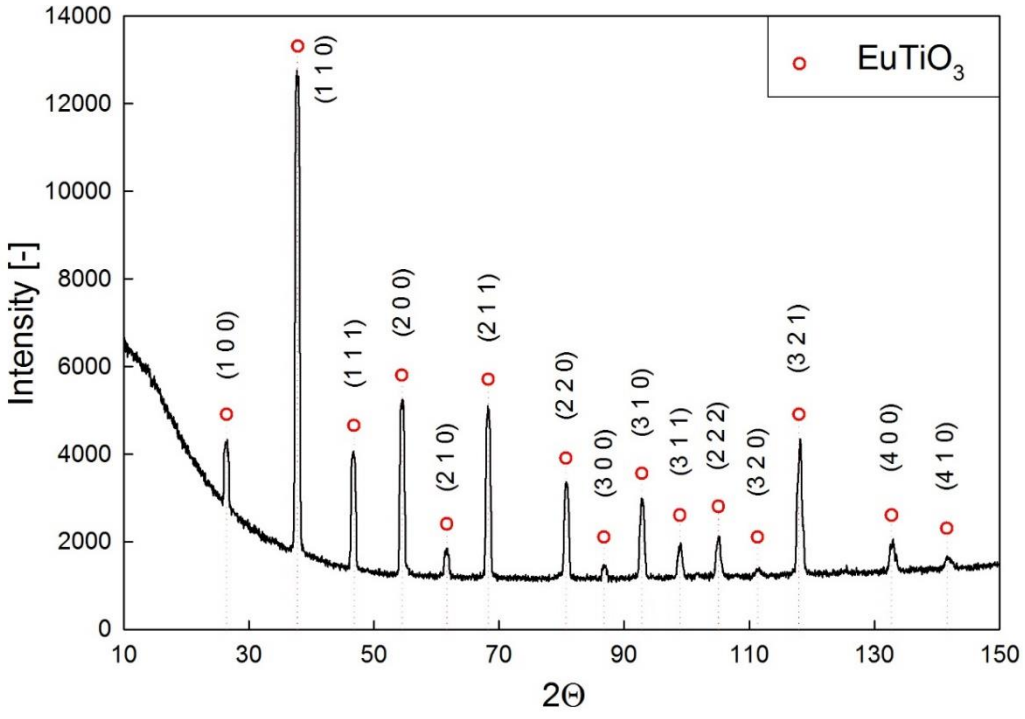

Fig. 24 XRD of the sample from MIX 2 sintered at 1400°C in the pure H_2

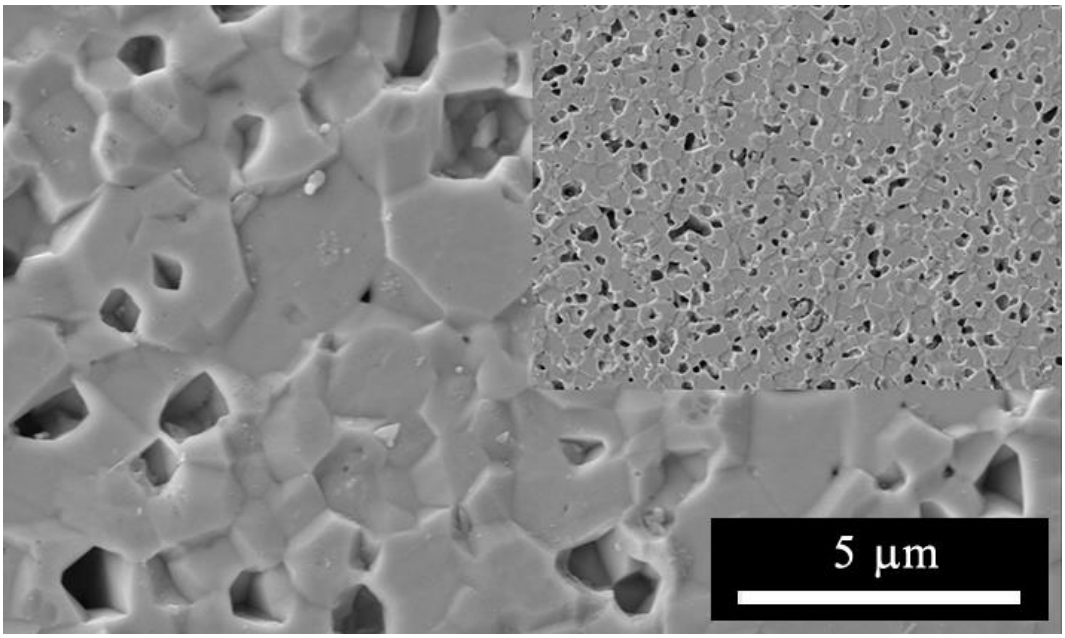

Fig. 25 The microstructure of bulk $EuTiO_3$ single phase sample with relative density 95 %TD (MIX 2 / 1400 °C / 2h / H_2).

Spark-plasma sintering

The XRD analyses of all samples prepared by SPS showed the presence of unwanted phases - $Eu_2Ti_2O_7$, Eu_2TiO_3 or unreacted compounds of starting mixtures (the example of sample containing significant amount of polluting pyrochlore phase is given in Fig. 26).

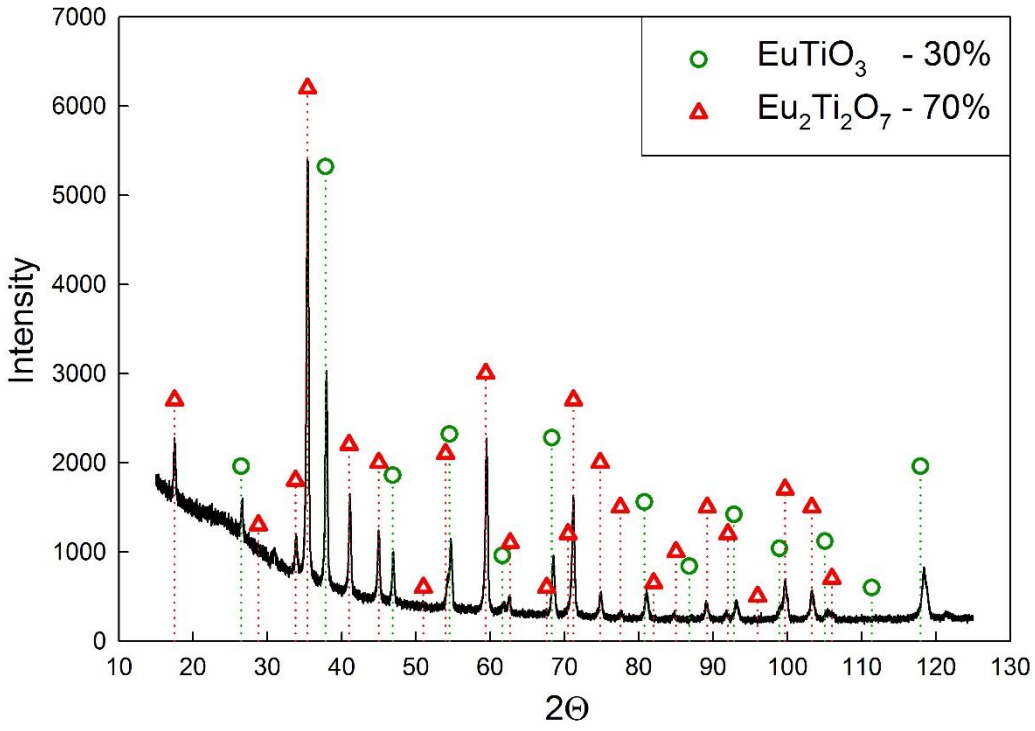

Fig. 26 XRD pattern of ETO sample prepared from the MIX 1 and sintered in SPS.

Establishing of the theoretical density value was highly inaccurate due to multi-phase composition of the samples. The values of relative density should be taken only as approximate. The results of the experiments with manually homogenized mixtures are summarized in Table 7 and with mixture homogenized by planetary ball mill in Table 8.

In the case of MIX 1, the content of secondary phases was in the range of 3 – 83 vol.% decreasing with sintering temperature increase and longer dwell time. The values of relative densities were in the range of 75 – 93 %TD.

The solid-state syntheses of the samples prepared from the MIX 2 did not lead to $EuTiO_3$ perovskite phase formation. The samples contained mostly unwanted pyrochlore phase $Eu_2Ti_2O_7$.

The sample with the lowest content of secondary phases was prepared from manually homogenized MIX 1 sintered firstly at 850 °C for 5 min followed by 3 min at 1300 °C and pressure 20 MPa. The content of polluting Eu_2TiO_3 was approx. 3 vol.%, but the relative density was only 82 %TD. The following experiment with doubled pressure (40 MPa) exhibited significantly improved relative density – 91 %TD, but the content of secondary phase was increased to 5 vol.%. The extension of the dwell time at the first step (850 °C) to 15 min and increasing sintering temperature to 1400 °C led to even higher relative density value – 93 %TD, but again with slightly increased secondary phase content (7 vol.%).

Table 7 Summary of following SPS sintering experiments at different temperatures and dwell times with manually homogenized mixtures.

Type of mixture	Sintering temp. [°C]	Dwell time [min]	Uniax. pressure [MPa]	ρ_{rel} [% TD]	Phase composition
MIX 1	800 / 1100	8 / 10	40	80	70% $EuTiO_3$ + $Eu_2Ti_2O_7$ + Ti_2O_3 + Eu_2O_3
	1200	3	40	89	90% $EuTiO_3$ + $Eu_2Ti_2O_7$ + Ti_2O_3 + Eu_2O_3
	850 / 1300	5 / 3	40	91	95% $EuTiO_3$ + Eu_2TiO_3
	850 / 1300	5 / 3	20	82	97% $EuTiO_3$ + Eu_2TiO_3
	850 / 1400	15 / 3	40	93	93% $EuTiO_3$ + Eu_2TiO_3
MIX 2	1200	3	40	93	70% $Eu_2Ti_2O_7$ + TiO_2 + Eu_2O_3
	1100 / 1500	1 / 3	40	95	80% $Eu_2Ti_2O_7$ + Ti_3O_5 + Eu_2O_3

Table 8 Summary of initial SPS sintering experiments at different temperatures and dwell times with mixtures homogenized by planetary mill.

Type of mixture	Sintering temp. [°C]	Dwell time [min]	Uniax. pressure [MPa]	ρ_{rel} [% TD]	Phase composition
MIX 1	900 / 1200	17 / 3	40	92	30% $EuTiO_3$ + $Eu_2Ti_2O_7$
	1050 / 1200	17 / 7		94	30% $EuTiO_3$ + $Eu_2Ti_2O_7$
	1250 / 900	1 / 15		94	17% $EuTiO_3$ + $Eu_2Ti_2O_7$
	1100 / 1350	10 / 5		94	30% $EuTiO_3$ + $Eu_2Ti_2O_7$
	1050 / 1400	17 / 7		84	80% $EuTiO_3$ + $Eu_2Ti_2O_7$

Infra-Red reflectivity

The IR reflectivity was measured on the densest samples sintered at 1400 °C in pure hydrogen atmosphere for 2 hours by conventional pressure-less sintering.

The dependence of IR reflectivity on relative density is shown in Fig. 27, the results are also compared with the literature data [50]. It can be seen that the shape of IR reflectivity did not change, but with the higher density the IR reflectivity increased significantly. The sample with relative density 95 %TD reached a reflectivity of 0.95 at wavenumbers ranging from 200 to 400 cm^{-1}.

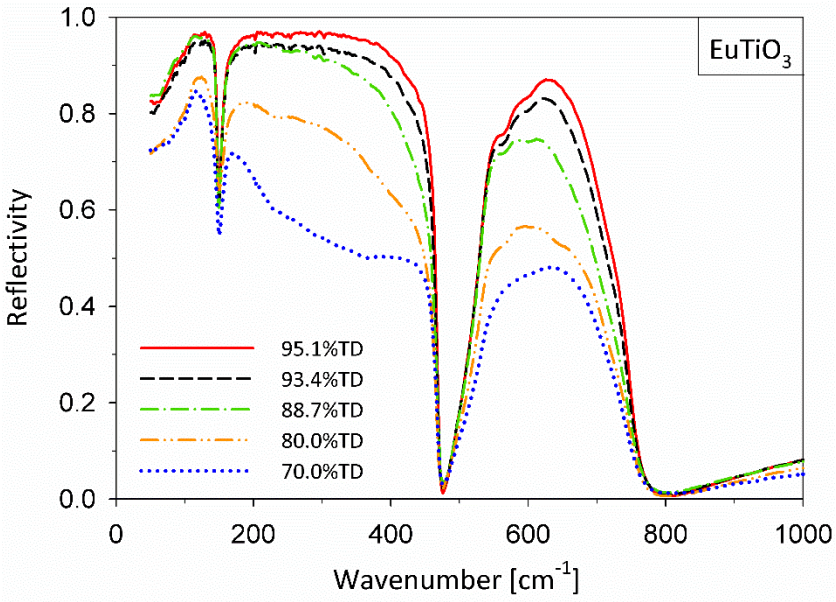

Fig. 27 Room-temperature IR reflectivity spectra of $EuTiO_3$ ceramics with: Left - relative density 70%* , 80%*, 88.7%, 93.4%, resp. 95.1% (*[50]).

The results of IR reflectivity of the sample mentioned above were also compared with samples, which were contaminated by 5 vol.% and 15 vol.% of pyrochlore phase [50]. All these samples had a relative density higher than 91 %TD, so the influence of relative density on IR reflectivity is minimalized. The presence of 15 % of $Eu_2Ti_2O_7$ is demonstrated by additional reflection bands between 100 and 450 cm^{-1}, see Fig. 28.

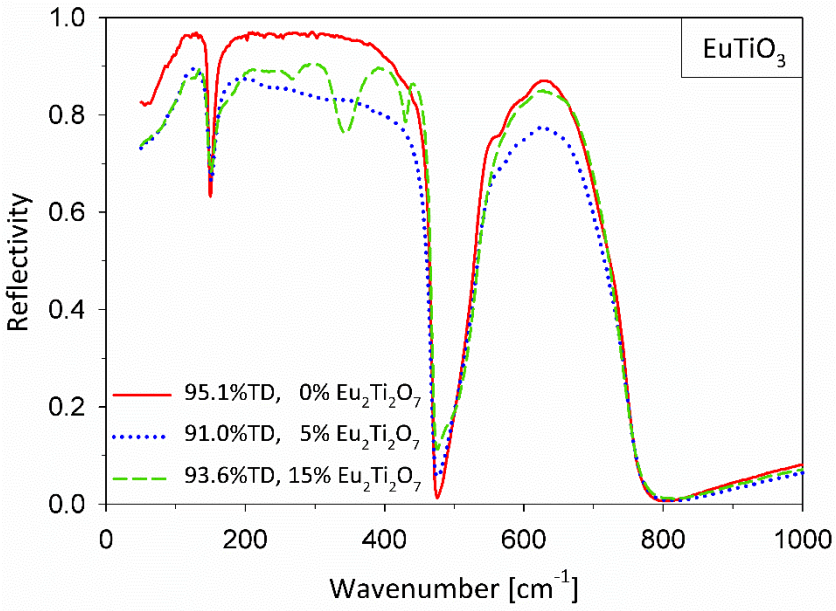

Fig. 28 Room-temperature IR reflectivity spectra of $EuTiO_3$ ceramics with: Right - $Eu_2Ti_2O_7$ phase impurity 0%, 5%* , resp. 15%* (*[50]).

The chosen samples were also used for studying of lattice instabilities [54] and anti-ferrodistortive phase transition [55] in the bulk $EuTiO_3$ ceramics by collaborated international partners.

5.4. Discussion

5.4.1. Milling of powder mixtures

A mechanical energy of milling was sufficient for thorough mixing of the input powder materials and breaking most of the agglomerates. This is very important for uniform solid state reaction. The proper homogenization process was also proven by following high temperature solid-state reaction, which successfully formed single phase bulk $EuTiO_3$ ceramics.

5.4.2. Annealing of powder mixtures

Any annealing experiment of powder mixtures would lead to particle growth. This concomitant phenomenon would be acceptable in the case of successful solid-state reaction, but the in this case the precursors did not undergo the reactions described by

Eq. 19 resp. Eq. 22. The green bodies and following sintered bodies prepared from mixtures with grown particles would reach lower densities than samples prepared from starting mixtures. That is why the annealed mixtures were not used for bulk body experiments described above.

5.4.3. Processing of bulk ceramics

Presented results confirmed the need of highly reducing conditions during solid-state syntheses of $EuTiO_3$ perovskite ceramics. Also other conditions such as proper homogenization of fine powder precursors, suitable green-body formation technique or optimal sintering temperature and dwell time need to be fulfilled for the successful processing of phase pure bulk $EuTiO_3$ ceramic material with high relative density. The thermodynamic data which would allow calculation of the conditions needed for reaction of used precursors are not available. From that point of view, the experimental investigation and optimization of the whole process was the only possible way.

Conventional pressure-less sintering

As it was already written in the "Results part", the thermodynamic conditions of all pressure-less sintering experiments (temperature and partial pressure of H_2) were sufficient for the $EuTiO_3$ phase formation and the dwell time (2 hours) was long enough for precursors to react through whole volume of all samples. That is also why more attention is paid to relative density evolution in this part of discussion.

Increasing of temperature from 1300 °C to 1400 °C led to significant increase of relative density, but further increase of sintering temperature up to 1500 °C unexpectedly lowered the final densities. Looking more closely at the open to closed porosity ratio reveals that the decrease of density was probably caused by defects forming inside the sintered body. The probable reason for the formation of these defects was oxygen deficiency in $EuTiO_3$ caused by its reaction with hydrogen. The product of this reductive reaction is then water vapour (see Eq. 26), which forms bubbles in the samples. The densities reached after sintering at 1650 °C were quite similar to the densities after sintering at 1500 °C, but the volume of open porosity increased significantly. At this temperature the chemical reaction leading to gaseous products could be so intensive that the internal defects spread into the outer surface of the samples. These samples contained significant amount of surface cracks, which support this hypothesis.

$$EuTiO_3 + \delta \cdot H_2 \Leftrightarrow EuTiO_{3-\delta} + \delta \cdot H_2O \qquad (26)$$

Spark-plasma sintering

The experimental results showed that the sintering of $EuTiO_3$ ceramics in SPS equipment resulted in samples with pyrochlore ($Eu_2Ti_2O_7$) secondary phase (impurity). Unfortunately the thermodynamic data of $EuTiO_3$ and $Eu_2Ti_2O_7$ allowing the direct calculation of probability of Eq. 27 are not available in the literature or in the thermodynamic databases.

$$2 \cdot EuTiO_3 + \frac{1}{2} O_2 \Leftrightarrow Eu_2Ti_2O_7 \tag{27}$$

Reduction potential of these two sintering atmospheres (in the conditions of SPS and conventional sintering) was compared by thermodynamic calculations in the work of Maca et al. [56]. As the CO is the most stable atmosphere in graphite furnace at the temperatures higher than 800 °C [57], the oxidization of $EuTiO_3$ in SPS furnace can be described by the Eq. 28. In the case of pressure-less sintering in pure or mixed hydrogen atmosphere the oxidization of $EuTiO_3$ can be described by Eq. 29.

$$2 \cdot EuTiO_3(s) + CO(g) \Leftrightarrow Eu_2Ti_2O_7(s) + C(s) \tag{28}$$

$$2 \cdot EuTiO_3(s) + H_2O(g) \Leftrightarrow Eu_2Ti_2O_7(s) + H_2(s) \tag{29}$$

When the Eq. (29) is subtract from Eq. (28), the reduction activity of CO and H_2 can be compared (see Eq. 30) and decided which atmosphere is more suitable for prevention of the pyrochlore formation. For such a calculation the Gibbs free energy of this reaction can be described according to Van't Hoff isotherm [58, 59], where the $\Delta G_{r,1400}$ is the Gibbs free energy of the reaction at 1400 K (Eq. 31).

$$CO(g) + H_2(g) \Leftrightarrow C(s) + H_2O(g) \tag{30}$$

$$\mathrm{G}_{\mathrm{r},1400} = \mathrm{G}^{0}_{\mathrm{r},1400} + R \cdot T \cdot \ln \frac{a_{H_2O} \cdot a_C}{a_{H_2} \cdot a_{CO}} \tag{31}$$

The $\Delta G^0_{r,1400}$ is the Gibbs free energy of the reaction described by Eq. 30 (its value is 65 kJ [60]) in case that all reactants are in standard state (for gases it means the pressure of 10^5 Pa = 1 bar), a_C is the thermodynamic activity of carbon (equal to 1 because the carbon is in pure solid state phase), a_{H2O}, a_{H2} , and a_{CO} are thermodynamic activities of the gaseous reactants (expressed by their partial pressure in bars). For the conditions close to SPS (p_{CO} = 10^{-3} bar) and hydrogen furnace environment (p_{H2} = 1 bar and p_{H2O} = 10^{-4} bar) following results were calculated:

$$\mathrm{G}_{\mathrm{r},1400} = 65{,}000 + 8.314 \cdot 1400 \cdot \ln \frac{10^{-4} \cdot 1}{1 \cdot 10^{-3}} = 38.2 kJ \tag{32}$$

An increase of pressure inside the closed and continuously shrinking pores (at the third sintering stage) [61] were not taken into account in these calculations, but even with the consideration of this factor, the atmosphere in SPS furnace is more reducing than in the hydrogen furnace.

It is in contrast to our experimental results which showed the presence of polluting $Eu_2Ti_2O_7$ only in the case of SPS samples. This disagreement between theory and experiment could be explained by very short dwell times at the sintering temperatures in the case of SPS technique. In such a short time (few minutes) cannot be established thermodynamic equilibrium. In our case it means that $Eu_2Ti_2O_7$ doesn't have enough time to be reduced to $EuTiO_3$. In contrast to SPS, the pressureless sintering in hydrogen furnace took 2 h, which was sufficient time to achieve the thermodynamic equilibrium and the formation of pure $EuTiO_3$ ceramics free of pyrochlore secondary phase.

The precursor particles were covered at least by a monolayer of adsorbed gas - air (the source of oxygen, see Fig. 29). Therefore, the oxidation resulting in the formation of $Eu_2Ti_2O_7$ during the short time in the SPS setup can occur. The pyrochlore phase could be similarly formed even in the hydrogen furnace, but these oxidised polluting phases are reduced to pure $EuTiO_3$ during the long dwell times.

This hypothesis is supported also by the experiments. The amount of pyrochlore was significantly lowered by repeated argon washing cycles which were performed before experiments, when argon has partially replaced adsorbed air.

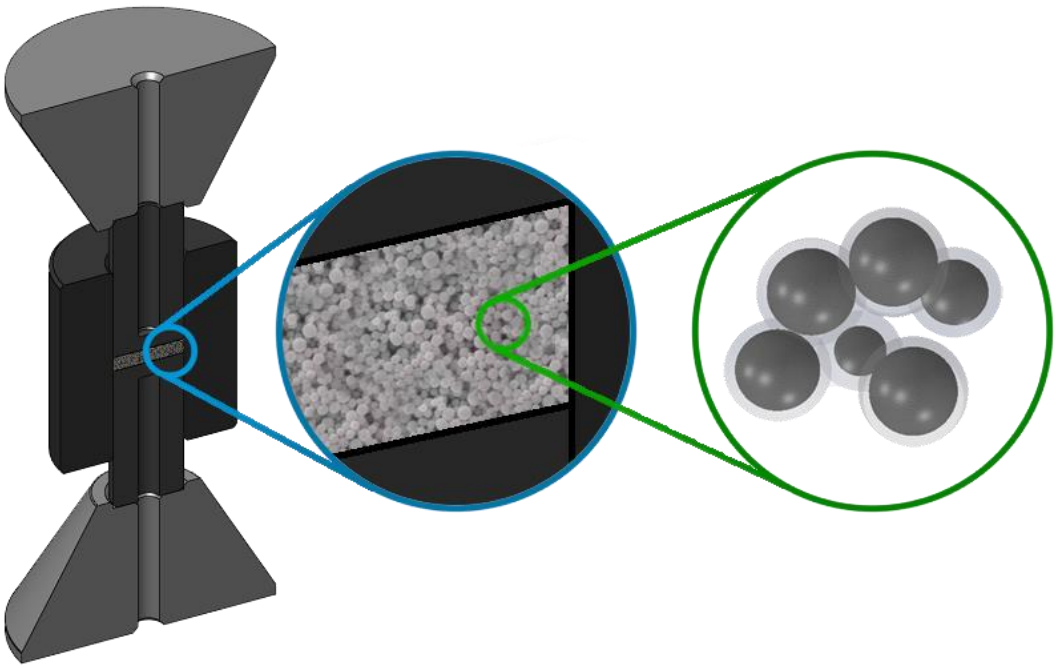

Fig. 29 The scheme of SPS die setup showing the air layer adsorbed on the particles surface before sintering [56].

5.5. Summary

The phase pure and dense bulk $EuTiO_3$ ceramic was prepared by solid-state reaction of powder mixtures of Eu_2O_3 and TiO_2 resp. Ti_2O_3 via optimized pressure-less sintering in reduction atmosphere of pure H_2. The sample with the highest relative density (95.1 %TD) showed IR reflectivity unaffected by phase impurities (secondary phases), and in the frequency range of 200 – 400 cm^{-1} the IR reflectivity was higher than 95 %. Such a ceramic is appropriate for studying the true (not distorted) magnetic and electric properties of this material.

$EuTiO_3$ ceramics has a high affinity to oxygen and forms the unwanted pyrochlore phase even in highly reducing CO atmosphere in the SPS furnace. After pressure-less sintering in hydrogen furnace any marks of secondary pyrochlore phase were not detected by XRD or by IR reflectivity measuring (despite the lower reducing characteristic of hydrogen in comparison with carbon monoxide atmosphere). This can be explained by the longer sintering dwell time in hydrogen furnace which allows to establish thermodynamic equilibrium and therefore pyrochlore decomposition. According authors best knowledge, obtained single phase samples of $EuTiO_3$ bulk ceramics reached the highest relative values published yet.

6. Eu(Na)TiO_3

6.1. State of the art

An alternative approach to solid-state syntheses are "wet syntheses", but according to the best author's knowledge, there is only a couple of papers publishing successful wet syntheses of the $EuTiO_3$ ceramic powder. For example Wei T. et al. [62] describes processing of $EuTiO_3$ nanopowder synthesis by sol-gel technique. The europium oxide (Eu_2O_3) and tetra-butyl titanate ($Ti(OC_4H_9)_4$) were used as a precursors of Eu and Ti ions. The europium oxide was dissolved in the HNO_3 and the tetra-butyl titanate in the 2-methoxyethanol ($C_3H_8O_2$). These two solutions were mixed together and the glycol ($C_2H_6O_2$) in 1:1 molar ratio with respect to the metal nitrates was used as a dispersant. The resulting sol was dried at 90 °C for 3 days to form the gel powder. The product was annealed, firstly at 350°C (air) for 10 h and secondly at 800°C (pure H_2) for 20 min creating single perovskite phase - $EuTiO_3$ powder (Fig. 30).

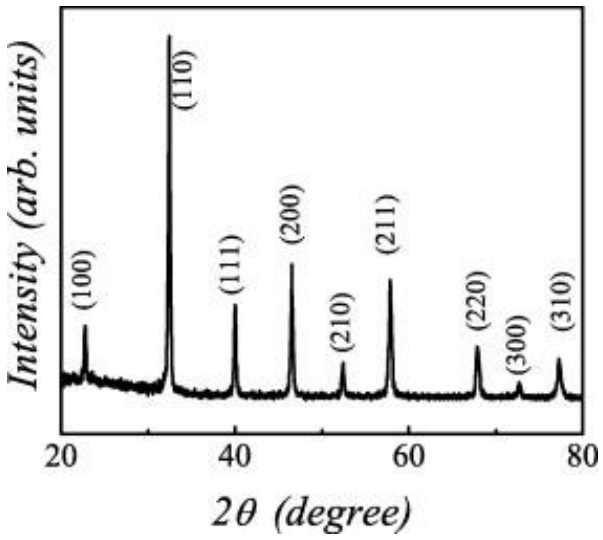

Fig. 30 XRD diffractogram of the single phase $EuTiO_3$ nanopowder [62].

The authors did not mention the amount of synthetized single phase powder and the particle size (100 nm) was established only by TEM. Also they did not publish the phase composition after the "wet synthesis" and after the first annealing step. If the $EuTiO_3$ phase becomes apparent after the second annealing step in hydrogen, the designation of this process as a "sol-gel" or "wet" syntheses of $EuTiO_3$ powder is at least questionable.

Henderson N.L. et al. [63] published another sol-gel syntheses of $EuTiO_3$ powder from Eu_2O_3 and $Ti(iOPr)_4$ as the precursors. Firstly, the Eu_2O_3 was dissolved in a mixture of ethanol and HNO_3 (10:1). Then a stoichiometric amount of $Ti(iOPr)_4$ was added dropwise to the solution, resulting in a clear orange liquid. After stirring for 3 h

resp. 12 h, the solvent was removed by heating to 80°C. Result was a pale orange powder, which was annealed under the flow of reducing atmosphere (5 % H_2 / 95 % Ar) at 1000 °C for 12 h. The change of color from orange to black occurred (because of reduction of Eu from +3 to +2 state). Typical mass of synthetized product was in the range of 0.5 – 1.0 g. The modified sol–gel syntheses were again followed by annealing under reducing conditions (5 % H_2 / 95 % Ar).

The XRD analyses showed single $EuTiO_3$ phase with no evidence of crystalline impurities. On the other hand an observed weight gain upon thermal gravimetric analysis in oxygen indicates that a small amount of Eu^{3+} is present, most likely as an amorphous $EuTiO_x$ phase.

Another titanates with perovskite structure were successfully synthetized hydrothermal syntheses [64-66]. The HTS are usually performed in highly alkaline environment (mostly NaOH or KOH solution). The presence of Na and K ions in the precursor solution could led to forming of systems containing these ions.

According to the authors' best knowledge, whereas $Eu(K)TiO_3$ perovskite ceramic processing was not published up to now, the posibility of $Eu(Na)TiO_3$ system creation was already proven by Ranjan R. et al. [67], when $Eu_{0.5}Na_{0.5}TiO_3$ ceramic was prepared by a solid-state reaction. It is only published successful processing of this material. New way of processing is highly welcomed due to strong sensitivity of measured physical properties on the processing route. Perovskite $Eu_{0.5}Na_{0.5}TiO_3$ ceramic exhibits not well understood phenomenon of quantum paraelectricity at low temperatures (< 50 K). Due to comparatively high saturation temperature in comparison with other known quantum paraelectrics (e.g. $SrTiO_3$), this material is also defined as a "high temperature quantum paraelectric" [68].

6.2. Experiments

6.2.1. Precursor materials

Titanium(IV) chloride

This powder material was manufactured by Sigma-Aldrich and its purity is higher than 99.995 % ($TiCl_4$ - CAS: 7550-45-0).

Hydrazine monohydrate

This water solution precursor was manufactured by Sigma-Aldrich and its purity is in the range of 64-65 % and its reagent grade is 98 % (N_2H_4 - CAS: 7803-57-8).

Sodium borohydride

This powder material was manufactured by Sigma-Aldrich and its purity is 99.99 % ($NaBH_4$ - CAS: 16940-66-2).

Hydrochloric acid

This highly concentrated acid was manufactured by Sigma-Aldrich with concentration range 36.5 - 38.0 % (HCl - CAS: 7647-01-0).

Sodium hydroxide

This granulated material was manufactured by Sigma-Aldrich and its purity is higher than 98 % (NaOH - CAS: 1310-73-2).

6.2.2. Precursor solution processing

Dissolution of the Eu_2O_3 powder in HCl

Hydrochloric acid (37 % HCl) was constantly mixed by the stirring bar in an Erlenmeyer flask (250 ml) at room temperature. The calculated amount of Eu_2O_3 powder (8.798 g) was added during approximately 10 s. The powder residuum in plastic cap was recovered using a small amount of distilled water. The clear colourless solution was then stirred at 60 - 70 °C for 2 h in the fume hood in order to evaporate a residual hydrochloride acid. Distilled water was added into the solution reaching final volume 250 ml of the $EuCl_3$ solution (concentration 2 $mol \cdot l^{-1}$).

Preparation of the syntheses precursors

Calculated amount of $TiCl_4$ water solution (3.9799 $mol \cdot kg^{-1}$) were weighed in a polypropylene bottle. The prepared water solution of $EuCl_3$ (2 $mol \cdot l^{-1}$) was added into it, following the desired ratio of Eu^{+3} and Ti^{+4} ions (1:1, 1:2, 4:9, 2:5 resp. 1:3). Then the NaOH or KOH pellets were added during continuous mixing by stirring bar for 15 min reaching concentration in the precursor solution 1 $mol \cdot l^{-1}$ resp. 10 $mol \cdot l^{-1}$. The bottle was placed into ice bath to avoid increasing of temperature. After adding of the reductant agent N_2H_4 (hydrazine 65 % water solution) or $NaBH_4$ (99.99 %) stirring continued next 30 min. The amount of reductant agent added in the solution was 30 times more than the theoretical amount required for reduction of Eu^{+3} to Eu^{+2}. The theoretical amount was established by calculations (Eq. 35 and 37). Eq. 33, 34 and 36 represent the standard reduction potential $E°$ to Standard Hydrogen Electrode at 25 °C and at pressure of 101.325 kPa.

$$Eu^{3+} + e^- \overset{E^\circ = -0{,}36V}{\Longleftrightarrow} Eu^{2+} \tag{33}$$

$$N_2 + 4H_2O + 4e^- \overset{E^\circ = -1{,}15V}{\Longleftrightarrow} N_2H_4 + 4OH^- \tag{34}$$

$$4(Eu^{3+} + e^-) + (N_2H_4 + 4OH^- - 4e^-) \Leftrightarrow 4Eu^{2+} + N_2 + 4H_2O \tag{35}$$

$$H_2BO_3{}^- + 5H_2O + 8e^- \overset{E^\circ = -1{,}24V}{\Longleftrightarrow} BH_4{}^- + 8OH^- \tag{36}$$

$$8(Eu^{3+} + e^-) + (BH_4{}^- + 8OH^- - 8e^-) \Leftrightarrow 8Eu^{2+} + H_2BO_3{}^- + 5H_2O \tag{37}$$

Syntheses in the hydrothermal vessel

Prepared solutions were moved into stainless steel hydrothermal vessel (Fig. 31) with Teflon insert under Ar flow. The polypropylene cup with stirring bar were washed using 5-13 g of distilled water to prevent losses of high dense precursor solution. After adding this residue into solution, the reactor contained approximately 30 ml resp. 60 ml of liquid.

The hydrothermal reactor was closed under argon atmosphere and placed in the furnace with temperature 220 °C resp. 250 °C. It was presumed from previous experiments that the reactor reached the required temperature approximately after 2 h and the dwell time was set up for next 24 h resp. 72 h. After that the hydrothermal vessel was pulled out of the furnace and left to cool down at the room temperature. The product was washed by distilled water and centrifuged until the neutral pH was reached (usually 6 times). Then two cycles of the same procedure with ethanol were done. The phase composition of the dried powder was measured by XRD.

Table 9 The summary of the main hydrothermal syntheses parameters (temperature, concentration, dwell time and reductant agent type).

Temperature	Dwell time	$EuCl_3$	$TiCl_4$	NaOH	KOH	Reductant agent
[°C]	[h]	[mol×l^{-1}]				[-]
220	26	0.100	0.100	1	-	$NaBH_4$
220	26	0.100	0.100	10	-	N_2H_4
220	26	0.100	0.100	10	-	$NaBH_4$
220	26	0.100	0.200	10	-	N_2H_4
250	26	0.100	-	10	-	N_2H_4
250	26	0.100	0.200	10	-	N_2H_4
250	26	0.100	0.200	10	-	$NaBH_4$
250	26	0.100	0.200	10	-	-
250	26	0.100	0.225	10	-	N_2H_4
250	26	0.100	0.250	10	-	N_2H_4
250	26	0.100	0.300	10	-	N_2H_4
250	26	0.100	0.300	10	-	-
250	26	0.100	0.300	-	-	$NaBH_4$
250	26	0.100	0.250	-	10	N_2H_4
250	74	0.100	0.250	-	10	N_2H_4
250	74	0.100	0.300	-	10	N_2H_4

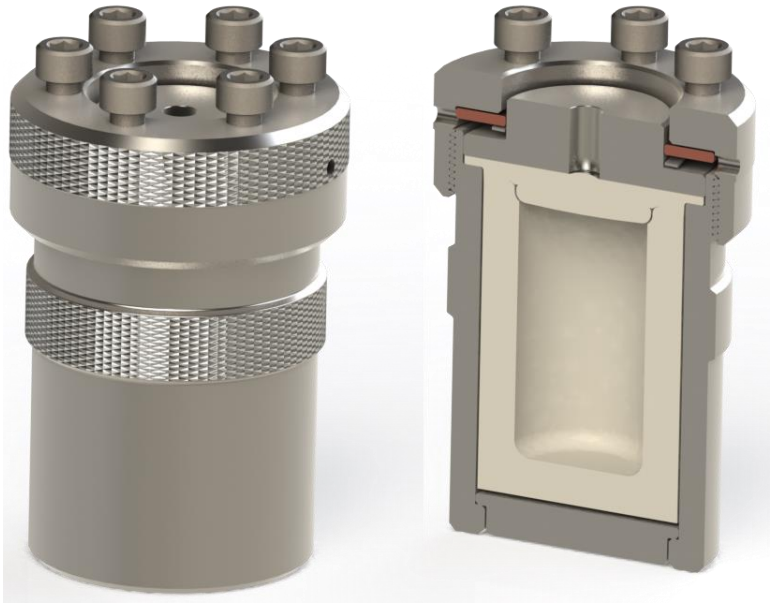

Fig. 31 Hydrothermal vessel with Teflon insert.

6.3. Results and discussion

6.3.1. Hydrothermal Syntheses

$EuTiO_3$

The difficulty of reduction of Eu^{+3} to its divalent state was shown in the previous chapter (processing of the bulk $EuTiO_3$ ceramics). The complexity of this issue was also proven during hydrothermal syntheses of ETO. No experiment resulted in synthesis of Eu^{+2} compound (of any kind), despite the distinctly higher electronegativity of both used reductant agents (N_2H_4 and $NaBH_4$) and their very high concentration in the precursor solutions. Even direct drop wise adding of concentrated $EuCl_3$ to N_2H_4 water solution (64%) led only to creation of N_2H_5Cl crystals. The similar result was observed even after HTS. The reasons could be the following:

- Reduction potential is lost or misplaced during the process.
- Temperature is insufficient for the reaction.
- Dwell time is short, the kinetics of the process is slower than expected.

The probability of the first mentioned explanation was already decreased by preparing of precursor solution under the inert atmosphere flow. On the other hand the risk can be further lowered by using non-aqueous solutions of precursors (e.g. ethylene glycol).

Initial HTS experiments were kept at the temperature of 220 °C. This temperature was increased to 250 °C in the later experiments without any significant change in

the phase composition. This is also the maximum temperature allowed by manufacturer of the hydrothermal reactor which was used in these experiments. The characteristics of the Teflon insert start to degrade (decrease of chemical resistance and mechanical strength) around the temperature of 260 °C and the material starts to decompose at 350 °C.

The majority of experiments were hold at the required temperature for 24 hours. A few of them were repeated with elongated dwell time (up to 3 days), but again without any significant change in the phase composition. From the energetic and time consuming point of view, the longer experiments would be very expensive with uncertain benefits for the reduction potential of upper mentioned additives.

Probably the best solution is to avoid the difficult reduction of Eu^{+3} completely and simply start with Eu^{+2} already from the beginning. It means that the Eu_2O_3 precursor would be replaced for example by EuO or directly by $EuCl_2$. The europium is in the "+2" oxidation state in the both of these compounds, but the reducing condition during syntheses are still necessary to prevent unwanted oxidation of product.

The most commercially available precursors contain europium in the oxidation state Eu^{+3}. The key step in fabrication of $EuTiO_3$ perovskite powder (where the europium is in the Eu^{+2} state) is the reduction of the Eu ions (Eq. 38). For that purpose the reduction agents took a part in these experiments.

Such solution is economically inconvenient because the prize of $EuCl_2$ is almost 3 times higher (ca 200 € / g) than $EuCl_3$ and EuO is not commercially available at all.

The alternative solution is the reduction of Eu_2O_3 powder precursor to EuO in laboratory condition in the pure hydrogen atmosphere. It is possible that original problem with insufficient reducing condition will occur also in this case, that is why the calculations of necessary condition (temperature, purity of the H_2 atmosphere) were performed using similar thermodynamic approach as in previous chapter - Van't Hoff isotherm (see Eq. 38 – 40).

$$\mathrm{Eu_2O_3}^{s} + {H_2}^{g} \leftrightarrow 2{\cdot}\mathrm{EuO}^{s} + {H_2O}^{g} \tag{38}$$

$$\Delta \mathrm{G}_T^0 = 2{\cdot}G_0(\mathrm{EuO}^{s}) + G_0({H_2O}^{g}) - G_0(\mathrm{Eu_2O_3}^{s}) - G_0({H_2}^{g}) \tag{39}$$

$$p(H_2O) = p(H_2){\cdot}exp\left(\frac{-\Delta G}{R{\cdot}T}\right) \tag{40}$$

The calculated equilibrium partial pressure of water vapours in dependence on the reaction temperature is given in Fig. 32 for 3 levels of partial pressure of hydrogen. The conditions below the curve allow occurring of the reduction reaction according to Eq. 38 and vice versa. Considering hydrogen furnace operating with flowing atmosphere, where the pressure slightly exceed the atmospheric one, then the blue curve should be taken on account.

The pressure hydrogen is commercially commonly available in purities 99.99 vol.% resp. 99.999 vol.% of H_2. This implies that partial pressure of H_2O vapour would be maximally 10 Pa resp. 1 Pa. It can be seen that for partial pressure of water vapours 10 Pa (i.e. H_2 purity 99.99 %) the minimal temperature needed for the reaction (Eq. 38) is ca 1870 K and for partial pressure of water vapours 1 Pa (i.e. H_2 purity 99.999 %) it is ca 1580 K. These temperatures are available in our hydrogen furnace, therefore the possibility of preparation of EuO powder will be tested in our next experiments. It should be noted, that such experiments should lead to particles growth and agglomeration.

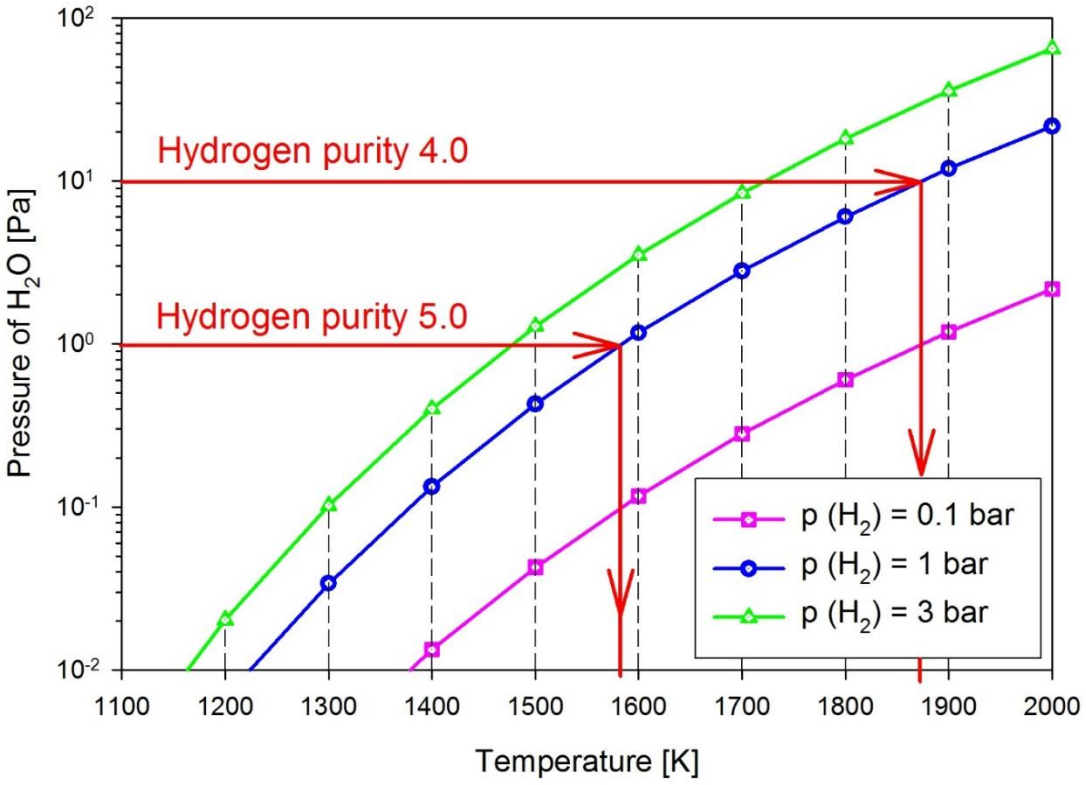

Fig. 32 The dependence of partial pressure of water vapours on the minimal temperature needed for the reaction (Eq. 38).

How it was written above, despite huge reduction potential of N_2H_4 and $NaBH_4$ (Eq. 34 and 36), reduction of europium from 3+ to 2+ state was unsuccessful. This is also the main reason, why other presumed phases such $Eu(OH)_3$ and $Eu_{0.5}Na_{0.5}TiO_3$ occurred.

$Eu_{0.5}Na_{0.5}TiO_3$

The perovskite phase $Eu_{0.5}Na_{0.5}TiO_3$ was present in every synthesis, were both precursors (Eu and Ti) were used. Its amount increased with Ti ions concentration (see Fig. 35), the maximum (single phase composition $Eu_{0.5}Na_{0.5}TiO_3$) was established for the concentration of Ti 0.25 $mol \cdot l^{-1}$. While lower concentrations lead to secondary $Eu(OH)_3$ phase appearance, the higher concentration (0.3 $mol \cdot l^{-1}$)

increase the content of amorphous phases. The source of the Na ions was the sodium hydroxide (NaOH), which was necessary for creation of the highly alkaline environment. The optimization of the Ti/Eu ratio resulted in the single phase $Eu_{0.5}Na_{0.5}TiO_3$ synthesis. Powder product was consisting of homogeneous cubic particles of ~ 1 μm in size (see Fig. 33 and Fig. 34) was synthetized.

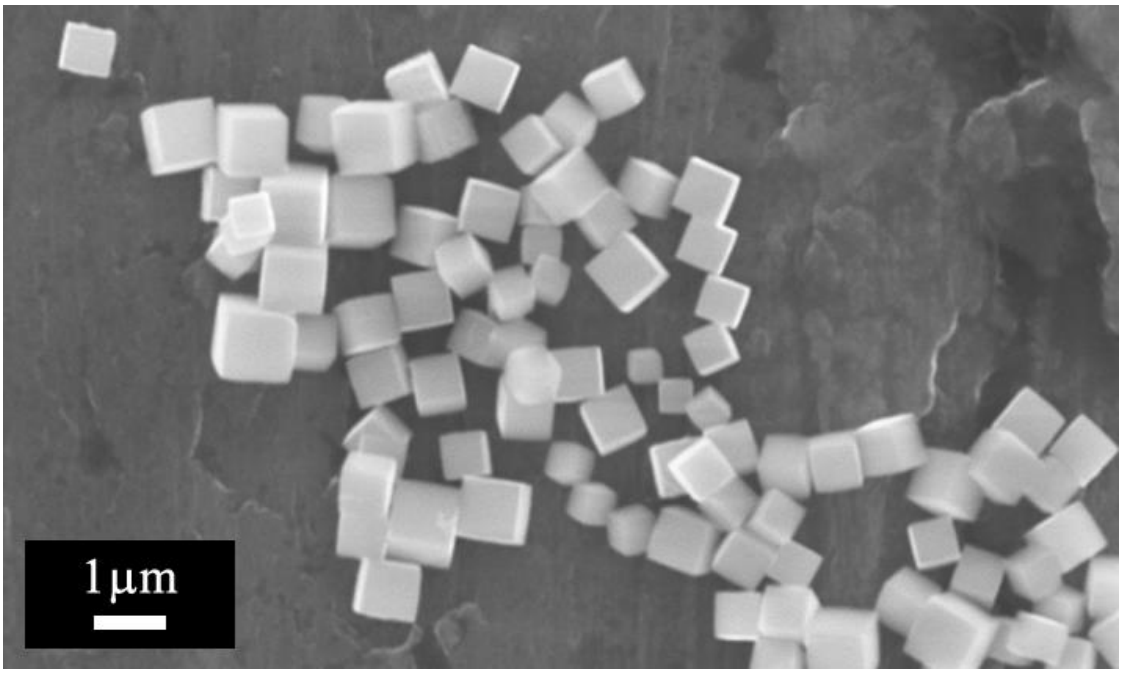

Fig. 33 Morphology of $Eu_{0.5}Na_{0.5}TiO_3$ powder synthetized by HTS.

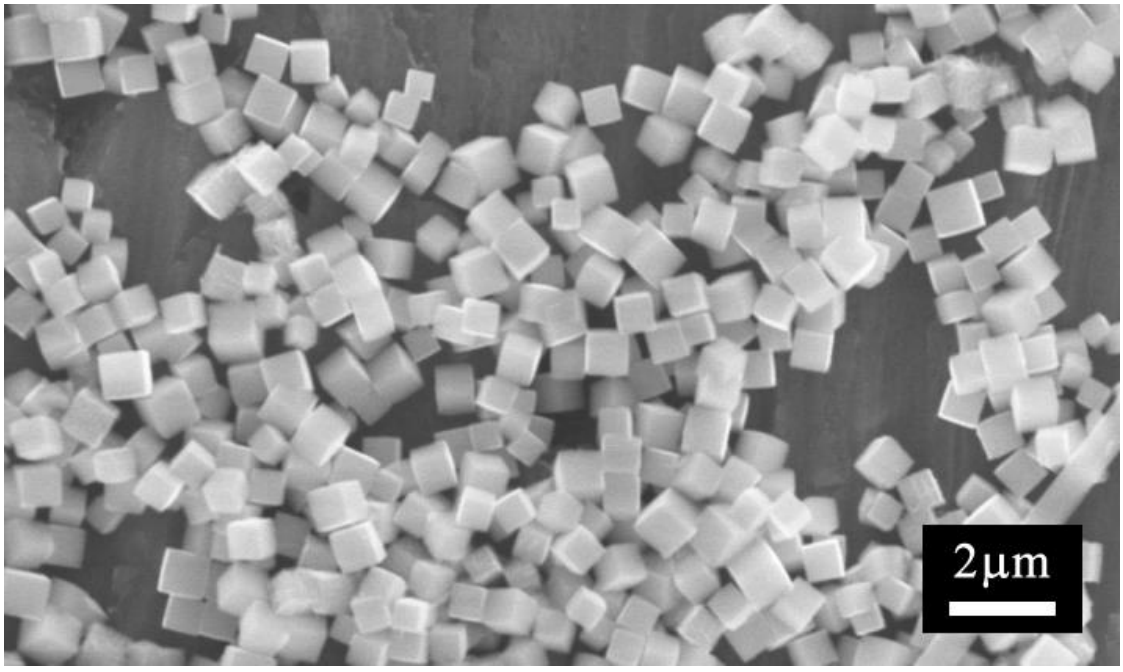

Fig. 34 Higher magnification of the morphology of $Eu_{0.5}Na_{0.5}TiO_3$ powder synthetized by HTS.

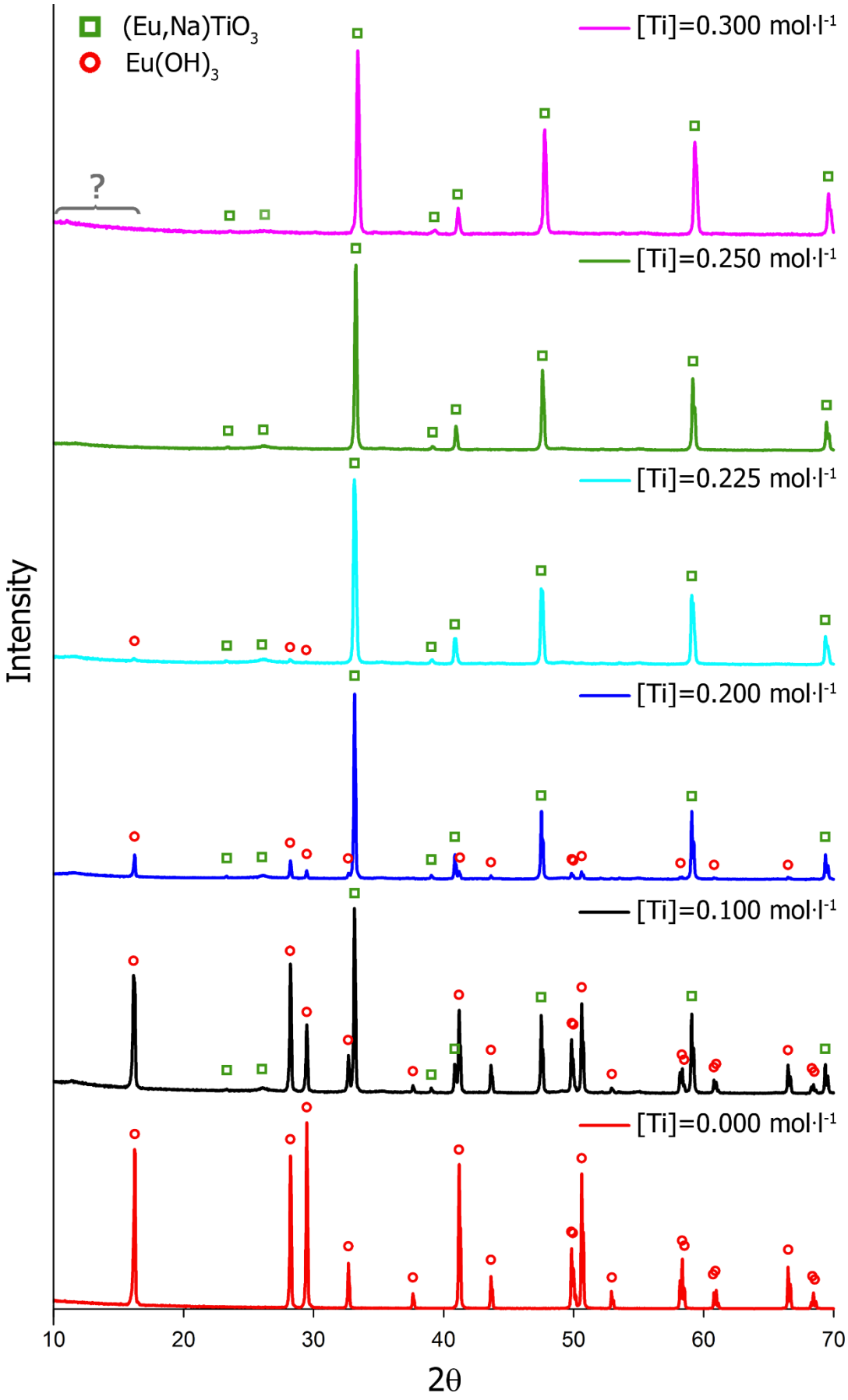

Fig. 35 Change in the phase composition of HT synthetized product with increasing concentration of Ti precursor.

6.3.2. Magnetic properties

The initial results of magnetic susceptibility evaluation of synthetized powder in dependence on temperature is given in Fig. 36. The sample did not dispose any magnetic ordering. Anyway, the material exhibits kind of magnetic susceptibility saturation under 100 K. This behaviour is in the conflict with the Currie-Weiss law (see Fig. 7), which is valid for every paramagnetic materials (paramagnetics doesn't have any spontaneous magnetic ordering).

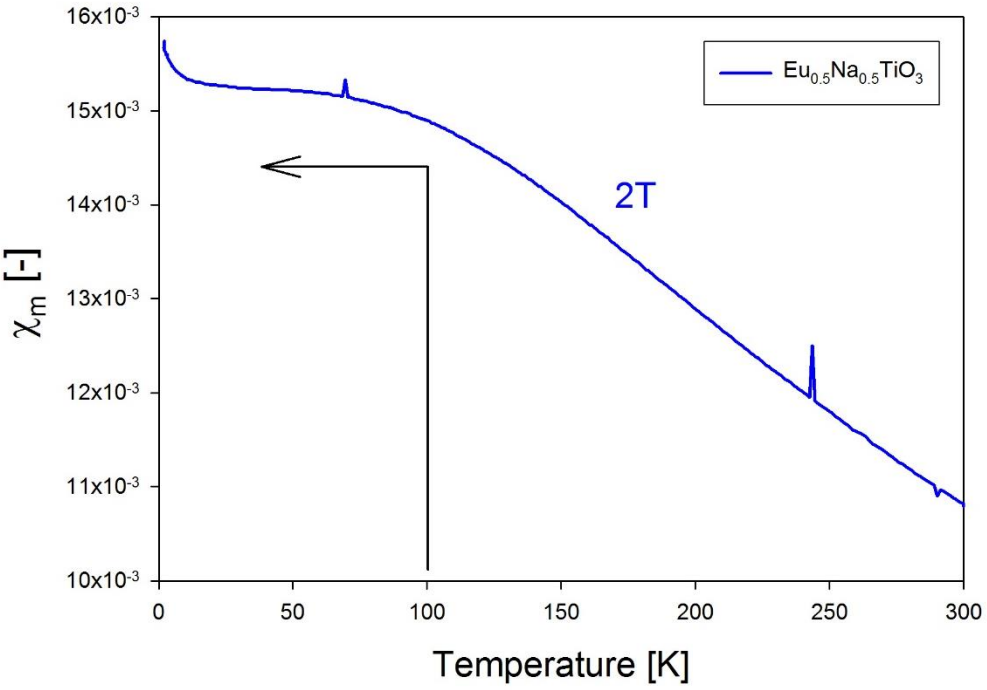

Fig. 36 Temperature dependence of magnetic susceptibility of $Eu_{0.5}Na_{0.5}TiO_3$ ceramic material in the external magnetic with intensity 2 T.

This behaviour would be maybe possible in case of some glass phases, but measured sample was highly crystalline (Fig. 35 – green diffractogram). Further investigation and deeper understanding of these result are necessary. In the case of confirmation of these data, it could be the first published material with sort of inception of ferromagnetism (quantum paramagnetics).

6.4. Summary

The difficulty of reduction of Eu^{+3} to its divalent state was shown in the previous chapter (processing of the bulk $EuTiO_3$ ceramics) and confirmed by results of HTS. Any HTS experiment did not result in synthesis of Eu^{+2} compound (of any kind), despite the distinctly higher electronegativity of both used reductant agents (N_2H_4 and $NaBH_4$) and their very high concentration in the precursor solutions.

On the other hand, another expected phase was successfully synthetized. Through optimization of Ti ions concentration a single phase $Eu_{0.5}Na_{0.5}TiO_3$ perovskite powder was

synthetized by HTS at 250 °C for 24 hours. The powder have particles in the shape of regular cubes with submicron size. The measuring of magnetic characteristic did not showed any type of magnetic ordering, but exhibits kind of magnetic susceptibility saturation under 100 K. Further investigation and deeper understanding of these result are necessary. In the case of confirmation of these data, it could be the first published material with sort of inception of ferromagnetism (quantum paramagnetics).

7. $MgTiO_3$

7.1. State of the art

In the fabrication of ceramic components, important achievement is often to reach full or almost full density of ceramics. In the last decades quite large number of sintering techniques besides conventional sintering method was developed. Consolidation of ceramic green bodies by these techniques (e.g. two-step, microwave and spark plasma sintering) are preferably used for materials, which processing is difficult from the point of view of reaching required microstructure, final density and phase purity [38, 69-71].

Magnesium titanate is a ceramic material widely used as resonators, filters and antennas for communication systems operating at microwave frequencies and capacitors [72, 73]. In the literature, various methods for $MgTiO_3$ fabrication were presented, such as solid-state reactions, co-precipitation or sol–gel route [72, 74, 75]. Few secondary phases were often detected along with $MgTiO_3$ phase ($MgTi_2O_5$, Mg_2TiO_4) [76, 77]. Preparation of pure $MgTiO_3$ by solid state reaction was the aim of many papers. However, magnesium titanate ceramics obtained by sintering process without additives reached density less than 95 %TD [78]. In order to improve properties of ceramics, it is desirable to achieve microstructures with nearly full density and fine grains with homogenous distribution.

Along with powder synthesis, consolidation and shaping of the ceramic green bodies, the optimization of the sintering process has been in the focus of attention during the last couple of decades. It is well know that density has very important role on dielectric properties of magnesium titanate, especially the dielectric constant [79].

The goal of this research part was to process high-dense and phase-pure $MgTiO_3$ using solid state synthesis and advanced sintering methods.

7.2. Experiments

7.2.1. Precursor materials

Magnesium(II) Oxide

This powder material was manufactured by Sigma-Aldrich and its purity is higher than 99 % (MgO - CAS: 1309-48-4). A particle size is specified by manufacturer as -325 mesh.

Titanium(IV) Oxide - anatase

This powder material was manufactured by Sigma-Aldrich and its purity is higher than 99.8 % (TiO_2 - CAS: 1317-70-0). The powder is in anatase modification.

7.2.2. Powder mixture processing

Stoichiometric calculations

The precursor powders MgO and TiO_2 were manually mixed in molar ratio 1:1 (according Eq. 41), weight ratio is calculated by Eq. 42 and 43. The mixture was

homogenized by high energy planetary ball mill (Fritsch Pulverisette) for the time interval of 0, 10, 40, 80 and 160 min creating 5 powder mixtures of different mechanical activation level. The milling balls to powder mass ratio was 40:1 and the process was performed in air atmosphere. Milling elements and bowls were from ZrO_2. The MgO powder was calcined at 700 °C for 2 h right before the milling process (to remove CO_2 and H_2O absorbed from air). The XRD analyses were performed to verify the phase composition after high energy milling process.

$$\mathrm{MgO} + TiO_2 \leftrightarrow \mathrm{MgTiO_3} \tag{41}$$

$$\mathrm{w}(MgO) = \frac{M(MgO) \cdot 100}{M(MgO) + M(TiO_2)} = \frac{40.304 \cdot 100}{40.304 + 79.878} = 33.536[wt\dot{0}\%] \tag{42}$$

$$\mathrm{w}(TiO_2) = \frac{M(TiO_2) \cdot 100}{M(MgO) + M(TiO_2)} = \frac{79.878 \cdot 100}{40.304 + 79.878} = 66.46\dot{4}[wt\%] \tag{43}$$

7.2.1. Green body shaping

The shaping of a green bodies was performed by isostatic pressure of 300 MPa for 5 min. The latex dies diameter was approximately 14 mm. The diameters of resulting cylindrical green bodies (after CIP) varied in the range of 10 – 12 mm. The porosity distribution of these ceramic precursors were established by mercury intrusion porosimetry.

7.2.2. Sintering

The green body samples were consolidated by conventional resp. two-step sintering regimes. In the case of conventional sintering, the samples were post-sintered by hot isostatic pressing (post-HIPed) to enhance the final densities of samples with minimal grain growth.

The conventional pressureless sintering was performed at 1300 °C resp. 1400 °C with the heating rate 10 °C·min^{-1}, dwell time 30 min and cooling rate 5 °C·min^{-1}. The sintering atmosphere was air (1 bar).

The post-sintering by HIP was performed at the temperature of 1200 °C for 2 hours resp. of 1280 °C for 3 hours (samples sintered at 1400 °C). The sintering atmosphere was in the both cases pure Ar and pressure 200 MPa.

Two-step sintering was performed at 1300 °C for 30 min (the first step) followed by 1200 °C for 20 hours (the second step). Other parameters of the sintering process were the same as in the case of conventional sintering.

The densities were established by measuring based on Archimedes principle (EN 623-2) using the theoretical value of density for $MgTiO_3$ ρ_{theor} = 4.00 g·cm^{-3} [80].

7.3. Results and discussion

The XRD analyses showed change in the phase composition during high energy milling process. With increasing milling time the precursors gradually recrystallized into $MgTiO_3$ phase. After 160 min of milling the mixture was consisted mostly by new $MgTiO_3$ phase (approx. 90 vol.%) together with minority phases Mg_2TiO_4, MgO and TiO_2 (see Fig. 37).

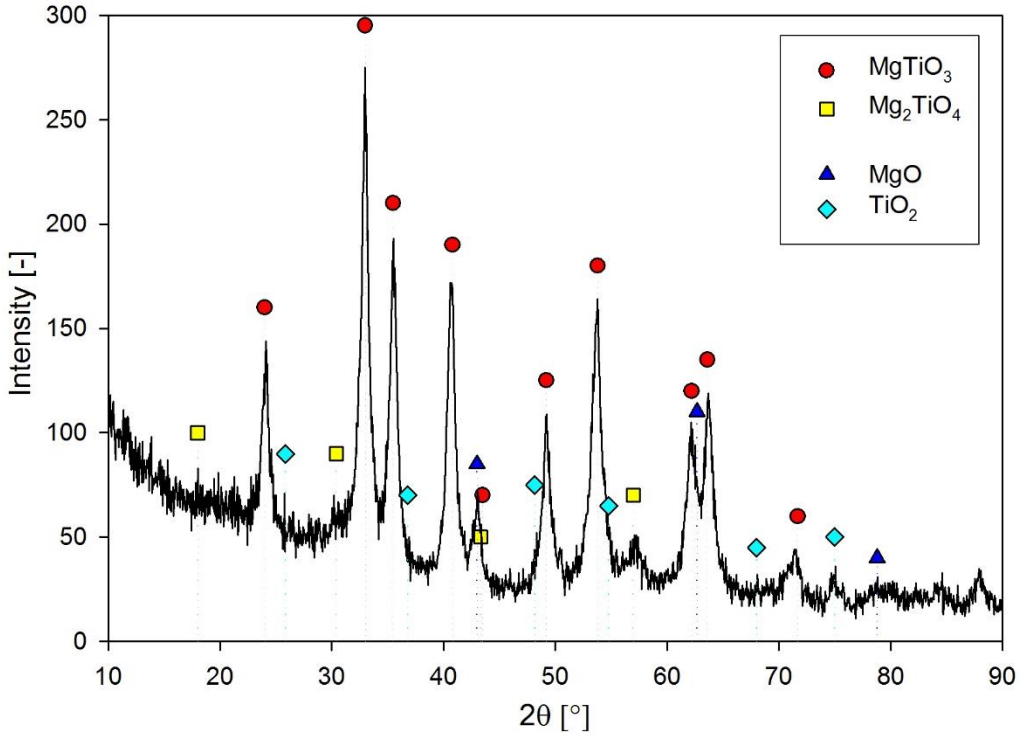

Fig. 37 XRD diffractogram of powder mixture milled for 160 min.

The green body sample from powder mixture without activation shows bimodal pore size distribution, what could be expected concerning two powder precursors of different particle size. The distribution was broadened during the mechanical activation by high energy milling up to 100 nm pore radius (80 min).

The first batch of samples was sintered by conventional sintering at 1300 °C in air. After sintering the sample from non-activated powder (activation 0 min) had white colour with yellow spots (indication of inhomogeneous chemical/phase composition), the other samples were light-brown. The highest relative density (88.9 %TD) reached the samples formed from mixture mechanically activated for 160 min. As expected, the sintering at higher temperature 1400 °C leaded to increase of relative density in the case of all samples. The sample activated for 160 min reached again the highest relative density 92.8 %TD. The relative and absolute densities of conventionally sintered samples are summarized in Table 10 and Table 11.

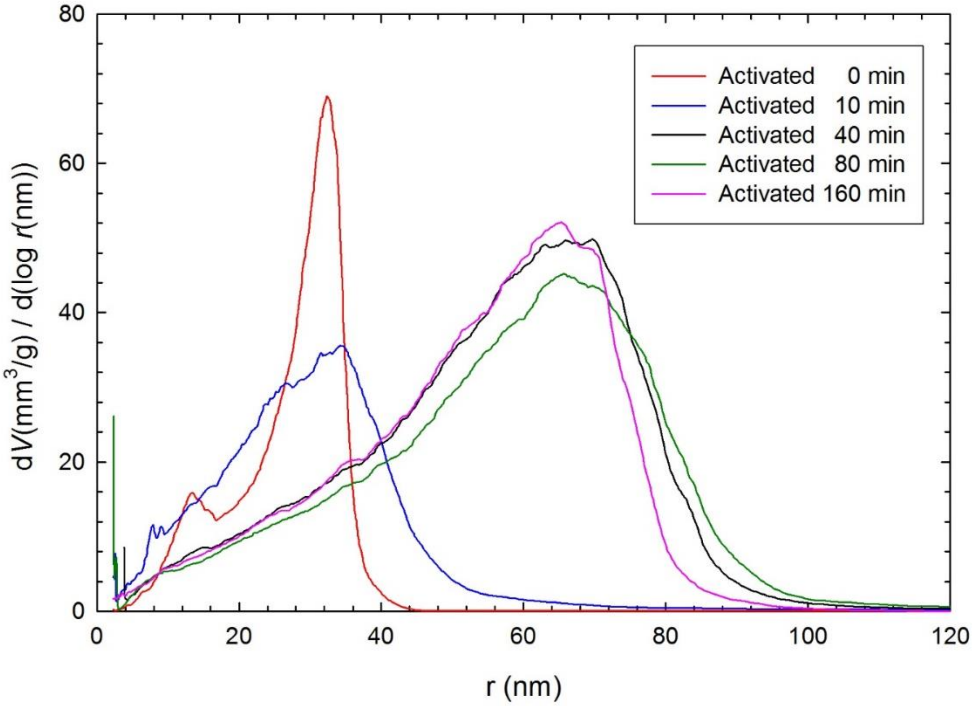

Fig. 38 Pore size distribution of green bodies formed by CIP of 300 MPa from powder mixtures activated for 0, 10, 40, 80 and 160 min.

Table 10 Conventional sintering of MTO samples at 1300 °C for 30 min in air.

Mechanical activation time [min]	Absolute density [g·cm^{-3}]	Relative density [%TD]	Rel. open porosity [vol.%]	Rel. closed porosity [vol.%]
0	3.00	74.9	21.9	3.2
10	3.53	88.2	7.2	4.7
40	3.50	87.5	8.2	4.3
80	3.53	88.3	6.6	5.1
160	3.56	88.9	5.1	6.1

Table 11 Conventional sintering of MTO samples at 1400 °C for 30 min in air.

Mechanical activation time [min]	Absolute density [g·cm^{-3}]	Relative density [%TD]	Rel. open porosity [vol.%]	Rel. closed porosity [vol.%]
0	3.01	75.3	20.3	4.7
10	3.69	92.1	0.3	7.4
40	3.67	91.8	0.3	7.9
80	3.69	92.3	0.2	7.5
160	3.71	92.8	0.2	7.0

The increase of relative densities of samples sintered at 1400 °C in comparison with samples sintered at 1300 °C is significant, but more important is the change of open porosity content. It is very important to minimize the open porosity content before post-sintering the samples by HIP. That is why only the samples sintered at 1400 °C were used for the next step. Samples were cut into two pieces and post-sintered at 1200 °C for 2 h resp. at 1280 °C for 3 h. Both experiments were performed in Ar atmosphere of pressure 200 MPa (HIP). The resulting densities are summarized by Table 12, the increase of absolute densities is shown in the Fig. 39.

Table 12 The densities of samples sintered at 1400 °C and post-sintered by HIP.

Mechanical activation time [min]	**HIP 1200 °C / 2 h**		**HIP 1280 °C / 3 h**	
	Absolute density [g·cm^{-3}]	Relative density [%TD]	Absolute density [g·cm^{-3}]	Relative density [%TD]
0	-	-	-	-
10	3.72	92.9	3.75	93.7
40	3.70	92.5	3.74	93.4
80	3.73	93.3	3.75	93.9
160	3.81	95.2	3.86	96.5

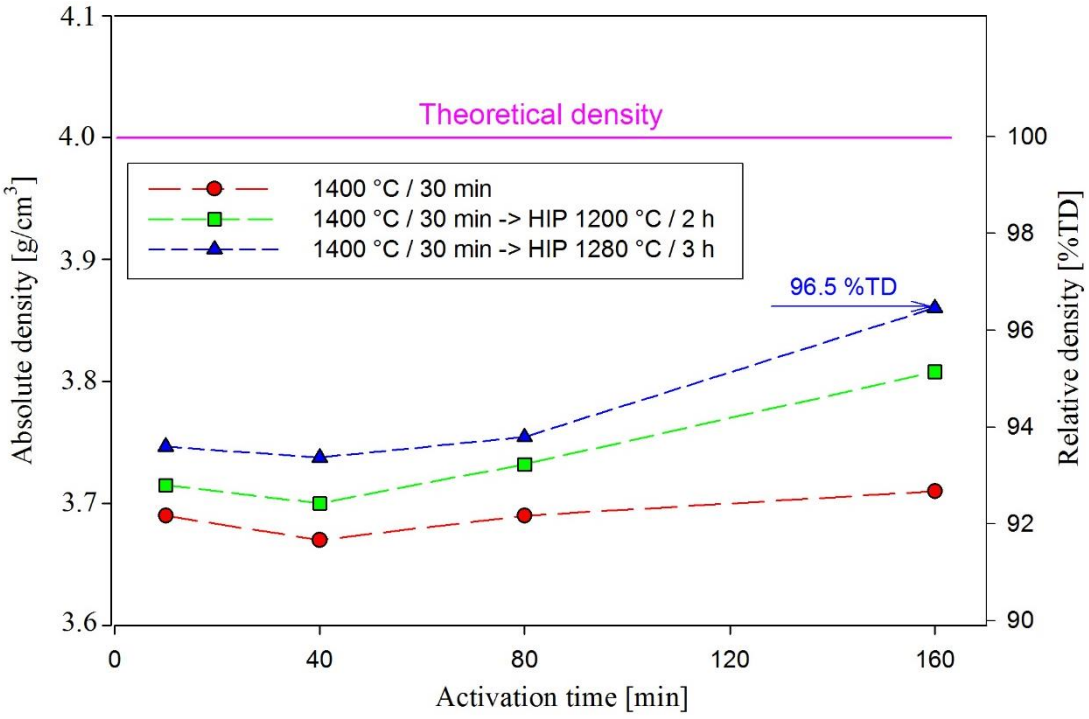

Fig. 39 Influence of the pressure assisted post-sintering by HIP at 1200 °C (2 h) resp. 1280°C (3 h).

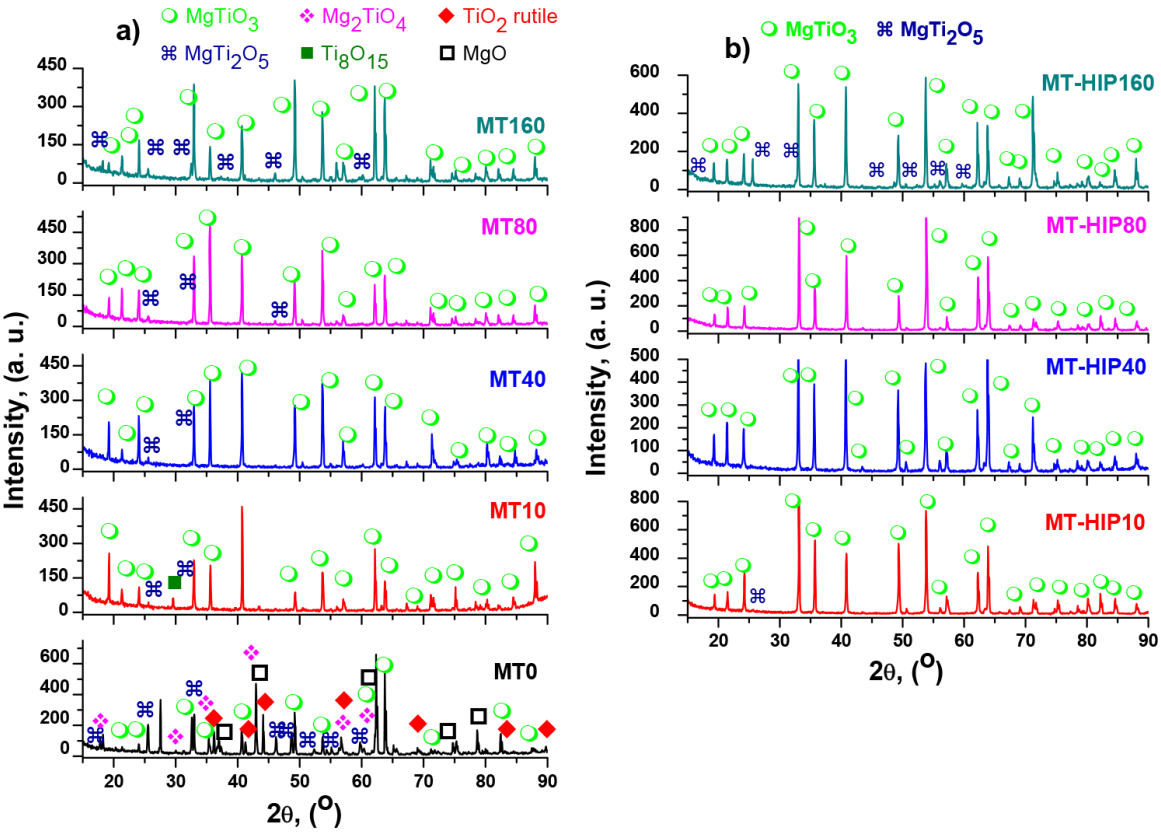

Fig. 40 The XRD patterns of samples: a) single sintered (1400 °C / 30 min), b) post-sintered (1400 °C / 30 min and HIP 1280 °C / 3 h / Ar / 200 MPa) [81].

The XRD diffraction patterns of sintered and post-sintered samples are shown in Fig. 40. The sharp diffraction peaks indicate that recrystallization process occurred during the high temperature treatment. In the case of samples sintered by conventional method at 1400 °C, a few different phases can be identified in the patterns. In non-activated sample the presence of $MgTiO_3$, Mg_2TiO_4, $MgTi_2O_5$, TiO_2 (rutile), MgO and Ti_8O_{16} can be observed. That indicates unfinished chemical reaction probably due to insufficient homogenization of powder mixture. The activated sample phase compositions are mixture of $MgTiO_3$ as the dominant phase with presence of $MgTi_2O_5$ as a minor phase.

The diffraction patterns of samples post-sintered by HIP the $MgTiO_3$ as a dominant phase is detected along with small amount of residual phases $MgTi_2O_5$. The X-ray analyses samples activated for 40 and 80 min indicated the presence of single $MgTiO_3$ phase, which was one of the main goals of this investigation.

The additional densification approach - Two-step sintering was performed at 1300 °C for 30 min (the first step) followed by 1200 °C for 20 hours (the second step). The increase of relative densities is observed in the comparison with conventionally sintered samples at 1300 °C. The highest relative density is 89.5 %TD, this value is exhibited by the sample activated for 160 min. These mixture showed the highest values of density (the best sintering characteristic) for every sintering regimes and techniques. Anyway, the two-step

sintering regime did not lead to significant improvement of final density as expected. The densities of sintered samples as well as the open and closed porosity content are summarized in Table 13.

Table 13 Two-step sintering of MTO samples at 1300 °C (30 min) followed by 1200 °C (20h) in air.

Mechanical activation time [min]	Absolute density [g·cm^{-3}]	Relative density [%TD]	Rel. open porosity [vol.%]	Rel. closed porosity [vol.%]
0	3.02	75.6	20.7	3.7
10	3.56	88.9	5.9	5.2
40	3.53	88.2	6.7	5.1
80	3.56	89.0	5.2	5.8
160	3.58	89.5	4.2	6.3

7.4. Summary

The mixtures of powder precursors MgO and TiO_2 (anatase) were mechanically activated by high energy ball milling for 0, 10, 40, 80 and 160 min. Green bodies were formed by CIP of 300 MPa for 5 min. The sintering was performed by two different approaches. The first one was conventional sintering followed by hot isostatic pressing and the second was two-step sintering. The highest relative densities were reached by the first approach (HIP). The final densities were increasing with time of mechanical activation, when the sample prepared from the mixture activated for 160 min reached relative density higher 96 %TD, but in the phase composition a small amount of secondary $MgTi_2O_5$ phase was detected. On the other hand, the samples prepared from mixtures activated 40 and 80 min (post-sintered by HIP 1280 °C / 3h) exhibited single $MgTiO_3$ phase. Main part of these results was already published at the Science of Sintering Journal [81].

8. Ba(Ca)Ti(Zr)O_3

8.1. State of the art

The basic approach to high piezoelectric characteristics achieving is to design the material composition close to the phase transition between two ferroelectric phases. This transition is known as "the morphotropic phase boundary" (MPB). Instabilities of the polarization state (generated close to this transition) cause high piezoelectricity and also high permittivity. The highest piezoelectric characteristics are desirable close to room temperature for most of applications. In the last decades ceramic materials based on $PbTi(Zr)O_3$ (PZT) were used for their strong piezoelectric characteristic. The problem is that lead is environmentally unfriendly (poisonous to humans and animals, damaging the nervous system and causing brain disorders). PZT ceramics is chemically inert and does not constitutes any health risk, but lead is partially evaporated during sintering process. That's the main reason why new lead-free piezoelectric materials are highly welcomed.

One of the promising materials from the group of lead free piezoelectric is $Ba(Ca)Ti(Zr)O_3$. The most often studied solid solution of this perovskite material is the composition $Ba_{0.85}Ca_{0.15}Ti_{0.9}Zr_{0.1}O_3$ (50/50 composition in the pseudobinary notation $BaZr_{0.2}Ti_{0.8}O_3$ - $Ba_{0.7}Ca_{0.3}TiO_3$) [82, 83]. Fig. 41 shows position of the MPB depending on temperature and composition. Bulk ceramic with this composition exhibits ε_r = 3060 and d_{33} = 560–620 pC/N [84]. These values are comparable with PZT piezoceramics (unlike other current lead-free piezoceramics materials).

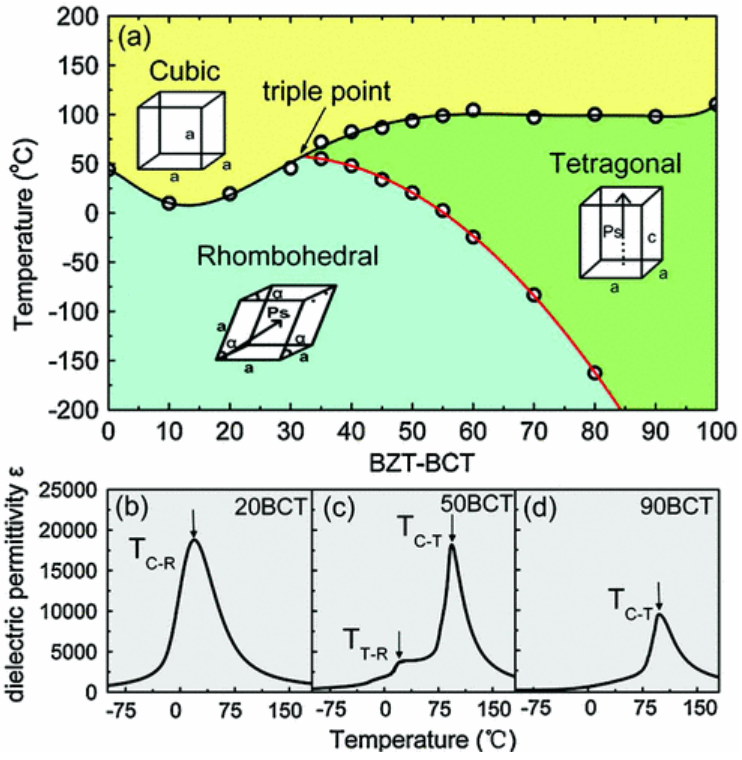

Fig. 41 Phase diagram of $BaZr_{0.2}Ti_{0.8}O_3$ - $Ba_{0.7}Ca_{0.3}TiO_3$ system and dielectric permittivity of chosen compositions [84].

Additionally, processing route has a significant influence on the formation of crystallographic phases [84, 85], and thus the precise location of MPB in this system is one of the future research challenges. The need of further investigation of processing route influences becomes even more essential in the case of more complex solid solutions - e.g. Ba(Ca)Ti(Zr)O_3 with $Bi_{0.51}(K_{0.18}Na_{0.82})_{0.5}TiO_3$ addition [83].

The most usual processing route of Ba(Ca)Ti(Zr)O_3 ceramic is the solid state reaction of oxide and carbonate precursors ($BaCO_3$, $CaCO_3$, TiO_2 and ZrO_2). Whereas Krishnamoorthy et al. [86] let the precursors reacted separately at 1200°C for 12 h reaching $BaTiO_3$ and $CaZrO_3$ powders, other authors prepared desired stoichiometric mixture by ball milling directly [82, 87]. The influence of annealing temperature on the final density of bulk ceramics was studied Wang et al. [82], when after calcination at 1000°C, 1100°C, 1200°C resp. 1300°C for 2 h in air, samples did not reach single perovskite phase, but the amount of secondary phases was decreasing with temperature. Simultaneously the significant enhancement of final density with increasing calcination temperature was observed. The influence of particle agglomeration during annealing was mitigated by following ball milling for 5 h in ethanol. The dried powders were mixed with 6 wt. % polyvinyl alcohol (PVA) and pressed into the disks (∅15mm) by uniaxial pressing at 150MPa. After debinding (800°C for 1 h), the samples were sintered at 1500-1550°C for 2 h in air. The single perovskite phase was observed for all samples sintered at temperatures 1520°C and higher. However, other authors declare single perovskite formation even for lower sintering temperatures [86, 88, 89]. The samples reached the highest final densities at the temperature 1520°C [82]. With increasing sintering temperature densities decreased up to 1550°C, when the final densities again slightly increased. Nevertheless, the influence of calcination temperature on the final densities was much higher than the influence of the sintering temperature. Authors explain this phenomenon by narrower grain boundaries which allow easier short distance diffusion [82].

Piezoelectric properties were also influenced by calcination temperature. For example d_{33} coefficient increased proportionally with increasing calcination temperature (as well as with sintering temperature). The effect of the calcination temperature on the rate of d_{33} coefficient increase became even stronger for samples sintered at higher temperatures. This result indicates that the grain boundaries (which seem to be controlled by annealing temperature) could greatly affect the piezoelectric properties [82].

The sensitivity of piezoelectric properties on the processing route was also reported by Wang et al. [90]. The accurate measurements of phase compositions of Ba(Ca)Ti(Zr)O_3 ceramics near the MPB showed that the high piezoelectric response is closely related to the existence of monoclinic phase in the ceramic microstructure, but its occurrence is strongly dependent on stress. This result highlights the importance of proper choice of green body processing technique and sintering regime.

The main aim of following experiments was processing of single phase perovskite bulk $Ba_{0.85}Ca_{0.15}Ti_{0.9}Zr_{0.1}O_3$ ceramics with relative density higher than 90 %TD. Such a material would be suitable for establishing its real (undistorted) piezoelectric properties.

8.2. Experiments

8.2.1. Precursor materials

$BaCO_3$

This powder purity was 99.99 % and the specific surface area was established by nitrogen adsorption S_{BET} = 1.6 $m^2 \cdot g^{-1}$. The SEM observation confirmed agglomerated powder with unregularly shaped primary particles of about 2 μm large and 600 nm wide, the morphology is shown in A-Fig. 12. The particle (agglomerate) size was established by laser diffraction (A-Fig. 13). The primary particles are agglomerated into larger blocks up to 10 μm (unimodal distribution). The XRD analysis (A-Fig. 14) shows single orthorhombic phase $BaCO_3$.

$CaCO_3$

This powder purity was 99.99 % and the specific surface area was established by nitrogen adsorption S_{BET} = 0.13 $m^2 \cdot g^{-1}$. From this value the approximate diameters of ball shaped particle was calculated D_{BET} = 17 μm. The SEM observation confirmed that the powder is consisted of particles of about 20 μm large, the morphology is shown in A-Fig. 15. The particle (agglomerate) size was established by laser diffraction (A-Fig. 16). The primary particles are agglomerated into larger blocks up to 100 μm (unimodal distribution). The XRD analysis (A-Fig. 17) shows single rhombohedral phase $CaCO_3$.

TiO_2

This powder purity was 99.99 % and the specific surface area was established by nitrogen adsorption S_{BET} = 8.4 $m^2 \cdot g^{-1}$. From this value the approximate diameters of ball shaped particle was calculated D_{BET} = 180 nm. The SEM observation confirmed that the powder is consisted of particles of about 150 nm large, the morphology is shown in A-Fig. 18. The particle (agglomerate) size was established by laser diffraction (A-Fig. 19). The primary particles are agglomerated into larger blocks up to 2 μm (bimodal distribution). The XRD analysis (A-Fig. 20) shows two phases of TiO_2 (98 % of anatase and 2 % of rutile).

ZrO_2

This powder purity was 99.9 % and the specific surface area was established by nitrogen adsorption S_{BET} = 9.2 $m^2 \cdot g^{-1}$. From this value the approximate diameters of ball shaped particle was calculated D_{BET} = 110 nm. The SEM observation confirmed that the powder is consisted of particles of about 100 nm large, the morphology is shown in A-Fig. 21. The particle (agglomerate) size was established by laser diffraction (A-Fig. 22). The primary particles are agglomerated into larger blocks up to 10 μm (bimodal distribution). The XRD analysis (A-Fig. 23) shows single ZrO_2 phase with monoclinic lattice.

8.2.2. Powder mixture processing

The mixture for solid state reaction leading to $Ba_{0.85}Ca_{0.15}Ti_{0.9}Zr_{0.1}O_3$ perovskite ceramic were weighed using laboratory scales (precision 0.001 g). All calculations were done according Eq. 44 for 20 g of mixture. Resulting ratios and weights are summarized in Table 14.

$$17BaCO_3 + 3CaCO_3 + 18TiO_2 + 2ZrO_2 = 20\mathrm{Ba}_{0.85}Ca_{0.15}Ti_{0.9}Zr_{0.1}O_3 + 20CO_2 \quad (44)$$

Table 14 Calculated ratios and weights for the mixture according Eq. 44.

Powder	Molar weight [g/mol]	Relative weight [%]	Weight for 20g batch [g]
$BaCO_3$	197.336	62.834	12.567
$CaCO_3$	100.086	5.624	1.125
TiO_2	79.865	26.926	5.385
ZrO_2	123.222	4.616	0.923
$Ba_{0.85}Ca_{0.15}Ti_{0.9}Zr_{0.1}O_3$	222.940	-	-

Stoichiometric mixtures were homogenised by planetary ball mill using ZrO_2 elements (∅ 5mm) and polyamide (PA) respective zirconia milling bowls for 2, 4, 6 resp. 8 hours in ethanol. Particle size distribution of these 8 mixtures (2 different milling bowls and 4 different milling times) were measured by LD.

8.2.3. Green body shaping

Ceramic pellets (diameter ≈ 18mm; thickness ≈ 5mm) were formed by cold isostatic pressing (CIP) at 300 MPa for 5 min in latex moulds. Symmetry of green bodies was improved by hand grinding with sand paper. Resulting disc shaped ceramic bodies (diameter ≈ 16 mm; thickness ≈ 4 mm) were cut into quarters by scroll saw.

8.2.4. Sintering

For the solid-state reaction and consolidation of green bodies was used pressureless sintering at the temperatures 1200, 1300, 1400 resp. 1500 °C with dwell time 1 hour (heating rate 5°C/min; cooling rate 20°C/min) in air.

Densities of resulting ceramics were measured by Archimedes method (EN623-2). For calculations of relative densities the theoretical density (TD) of $Ba_{0.85}Ca_{0.15}Ti_{0.9}Zr_{0.1}O_3$ phase as in work of Wang P, et al. [82] was used (ρ_{theor} = 5.687 g·cm^{-3}).

8.3. Results and discussion

Whereas the particle size distribution in the mixture 1-4 is practically unchanged after first 2 hours of milling in ZrO_2 bowls (from the particle size point of view), different results are observed in the case of mixtures milled in the polyamide bowls. The particle size distribution is shifted to the lower values for the first 6 hour of milling, but longer time cause probable agglomeration of the final powder product. The results of milling (homogenization) step in the planetary mill are summarized in Table 15 and Fig. 42.

Table 15 Results of particle size distribution measuring (LD) of milled mixtures.

Sample	Milling bowl material	Milling time [h]	Median size [μm]	Diameter on cumulative 10 % [μm]	Diameter on cumulative 90 % [μm]
MIX 1	ZrO_2	2	0.72989	0.4862	1.0635
MIX 2		4	0.75922	0.4839	1.1390
MIX 3		6	0.74763	0.4807	1.1140
MIX 4		8	0.72185	0.4213	1.1319
MIX 5	PA	2	0.81255	0.3775	1.7910
MIX 6		4	0.70459	0.4330	1.1289
MIX 7		6	0.68500	0.3824	1.1342
MIX 8		8	1.17326	0.6096	2.4900

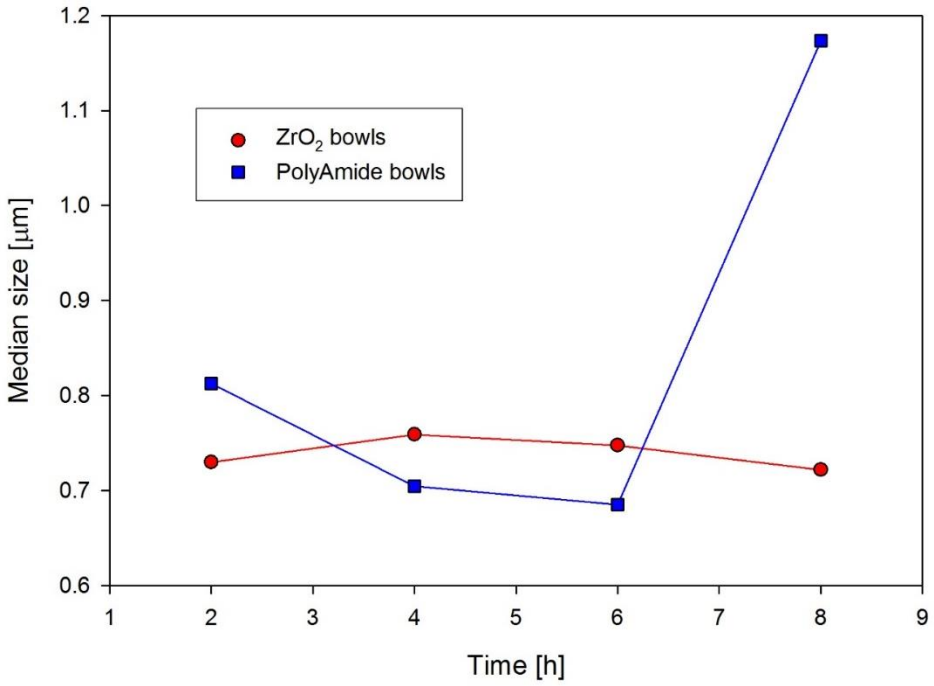

Fig. 42 Effect of milling time and bowl material on the particle median size.

Almost in all cases the relative density of samples raises with sintering temperature. The ceramic bodies sintered at 1200 °C have very small relative density because the density calculation neglected phase composition and the same theoretical density as for single phase $Ba_{0.85}Ca_{0.15}Ti_{0.9}Zr_{0.1}O_3$ ceramics. The samples milled in ZrO_2 bowls had almost the same particle size distribution, but the relative densities are slightly increasing with the milling time. In the case of samples milled in PA bowls the relative densities raises with milling time as well, with the optimal milling time 6 hours as was expected from particle size distribution after milling. On the other hand the influence of agglomeration of MIX 8 on final relative densities of sintered bodies was not so strong, when the values were slightly lower in comparison with MIX 7 (PA – 6 hour). All measured values of relative densities are summarized in Table 16 and graphically presented in the Fig. 43 and Fig. 44.

The highest relative density reached the sample milled 6 hour in PA bowl and sintered at 1500 °C for 1 hour. The phase composition of this sample was established by XRD and it is shown in Fig. 45. The sample have single perovskite phase, but because the XRD database does not content this phase (solid solution of composition $Ba_{0.85}Ca_{0.15}Ti_{0.9}Zr_{0.1}O_3$), the XRD diffractogram shown in Fig. 45 is fitted by similar $BaTiO_3$ phase.

Table 16 Relative densities of sintered samples milled in ZrO_2 (MIX 1-4) and PA (MIX 5-8) milling bowls.

Sample	Milling bowl material	Milling time [h]	Relative density [%TD]			
			1200 °C	1300 °C	1400 °C	1500 °C
MIX 1	ZrO_2	2	46.7	82.1	79.9	85.6
MIX 2		4	51.4	88.9	86.4	88.8
MIX 3		6	39.7	65.3	74.5	94.9
MIX 4		8	51.6	92.6	92.8	94.2
MIX 5	PA	2	38.0	60.7	78.6	88.3
MIX 6		4	42.5	69.4	81.9	95.1
MIX 7		6	43.4	68.8	88.8	96.0
MIX 8		8	41.3	67.5	83.3	94.5

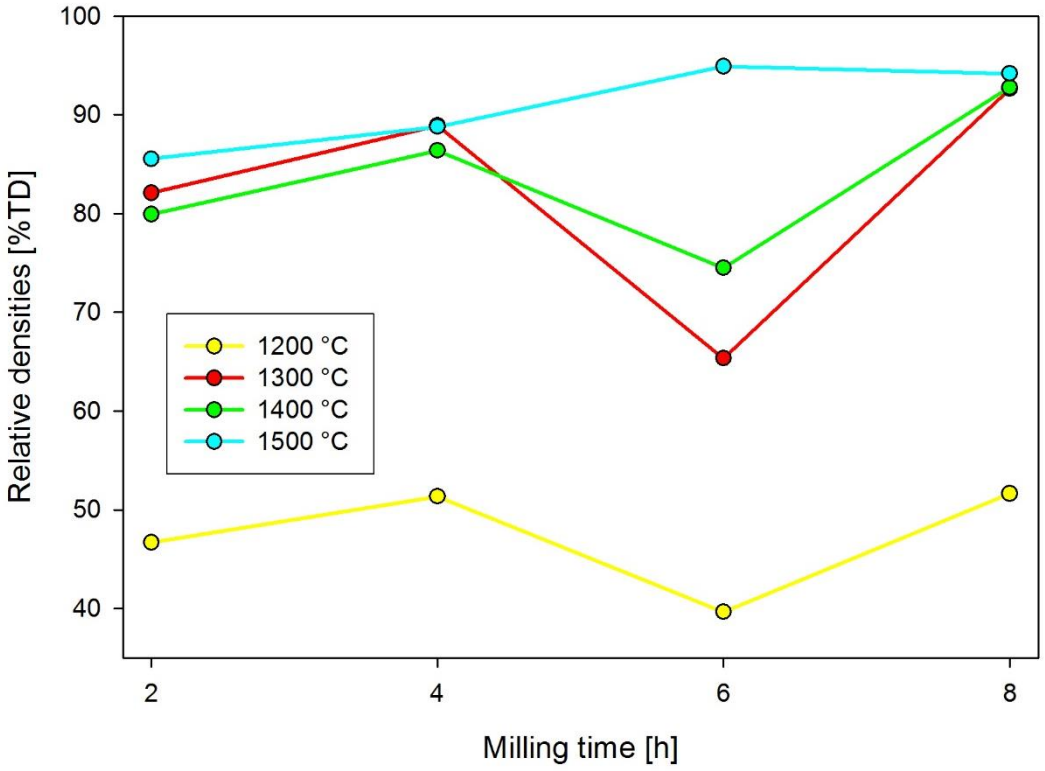

Fig. 43 Relative densities of sintered samples milled in ZrO_2 milling bowls.

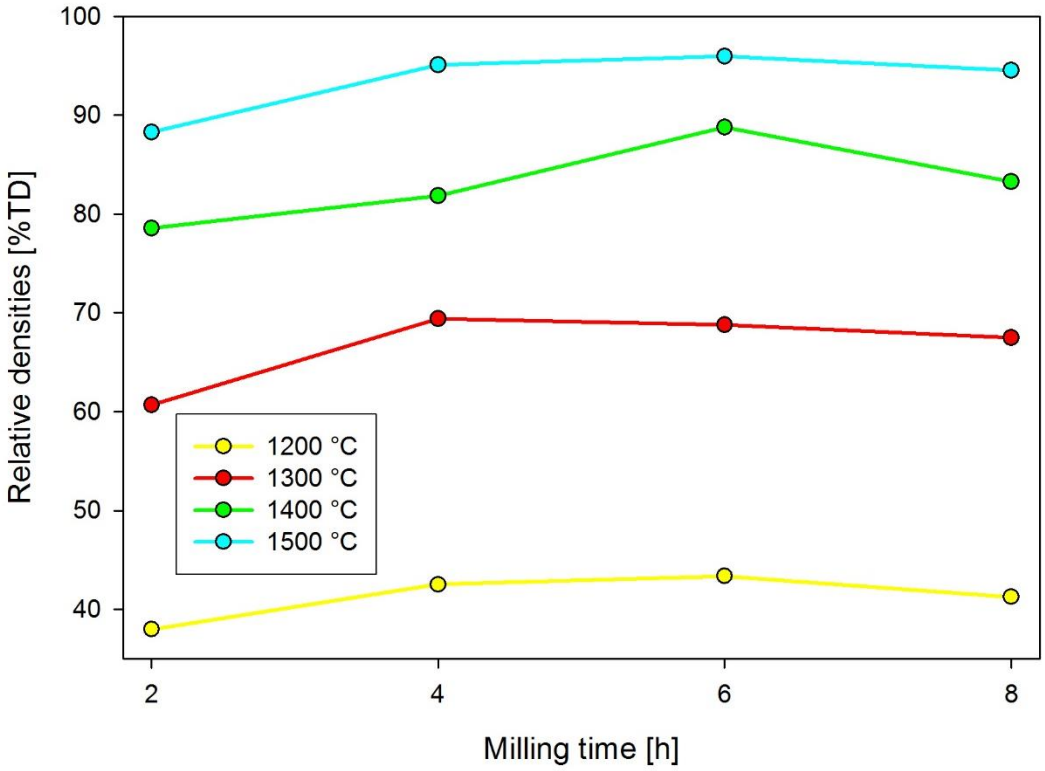

Fig. 44 Relative densities of sintered samples milled in PA milling bowls.

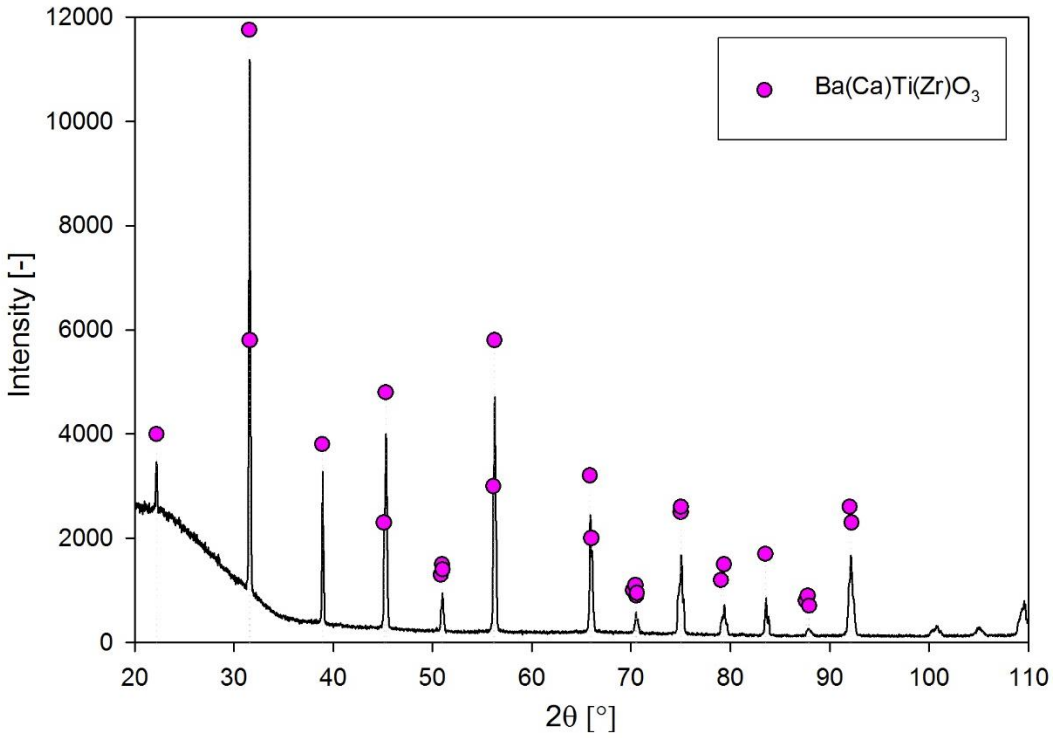

Fig. 45 XRD diffractogram of the single phase Ba(Ca)Ti(Zr)O_3 perovskite ceramics (MIX 7 – 1500 °C).

8.4. Summary

The single phase perovskite $Ba_{0.85}Ca_{0.15}Ti_{0.9}Zr_{0.1}O_3$ was synthetized by solid-state reaction from oxide and carbonate precursors ($BaCO_3$, $CaCO_3$, TiO_2 and ZrO_2). The planetary ball milling in zirconia resp. polyamide bowls were used for homogenization of precursor mixtures (MIX 1-8) for 2 – 8 hours. The highest relative density 96 %TD was reached by the sample, which was milled for 6 hour in PA bowl, formed by isostatic pressure of 300 MPa and sintered at 1500 °C for 1 hour in air. Such a ceramic material is suitable for further investigation of its piezoelectric characteristic.

9. Conclusion

In this thesis the processing of electroceramic materials for advanced applications and/or basic research was shown. In the case of all studied materials, the single phase samples with high relative density were prepared despite the lower sinterability of titanates with perovskite structure (in comparison with other advanced ceramic materials such as Al_2O_3, ZrO_2, etc.). Presented results demonstrated the importance of careful choice of the processing techniques and their variables for reaching of desired microstructure and phase composition of advanced electroceramics and therefore for proper evaluation of their physical properties.

Significant part of presented results were obtained during authors internships at collaborated international institution. The major part of the presented results are already published in impacted journals (see the summary of student's activities) what declare their novelty.

Summary of student's activities:

Publications

- M. Kachlik, K. Maca, V. Goian and S. Kamba; Processing of phase pure and dense bulk $EuTiO_3$ ceramics and their infrared reflectivity spectra, *Materials Letters*. 74 (2012), 16–18, DOI: 10.1016/j.matlet.2012.01.055
- K. Maca, M. Kachlik, P. Vaněk, D. Gautam and M. Winterer; The influence of sintering conditions on the phase purity of bulk $EuTiO_3$ and $Eu_{0.5}Ba_{0.5}TiO_3$ ceramics; *Phase Transition*. (2012), 1-11, DOI: 10.1080/01411594.2012.722633
- V. Goian, S. Kamba, O. Pacherová, J. Drahokoupil, L. Palatinus, M. Dušek, J. Rohlíček, F. Laufek, W. Schranz, A. Fuith, M. Kachlik, K. Maca, A. Shkabko, L. Sagarna, A. Weidenka and A. A. Belik; Antiferrodistortive phase transition in $EuTiO_3$; *Physical Review B*. 86 (2012), Issue 5, DOI: 10.1103/PhysRevB.86.054112
- D. Bessas, K. Z. Rushchanskii, M. Kachlik, S. Disch, O. Gourdon, K. Maca, I. Sergueev, S. Kamba, M. Ležai´c, and R. P. Hermann; Lattice instabilities in bulk $EuTiO_3$, *Physical Review B*. 88 (2013), Issue 14, DOI: 10.1103/PhysRevB.88.144308
- S. Filipovic, N. Obradovic,V. B. Pavlovic, D. Kosanovic, M. Mitric, N. Mitrovic, V. Pouchly, M. Kachlik and K. Maca; Advantages of Combined Sintering Compared to Conventional Sintering of Mechanically Activated Magnesium Titanate; Science of Sintering. (2014), Isssue 3, 283-290, DOI: 10.2298/SOS1403283F

Conferences and internships

- 1.11.2010 - 17.12.2010 Internship at the University of Duisburg-Essen (DE)
- 20.3.2011 - 24.3.2011 First ESR Workshop COST MP0904 (BE)
- 13.4.2011 - 17.4.2011 Internship at the National Centre of Scientific Research Demokritos (GR)
- 15.11.2011 - 19.11.2011 Second ESR Workshop COST MP0904 (SRB)
- 27.11.2011 - 3.12.2011 Internship at the University of Duisburg-Essen (DE)
- 28.2.2012 Workshop at IFP AVCR Inst. of Plasma Phys. (CZ)
- 5.3.2012 - 1.4.2012 Internship at the University of Duisburg-Essen (DE)
- 27.1.2013 - 30.1.2013 Training School in Ljubljana COST MP0904 (SLO)
- 19.7.2013 - 21.7.2013 Workshop COST MP0904 (CZ)
- 1.9.2013 - 30.11.2013 Internship at the IENI-CNR Genoa (IT)
- 30.1.2014 - 2.2.2014 Closing COST MP0904 SIMUFER Conference (IT)
- 22.6.2015 - 26.6.2015 Nanotechnology and Advanced Materials Workshop and Summer School (CZ)

Participation in research projects

- GACR P107-15-06390S "Utilization of theoretical and experimental approaches to sintering for tailoring the microstructure and properties of advanced ceramic materials", coordinator Prof. RNDr. Karel Maca, Dr., 2015-2017.
- FP7 (project no. 604036) "Natural inorganic polymers and smart functionalized micro-units applied in customized rapid prototyping of bioactive scaffolds (Bio-Scaffolds)", coordinator Prof. Werner E. G. Müller, 2013-2016.
- GACR P108-13-09967S "A fundamental study of the effect of synthesis and processing conditions on the structure and properties of (Ba,Ca)(Ti,Zr)O_3 lead-free piezoceramics", coordinator Prof. Tim Button, 2013-2015
- GACR P108-13-02476S "Pressure-less sintering of crack-free advanced ceramics by extremely fast heating ", coordinator Ing. David Salamon, PhD., 2013-2015
- LD11035 (Action COST MP0904) "Processing and properties of ferroics and multiferroics", coordinator Prof. RNDr. Karel Maca, Dr. 2011-2013.
- FSI-J-13-1967 "Syntheses and consolidation of bulk (Eu,Ba,Sr)TiO_3 ceramics", coordinator Ing. Martin Kachlik, 2013.
- FSI-J-12-18 "Processing of ferroic and multi-ferroic bulk ceramics", coordinator Ing. Martin Kachlik, 2012.
- OC102 (Action COST 539) "Processing of electro-ceramics from nano-powders", coordinator Prof. RNDr. Karel Maca, Dr. 2006-2009.

10. Literature

[1] HALLIDAY, D., RESNICK, R.,WALKER, J. *Fundamentals of Physics*; John Wiley And Sons Ltd: United Kingdom, 2007.

[2] LERNER, L. S. *Physics for Scientists and Engineers*; Jones and Bartlett Publishers: United Kingdom, 1997.

[3] CARTER, C. B.,NORTON, M. G. *Ceramic materials : science and engineering*; Springer: New York, 2007.

[4] MANBACHI, A.,COBBOLD, R. S. C. Development and application of piezoelectric materials for ultrasound generation and detection, *Ultrasound,* 2011, vol. 19, pp. 187.

[5] JAFFE, B., COOK, W. R.,JAFFE, H. In *Piezoelectric Ceramics*; Academic Press: 1971, p 92.

[6] MOULSON, A. J.,HERBERT, J. M. In *Electroceramics*; John Wiley & Sons, Ltd: 2003, p 339.

[7] HILL, N. A. Why Are There so Few Magnetic Ferroelectrics?, *J. Phys. Chem. B,* 2000, vol. 104, pp. 6694.

[8] CROSS, L. E. Ferroelectric materials for electromechanical transducer applications, *Materials Chemistry and Physics,* 1996, vol. 43, pp. 108

[9] SCHNEIDER, T., BECK, H.,STOLL, E. Quantum effects in an n-component vector model for structural phase transitions, *Physical Review B,* 1976, vol. 13, pp. 1123.

[10] MULLER, K. A.,BURKARD, H. SRTIO3 - INTRINSIC QUANTUM PARA-ELECTRIC BELOW 4-K, *Physical Review B,* 1979, vol. 19, pp. 3593.

[11] WEISS, P. *Journal de Physique,* 1907, vol. 6, pp. 661.

[12] STONER, E. C. *Philosophical Magazine,* 1933, vol. 15, pp. 1080.

[13] SCHMID, H. Multi-ferroic magnetoelectrics, *Ferroelectrics,* 1994, vol. 162, pp. 317.

[14] SPALDIN, N. A.,FIEBIG, M. Materials science. The renaissance of magnetoelectric multiferroics, *Science,* 2005, vol. 309, pp. 391.

[15] SPALDIN, N. A., CHEONG, S.-W.,RAMESH, R. Multiferroics: Past, present, and future, *Physics Today,* 2010, vol. 63, pp. 38.

[16] DEBYE, P. Bemerkung zu einigen neuen Versuchen über einen magneto-elektrischen Richteffekt, *Z. Physik,* 1926, vol. 36, pp. 300.

[17] FIEBIG, M. Revival of the magnetoelectric effect, *Journal of Physics D: Applied Physics,* 2005, vol. 38, pp. R123.

[18] BROWN, W. F., HORNREIC, R. M.,SHTRIKMAN, S. UPPER BOUND ON MAGNETOELECTRIC SUSCEPTIBILITY, *Physical Review,* 1968, vol. 168, pp. 574.

[19] WANG, J., NEATON, J. B., ZHENG, H., NAGARAJAN, V., OGALE, S. B., LIU, B., VIEHLAND, D., VAITHYANATHAN, V., SCHLOM, D. G., WAGHMARE, U. V., SPALDIN, N. A., RABE, K. M., WUTTIG, M.,RAMESH, R. Epitaxial BiFeO3 multiferroic thin film heterostructures, *Science,* 2003, vol. 299, pp. 1719.

[20] KITAGAWA, Y., HIRAOKA, Y., HONDA, T., ISHIKURA, T., NAKAMURA, H.,KIMURA, T. Low-field magnetoelectric effect at room temperature, *Nat. Mater.,* 2010, vol. 9, pp. 797.

[21] BIBES, M.,BARTHELEMY, A. Multiferroics: Towards a magnetoelectric memory, *Nat. Mater.,* 2008, vol. 7, pp. 425.

[22] SHANNON, R. D. REVISED EFFECTIVE IONIC-RADII AND SYSTEMATIC STUDIES OF INTERATOMIC DISTANCES IN HALIDES AND CHALCOGENIDES, *Acta Crystallogr. Sect. A,* 1976, vol. 32, pp. 751.

[23] MIZOKAWA, T., KHOMSKII, D. I.,SAWATZKY, G. A. Interplay between orbital ordering and lattice distortions in LaMnO3, YVO3, and YTiO3, *Physical Review B,* 1999, vol. 60, pp. 7309.

[24] MCKISSIC, K.,MACK, J. Energy and beyond: Studying the energetics of high-speed ball milling (HSBM) using Diels-Alder reactions, *Abstr. Pap. Am. Chem. Soc.,* 2013, vol. 245, pp. 1.
[25] DASH, S. K., KANT, S., DALAI, B., SWAIN, M. D.,SWAIN, B. B. Characterization and dielectric properties of barium zirconium titanate prepared by solid state reaction and high energy ball milling processes, *Indian J. Phys.,* 2014, vol. 88, pp. 129.
[26] SHEN, J. Z.,KOSMAČ, T. *Advanced ceramics for dentistry*, 2014.
[27] KRELL, A.,BLANK, P. GRAIN-SIZE DEPENDENCE OF HARDNESS IN DENSE SUBMICROMETER ALUMINA, *Journal of the American Ceramic Society,* 1995, vol. 78, pp. 1118.
[28] KRELL, A.,BLANK, P. The influence of shaping method on the grain size dependence of strength in dense submicrometre alumina, *Journal of the European Ceramic Society,* 1996, vol. 16, pp. 1189.
[29] O, Y. T., KOO, J. B., HONG, K. J., PARK, J. S.,SHIN, D. C. Effect of grain size on transmittance and mechanical strength of sintered alumina, *Mater. Sci. Eng. A-Struct. Mater. Prop. Microstruct. Process.,* 2004, vol. 374, pp. 191.
[30] HE, Y. J., WINNUBST, L., BURGGRAAF, A. J., VERWEIJ, H., VANDERVARST, P. G. T.,DEWITH, B. Grain-size dependence of sliding wear in tetragonal zirconia polycrystals, *Journal of the American Ceramic Society,* 1996, vol. 79, pp. 3090.
[31] LAWSON, S. Eenviromental degradation of zirconia ceramics, *Journal of the European Ceramic Society,* 1995, vol. 15, pp. 485.
[32] KANG, S.-J. L. *Sintering : densification, grain growth, and microstructure*; Elsevier: Amsterdam, 2008.
[33] RAHAMANN, M. N. *Sintering of Ceramics*; Taylor & Francis Group, LLC: University of Missouri-Rolla, USA, 2008.
[34] SU, H. H.,JOHNSON, D. L. Master sintering curve: A practical approach to sintering, *Journal of the American Ceramic Society,* 1996, vol. 79, pp. 3211.
[35] MACA, K.,SIMONIKOVA, S. Effect of sintering schedule on grain size of oxide ceramics, *J. Mater. Sci.,* 2005, vol. 40, pp. 5581.
[36] WANG, J. D.,RAJ, R. ESTIMATE OF THE ACTIVATION-ENERGIES FOR BOUNDARY DIFFUSION FROM RATE-CONTROLLED SINTERING OF PURE ALUMINA, AND ALUMINA DOPED WITH ZIRCONIA OR TITANIA, *Journal of the American Ceramic Society,* 1990, vol. 73, pp. 1172.
[37] CHEN, I. W.,WANG, X. H. Sintering dense nanocrystalline ceramics without final-stage grain growth, *Nature,* 2000, vol. 404, pp. 168.
[38] BODISOVA, K., SAJGALIK, P., GALUSEK, D.,SVANCAREK, P. Two-stage sintering of alumina with submicrometer grain size, *Journal of the American Ceramic Society,* 2007, vol. 90, pp. 330.
[39] MAZAHERI, M., VALEFI, M., HESABI, Z. R.,SADRNEZHAAD, S. K. Two-step sintering of nanocrystalline 8Y(2)O(3) stabilized ZrO2 synthesized by glycine nitrate process, *Ceramics International,* 2009, vol. 35, pp. 13.
[40] WANG, X. H., DENG, X. Y., BAI, H. L., ZHOU, H., QU, W. G., LI, L. T.,CHEN, I. W. Two-step sintering of ceramics with constant grain-size, II: BaTiO3 and Ni-Cu-Zn ferrite, *Journal of the American Ceramic Society,* 2006, vol. 89, pp. 438.
[41] MACA, K., POUCHLY, V.,SHEN, Z. J. Two-Step Sintering and Spark Plasma Sintering of Al2O3, ZrO2 and SrTiO3 ceramics, *Integr. Ferroelectr.,* 2008, vol. 99, pp. 114.
[42] BALAYA, P., AHRENS, M., KIENLE, L., MAIER, J., RAHMATI, B., LEE, S. B.,SIGLE, W. Synthesis and characterization of nanocrystalline SrTiO3, *Journal of the American Ceramic Society,* 2006, vol. 89, pp. 2804.

[43] OGHBAEI, M.,MIRZAEE, O. Microwave versus conventional sintering: A review of fundamentals, advantages and applications, *Journal of Alloys and Compounds,* 2010, vol. 494, pp. 175.
[44] CHAIM, R. Superfast densification of nanocrystalline oxide powders by spark plasma sintering, *J. Mater. Sci.,* 2006, vol. 41, pp. 7862.
[45] HULBERT, D. M., ANDERS, A., DUDINA, D. V., ANDERSSON, J., JIANG, D., UNUVAR, C., ANSELMI-TAMBURINI, U., LAVERNIA, E. J.,MUKHERJEE, A. K. The absence of plasma in "spark plasma sintering", *Journal of Applied Physics,* 2008, vol. 104, pp. 033305.
[46] KIM, B.-N., HIRAGA, K., MORITA, K.,YOSHIDA, H. Spark plasma sintering of transparent alumina, *Scripta Materialia,* 2007, vol. 57, pp. 607.
[47] MUNIR, Z. A., ANSELMI-TAMBURINI, U.,OHYANAGI, M. The effect of electric field and pressure on the synthesis and consolidation of materials: A review of the spark plasma sintering method, *J. Mater. Sci.,* 2006, vol. 41, pp. 763.
[48] LEE, J. H., FANG, L., VLAHOS, E., KE, X., JUNG, Y. W., KOURKOUTIS, L. F., KIM, J. W., RYAN, P. J., HEEG, T., ROECKERATH, M., GOIAN, V., BERNHAGEN, M., UECKER, R., HAMMEL, P. C., RABE, K. M., KAMBA, S., SCHUBERT, J., FREELAND, J. W., MULLER, D. A., FENNIE, C. J., SCHIFFER, P., GOPALAN, V., JOHNSTON-HALPERIN, E.,SCHLOM, D. G. A strong ferroelectric ferromagnet created by means of spin-lattice coupling, *Nature,* 2010, vol. 466, pp. 954.
[49] BUSSMANN-HOLDER, A., KOHLER, J., KREMER, R. K.,LAW, J. M. Relation between structural instabilities in EuTiO3 and SrTiO3, *Physical Review B,* 2011, vol. 83, pp. 4.
[50] KAMBA, S., NUZHNYY, D., VANEK, P., SAVINOV, M., KNIZEK, K., SHEN, Z., SANTAVA, E., MACA, K., SADOWSKI, M.,PETZELT, J. Magnetodielectric effect and optic soft mode behaviour in quantum paraelectric EuTiO(3) ceramics, *Epl,* 2007, vol. 80, pp. 6.
[51] BROUS, J., FANKUCHEN, I.,BANKS, E. Rare Earth Titanates with a Perovskite Structure, *Acta Crystallogr,* 1953, vol. 6, pp. 67.
[52] SHAFER, M. W. Preparation and Crystal Chemistry of Divalent Europium Compounds, *Journal of Applied Physics,* 1965, vol. 36, pp. 1145.
[53] ZONG, Y., KUGIMIYA, K., FUJITA, K., AKAMATSU, H., HIRAO, K.,TANAKA, K. Preparation and magnetic properties of amorphous EuTiO3 thin films, *Journal of Non-Crystalline Solids,* 2010, vol. 356, pp. 2389.
[54] BESSAS, D., RUSHCHANSKII, K. Z., KACHLIK, M., DISCH, S., GOURDON, O., BEDNARCIK, J., MACA, K., SERGUEEV, I., KAMBA, S., LEŽAIĆ, M.,HERMANN, R. P. Lattice instabilities in bulk EuTiO_{3}, *Physical Review B,* 2013, vol. 88, pp.
[55] GOIAN, V., KAMBA, S., PACHEROVÁ, O., DRAHOKOUPIL, J., PALATINUS, L., DUŠEK, M., ROHLÍČEK, J., SAVINOV, M., LAUFEK, F., SCHRANZ, W., FUITH, A., KACHLÍK, M., MACA, K., SHKABKO, A., SAGARNA, L., WEIDENKAFF, A.,BELIK, A. A. Antiferrodistortive phase transition in EuTiO3, *Physical Review B,* 2012, vol. 86, pp.
[56] MACA, K., KACHLIK, M., VANEK, P., GAUTAM, D.,WINTERER, M. The influence of sintering conditions on the phase purity of bulk EuTiO3and Eu0.5Ba0.5TiO3ceramics, *Phase Transitions,* 2013, vol. 86, pp. 737.
[57] KINGERY, W. D., BOWEN, H. K.,UHLMANN, D. R. *Introduction to Ceramics*; John Willey & Sons: New York, 1976.
[58] MACA, K., DOBSAK, P.,BOCCACCINI, A. R. Fabrication of graded porous ceramics using alumina-carbon powder mixtures, *Ceramics International,* 2001, vol. 27, pp. 577.

[59] MACA, K.,CIHLAR, J. Study of high-temperature processes at interphase boundary of chromium (titanium) and alumina, *Ceram.-Silik.,* 1997, vol. 41, pp. 13.
[60] BARIN, I. *Thermodynamic Data of Pure Substances*; VCH Verlagsgesellschaft mbH: Weinheim, 1993; Vol. D-6940.
[61] MEIR, S., KALABUKHOV, S., FROUMIN, N., DARIEL, M. P.,FRAGE, N. Synthesis and Densification of Transparent Magnesium Aluminate Spinel by SPS Processing, *Journal of the American Ceramic Society,* 2009, vol. 92, pp. 358.
[62] WEI, T., LIU, H. P., CHEN, Y. F., YAN, H. Y.,LIU, J. M. Preparation, magnetic characterization, and optical band gap of EuTiO3 nanoparticles, *Applied Surface Science,* 2011, vol. 257, pp. 4505.
[63] HENDERSON, N. L., KE, X., SCHIFFER, P.,SCHAAK, R. E. Solution precursor synthesis and magnetic properties of Eu1−xCaxTiO3, *Journal of Solid State Chemistry,* 2010, vol. 183, pp. 631.
[64] XU, G., HUANG, X. Q., KRSTIC, V., CHEN, S. Q., YANG, X., CHAO, C. Y., SHEN, G.,HAN, G. R. Hydrothermal synthesis of single-crystalline tetragonal perovskite PbTiO3 nanosheets with dominant (001) or (111) facets, *Crystengcomm,* 2014, vol. 16, pp. 4373.
[65] YANG, X., REN, Z. H., XU, G., CHAO, C. Y., JIANG, S., DENG, S. Q., SHEN, G., WEI, X.,HAN, G. R. Monodisperse hollow perovskite BaTiO3 nanostructures prepared by a sol gel hydrothermal method, *Ceramics International,* 2014, vol. 40, pp. 9663.
[66] PENG, J. M., ZHOU, Y., WANG, H., ZHOU, H. R.,CAI, S. Y. Hydrothermal synthesis and formation mechanism of photocatalytically active SrTiO3 nanocrystals using anatase TiO2 with different facets as a precursor, *Crystengcomm,* 2015, vol. 17, pp. 1805.
[67] RANJAN, R., SENYSHYN, A., BOYSEN, H., BAEHTZ, C.,FREY, F. Crystal structures of Na1/2Ln1/2TiO3 (Ln: La, Eu, Tb), *Journal of Solid State Chemistry,* 2007, vol. 180, pp. 995.
[68] SUN, PAI, H., NAKAMURA, T., SHAN, Y.-J., INAGUMA, Y.,ITOH, M. High temperature quantum paraelectricity in perovskite-type titanates Ln1/2 Na1/2 TiO3 (Ln = La, Pr, Nd, Sm, Eu, Gd and Tb), *Ferroelectrics,* 1997, vol. 200, pp. 93.
[69] SHEN, Z. J., JOHNSSON, M., ZHAO, Z.,NYGREN, M. Spark plasma sintering of alumina, *Journal of the American Ceramic Society,* 2002, vol. 85, pp. 1921.
[70] TAKEUCHI, T., TABUCHI, M., KAGEYAMA, H.,SUYAMA, Y. Preparation of dense BaTiO(3) ceramics with submicrometer grains by spark plasma sintering, *Journal of the American Ceramic Society,* 1999, vol. 82, pp. 939.
[71] DEMIRSKII, D. N.,RAGULYA, A. V. INITIAL KINETICS OF MICROWAVE SINTERING OF COPPER, *Powder Metall. Met. Ceram.,* 2010, vol. 49, pp. 147.
[72] MIAO, Y. M., ZHANG, Q. L., YANG, H.,WANE, H. P. Low-temperature synthesis of nano-crystalline magnesium titanate materials by the sol-gel method, *Mater. Sci. Eng. B-Solid State Mater. Adv. Technol.,* 2006, vol. 128, pp. 103.
[73] DHARMARAJ, N., PARK, H. C., LEE, B. M., VISWANATHAMURTHI, P., KIM, H. Y.,LEE, D. R. Preparation and morphology of magnesium titanate nanofibres via electrospinning, *Inorg. Chem. Commun.,* 2004, vol. 7, pp. 431.
[74] STUBICAR, N., TONEJC, A.,STUBICAR, M. Microstructural evolution of some MgO-TiO2 and MgO-Al2O3 powder mixtures during high-energy ball milling and post-annealing studied by X-ray diffraction, *Journal of Alloys and Compounds,* 2004, vol. 370, pp. 296.
[75] CHENG, H. M., XU, B.,MA, J. M. Preparation of MgTiO3 by an improved chemical co-precipitation method, *J. Mater. Sci. Lett.,* 1997, vol. 16, pp. 1570.

[76] THATIKONDA, S. K., GOSWAMI, D.,DOBBIDI, P. Effects of CeO2 nanoparticles and annealing temperature on the microwave dielectric properties of MgTiO3 ceramics, *Ceramics International,* 2014, vol. 40, pp. 1125.
[77] KOZAWA, T., ONDA, A.,YANAGISAWA, K. Preparation of alkaline-earth titanates by accelerated solid-state reaction in water vapor atmosphere, *Journal of the European Ceramic Society,* 2010, vol. 30, pp. 3435.
[78] FERREIRA, V. M., AZOUGH, F., FREER, R.,BAPTISTA, J. L. The effect of Cr and La on MgTiO3 and MgTiO3-CaTiO3 microwave dielectric ceramics, *J. Mater. Res.,* 1997, vol. 12, pp. 3293.
[79] PIAGAI, R., KIM, I. T., PARK, J. G.,KIM, Y. Microwave dielectric properties of magnesium calcium titanate ceramics prepared by semi-alkoxide methods, *J. Korean Phys. Soc.,* 1998, vol. 32, pp. S367.
[80] TANG, B., LI, H., FAN, P., YU, S.,ZHANG, S. The effect of Mg:Ti ratio on the phase composition and microwave dielectric properties of MgTiO3 ceramics prepared by one synthetic process, *Journal of Materials Science: Materials in Electronics,* 2014, vol. 25, pp. 2482.
[81] FILIPOVIC, S., OBRADOVIC, N., PAVLOVIC, V. B., KOSANOVIC, D., MITRIC, M., MITROVIC, N., POUCHLY, V., KACHLIK, M.,MACA, K. Advantages of combined sintering compared to conventional sintering of mechanically activated magnesium titanate, *Science of Sintering,* 2014, vol. 46, pp. 283.
[82] WANG, P., LI, Y.,LU, Y. Enhanced piezoelectric properties of (Ba0.85Ca0.15)(Ti0.9Zr0.1)O3 lead-free ceramics by optimizing calcination and sintering temperature, *Journal of the European Ceramic Society,* 2011, vol. 31, pp. 2005.
[83] QIAO, S., WU, J., WU, B., ZHANG, B., XIAO, D.,ZHU, J. Effect of Ba0.85Ca0.15Ti0.90Zr0.10O3 content on the microstructure and electrical properties of Bi0.51(Na0.82K0.18) 0.50TiO3 ceramics, *Ceramics International,* 2012, vol. 38, pp. 4845.
[84] LIU, W.,REN, X. Large Piezoelectric Effect in Pb-Free Ceramics, *Phys. Rev. Lett.,* 2009, vol. 103, pp.
[85] DAMJANOVIC, D., BIANCOLI, A., BATOOLI, L., VAHABZADEH, A.,TRODAHL, J. Elastic, dielectric, and piezoelectric anomalies and Raman spectroscopy of 0.5Ba(Ti0.8Zr0.2)O3-0.5(Ba0.7Ca0.3)TiO3, *Applied Physics Letters,* 2012, vol. 100, pp. 192907.
[86] KRISHNAMOORTHY, P. R., RAMASWAMY, P.,NARAYANA, B. H. CaZrO3 additives to enhance capacitance properties in BaTiO3 ceramic capacitors, *Journal of Materials Science: Materials in Electronics,* 1992, vol. 3, pp. 176.
[87] LI, W., XU, Z., CHU, R., FU, P.,ZANG, G. Structural and dielectric properties in the (Ba1−xCax)(Ti0.95Zr0.05)O3 ceramics, *Current Applied Physics,* 2012, vol. 12, pp. 748.
[88] LI, C.-X., YANG, B., ZHANG, S.-T., ZHANG, R., SUN, Y., WANG, J.-J., WANG, R.-X.,CAO, W.-W. Phase transition, microstructure and electrical properties of Fe doped Ba0.70Ca0.30TiO3 lead-free piezoelectric ceramics, *Ceramics International,* 2013, vol. 39, pp. 8701.
[89] YOON, M.-S.,UR, S.-C. Effects of A-site Ca and B-site Zr substitution on dielectric properties and microstructure in tin-doped BaTiO3–CaTiO3 composites, *Ceramics International,* 2008, vol. 34, pp. 1941.
[90] WANG, W., LI, W. L., XU, D., CAO, W. P., HOU, Y. F.,FEI, W. D. Phase transitions in (1−x)BaZr0.2Ti0.8O3−xBa0.7Ca0.3TiO3 powders and ceramic pellets, *Ceramics International,* 2014, vol. 40, pp. 3933.

Attachment

$EuTiO_3$

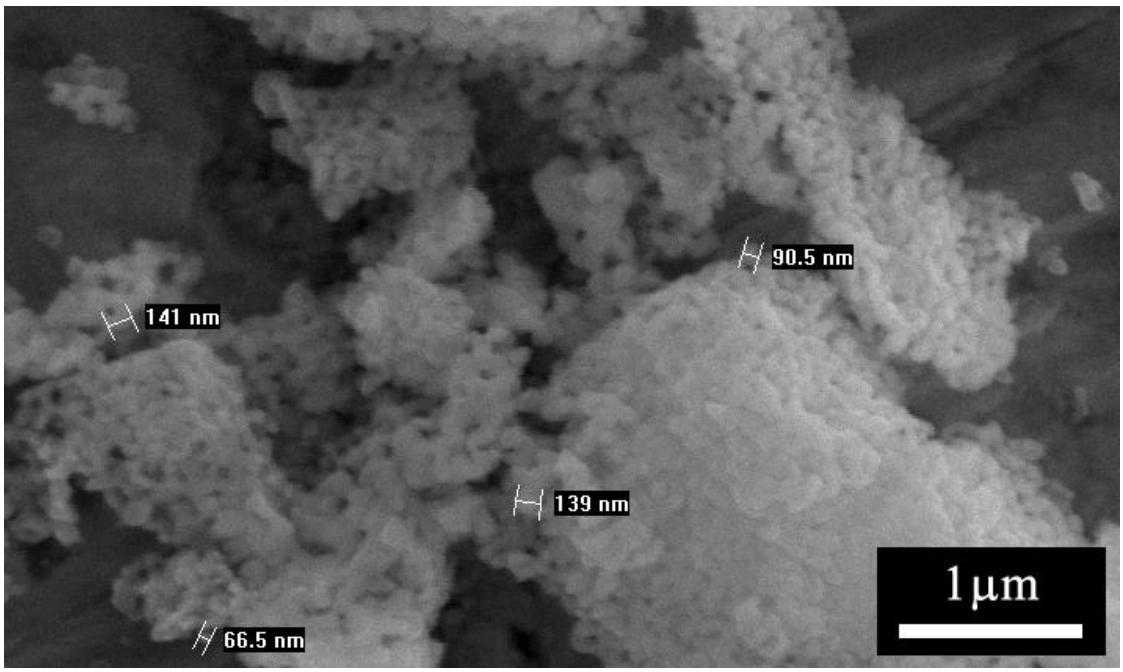

A-Fig. 1 Morphology of Eu_2O_3 (Ver.) powder by SEM.

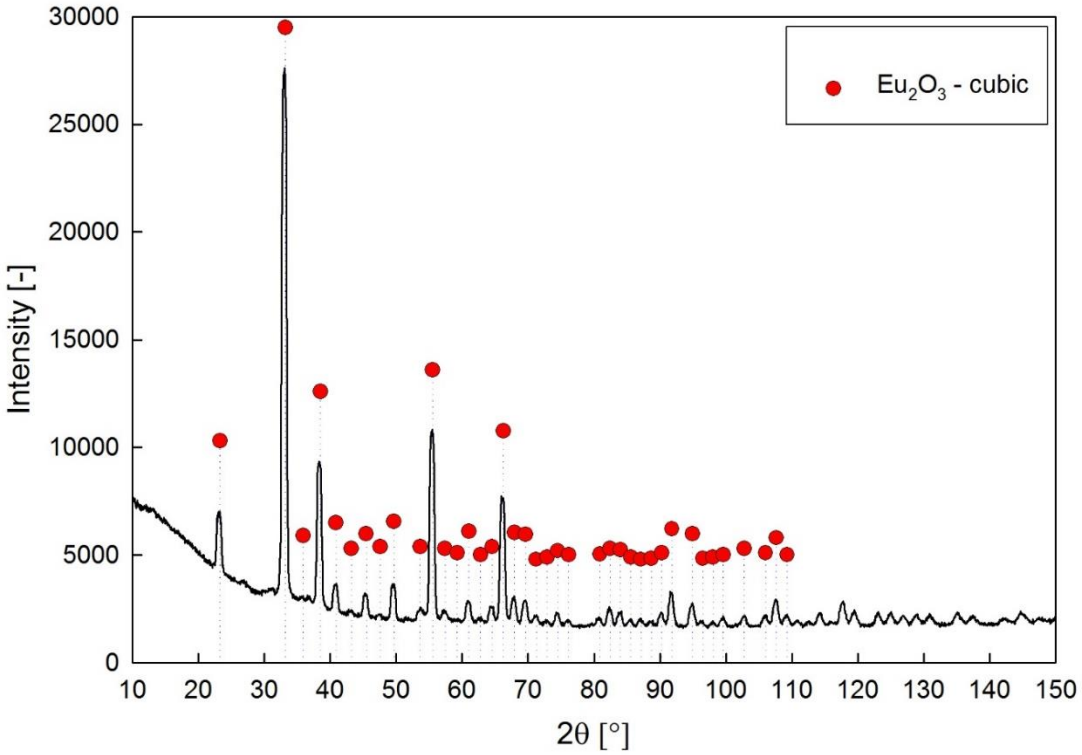

A-Fig. 2 XRD diffractogram of the Eu_2O_3 (Ver.) powder.

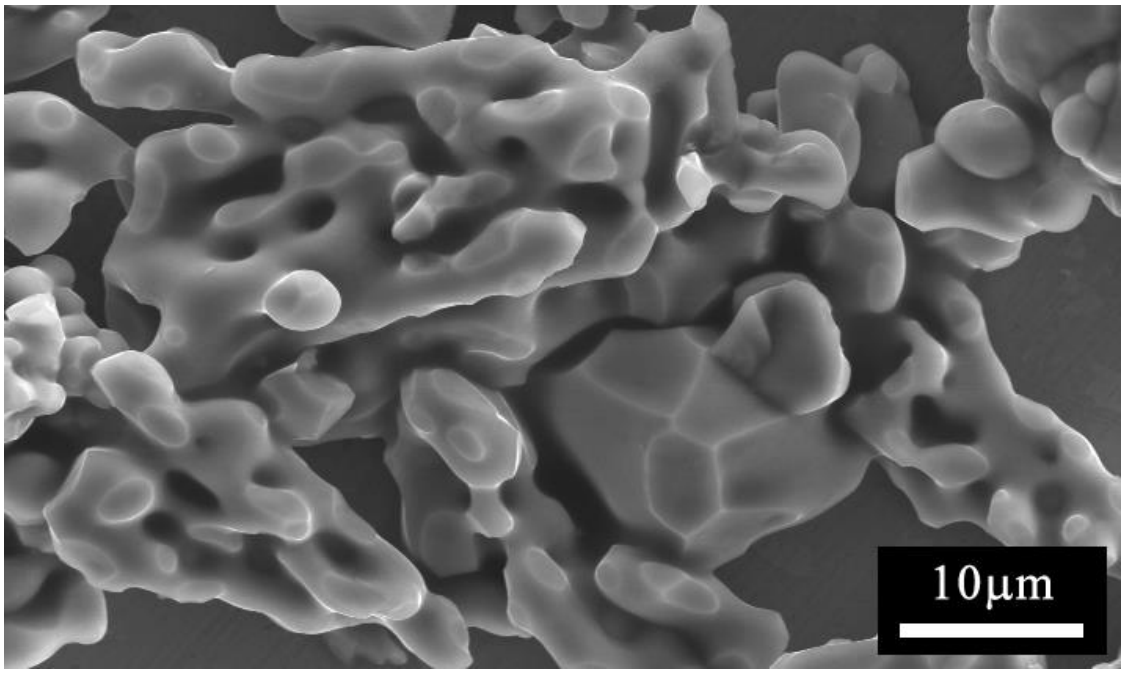

A-Fig. 3 Morphology of Ti_2O_3 (Ver.) powder by SEM.

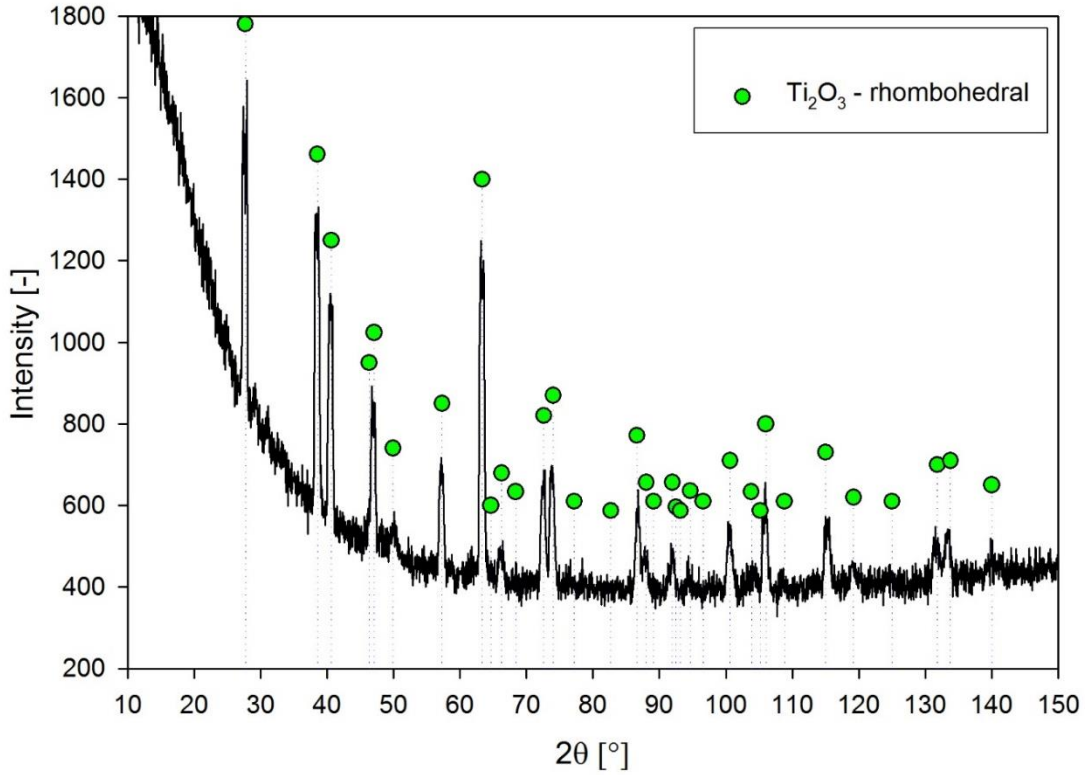

A-Fig. 4 XRD diffractogram of the Ti_2O_3 (Ver.) powder.

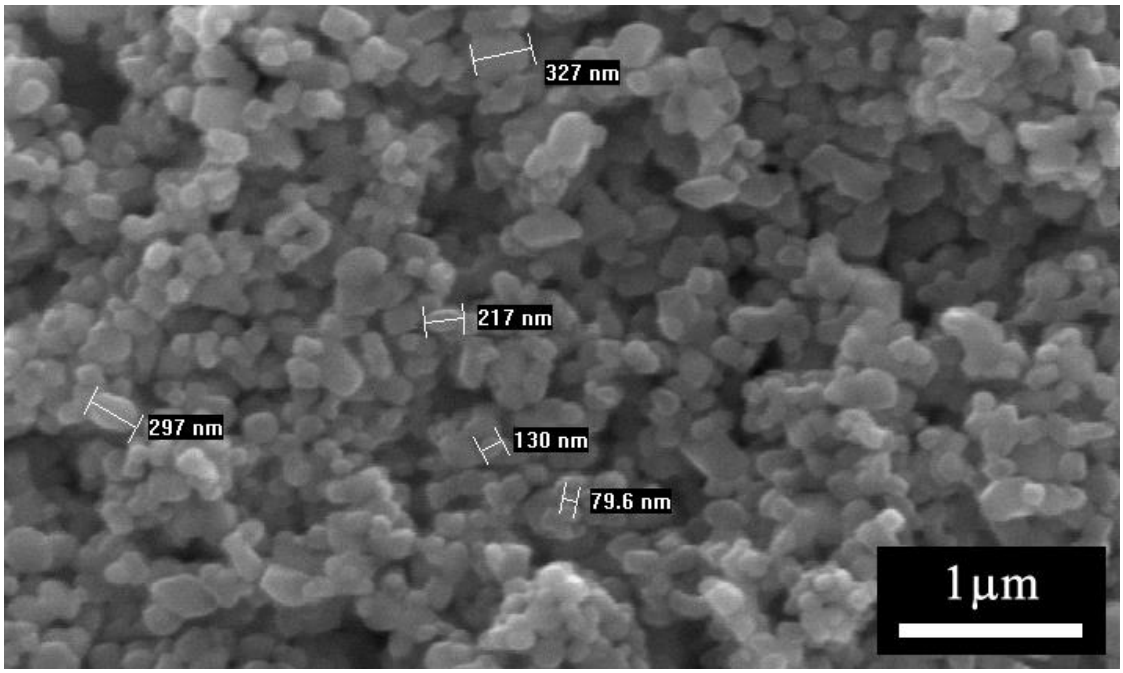

A-Fig. 5 Morphology of TiO_2-A (Ver.) by SEM

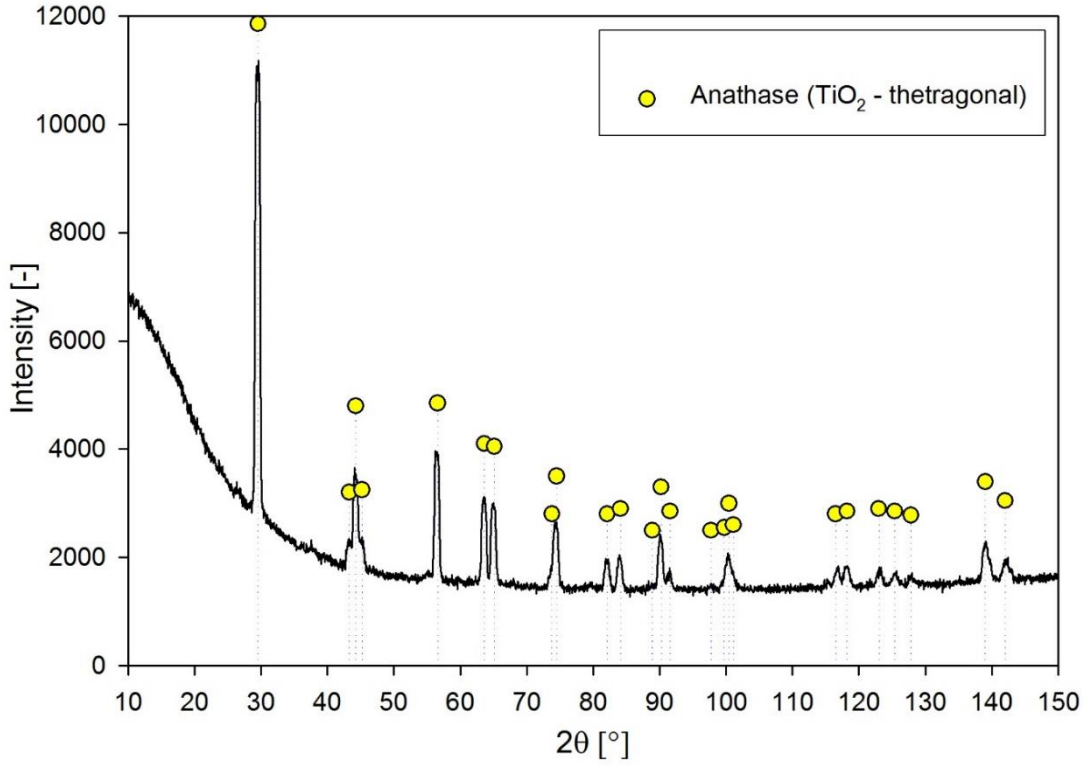

A-Fig. 6 XRD diffractogram of the TiO_2-A (Ver.) powder

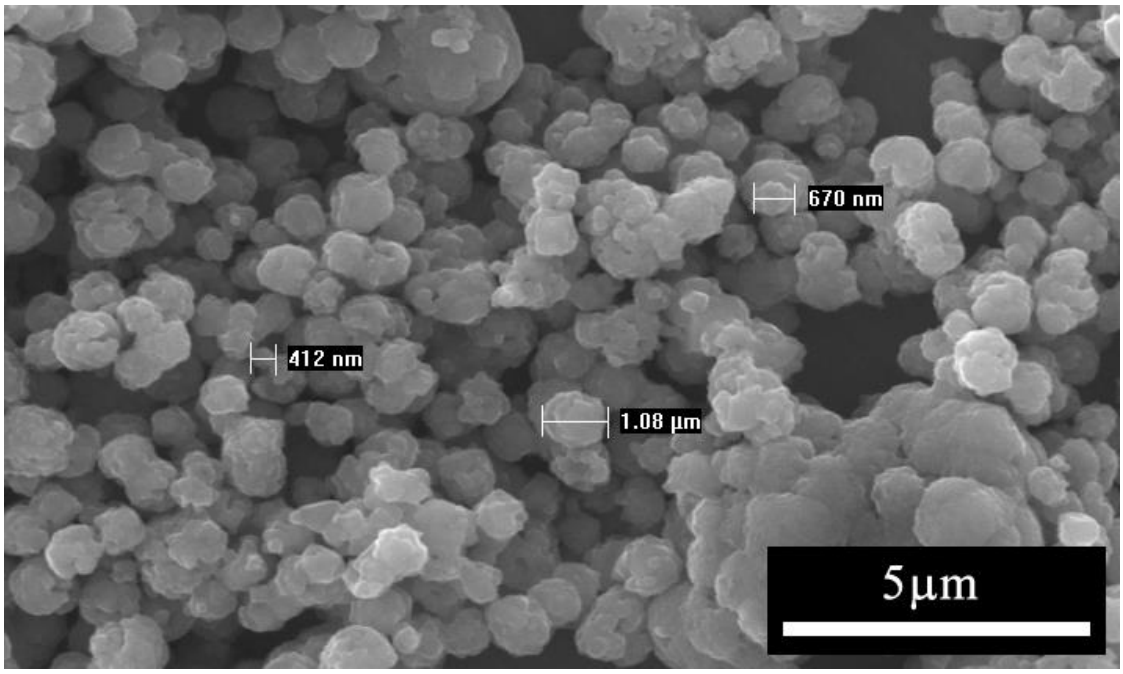

A-Fig. 7 Morphology of TiO_2-R (Ver.) by SEM

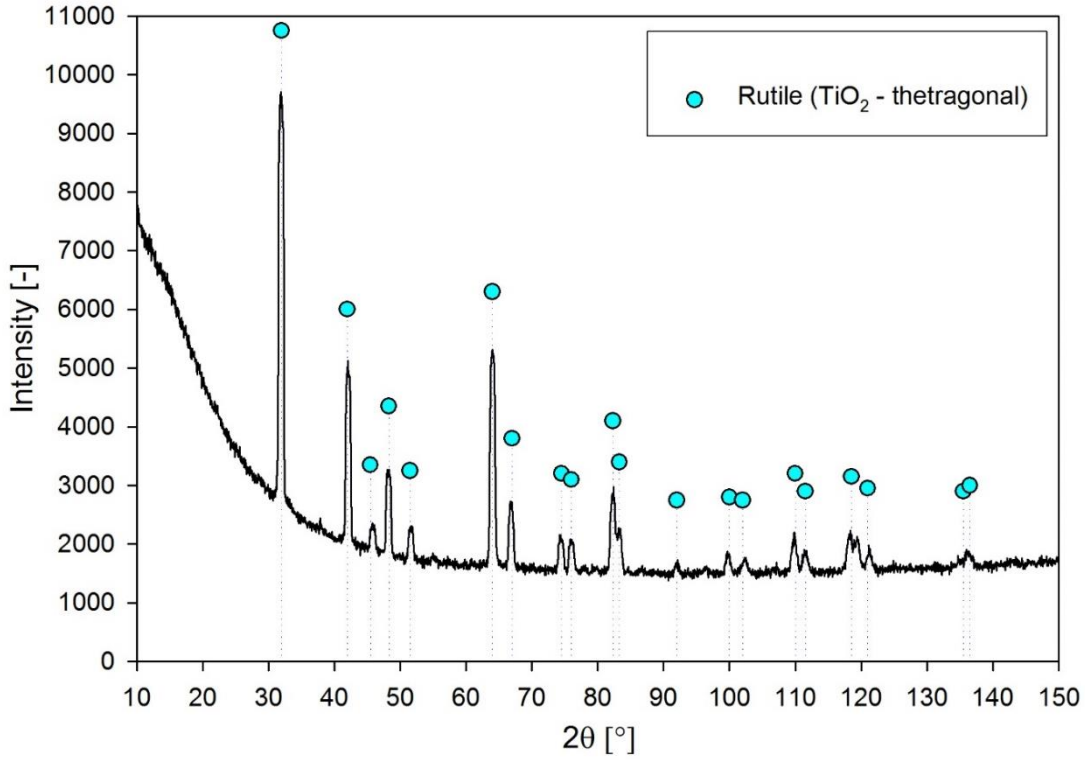

A-Fig. 8 XRD diffractogram of the TiO_2-R (Ver.) powder

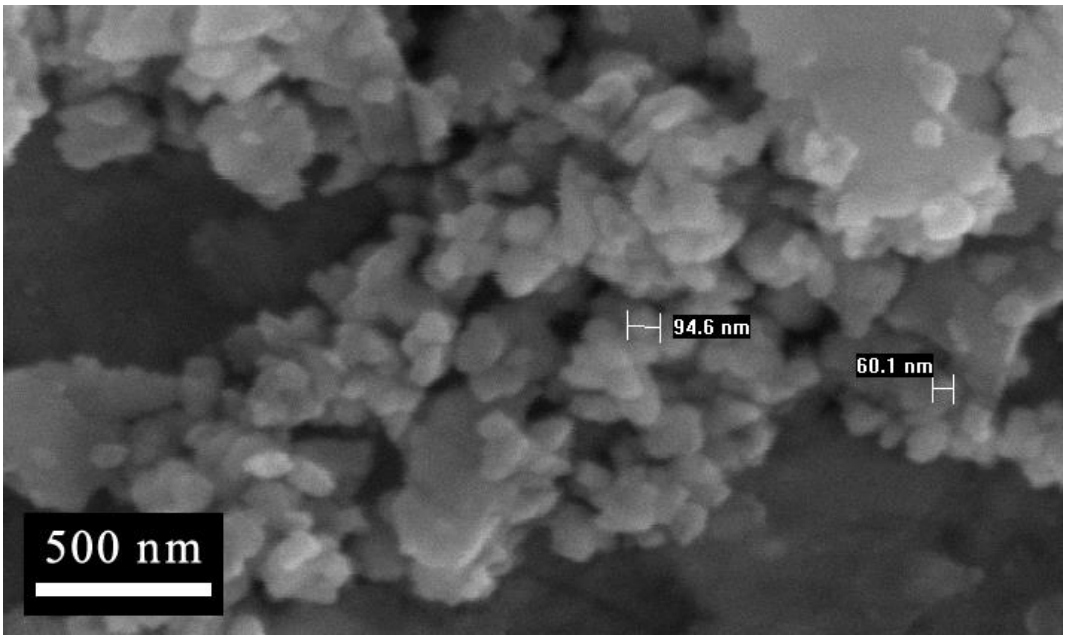

A-Fig. 9 Morphology of the MIX 1 – Eu_2O_3 + Ti_2O_3 after milling

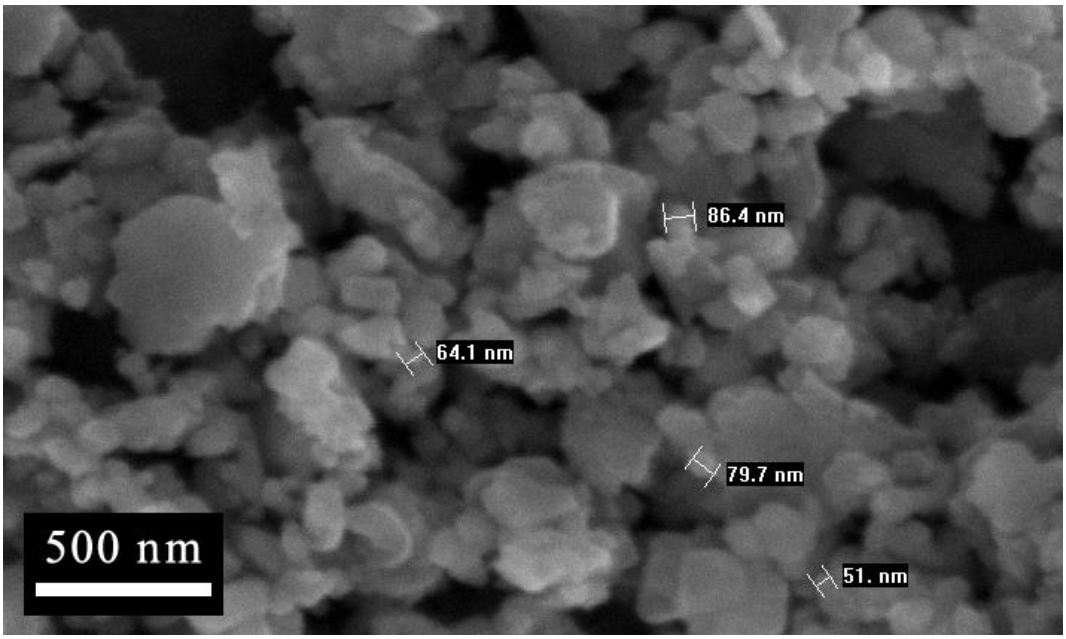

A-Fig. 10 Morphology of the MIX 2 – Eu_2O_3 + TiO_2-A after milling

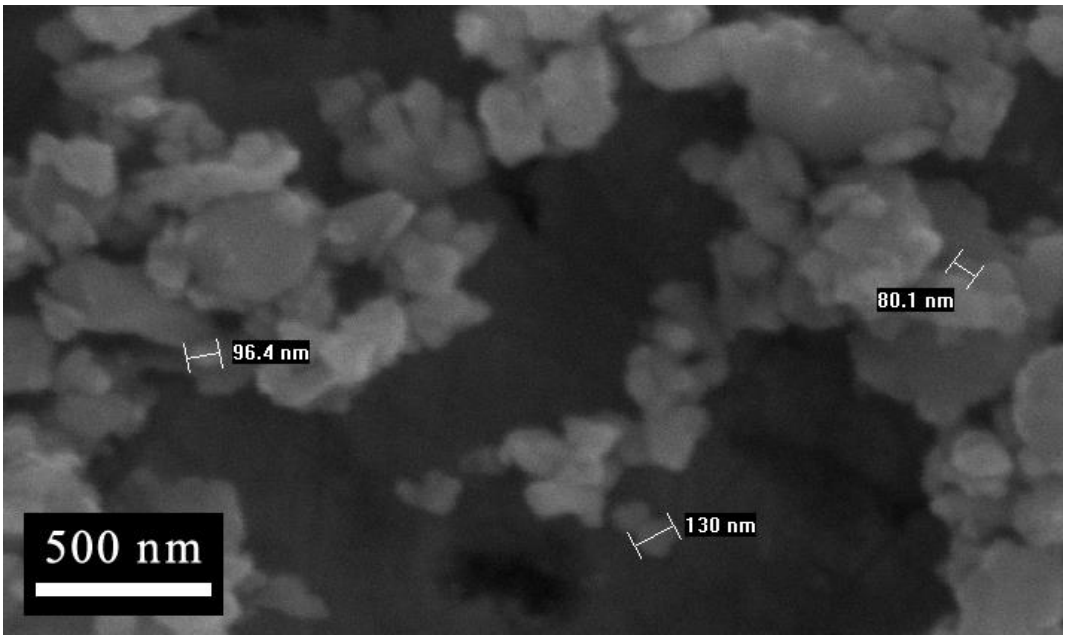

A-Fig. 11 Morphology of the MIX 3 – Eu_2O_3 + TiO_2-R after milling

Ba(Ca)Ti(Zr)O_3

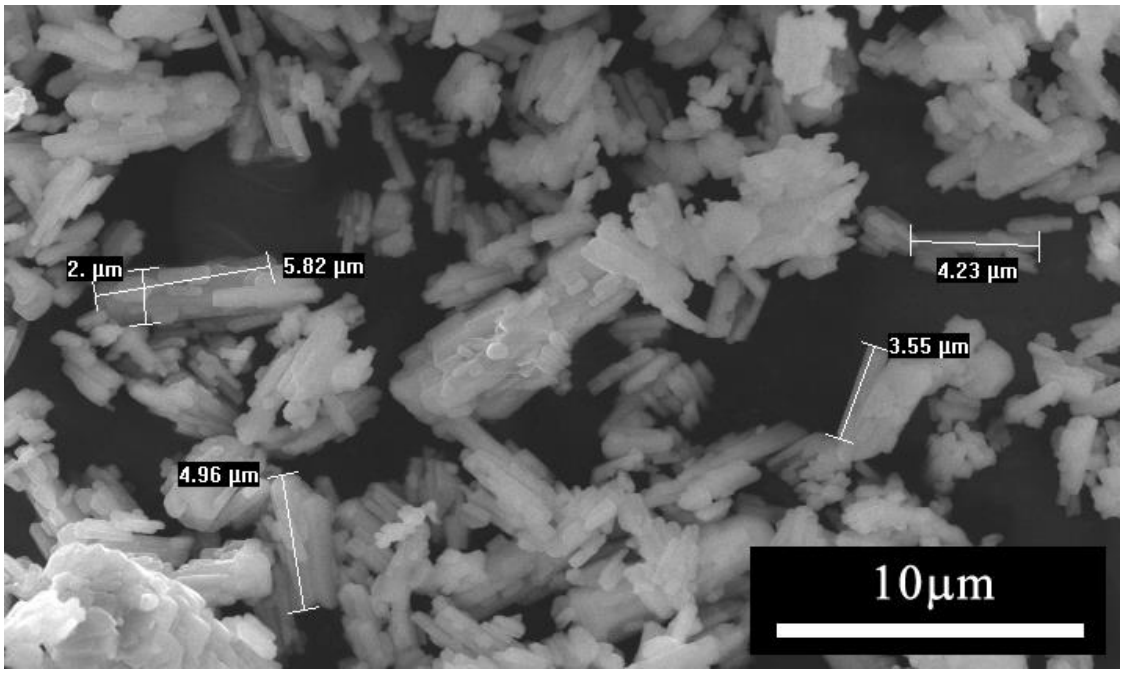

A-Fig. 12 Morphology of $BaCO_3$ powder by SEM

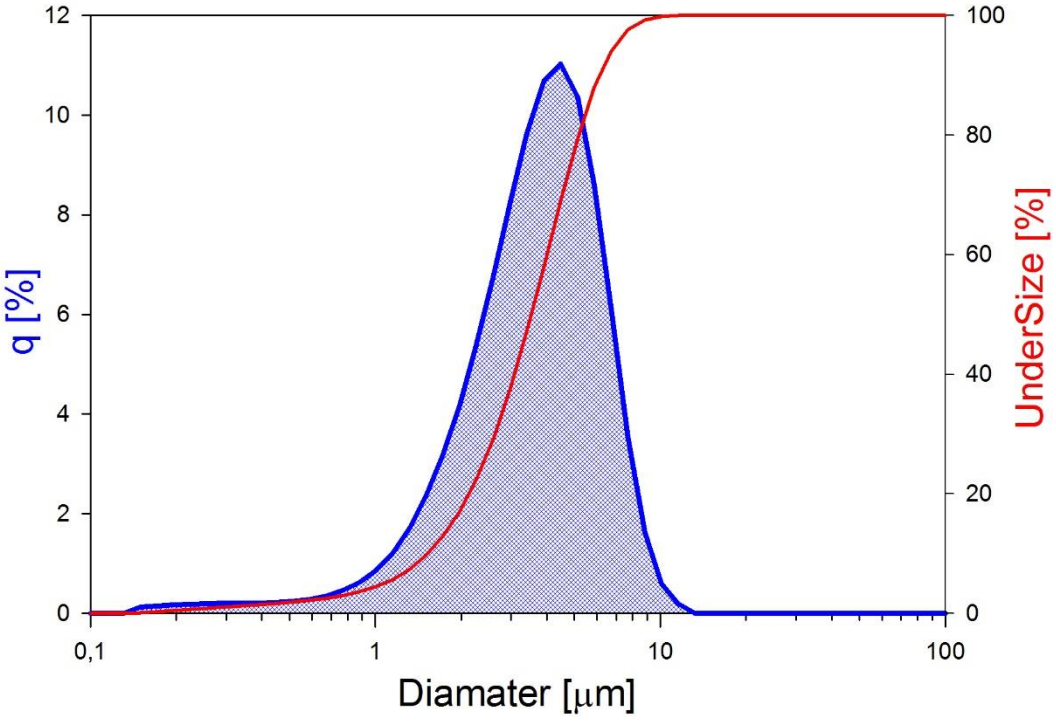

A-Fig. 13 Particle (agglomeration) size distribution of $BaCO_3$ powder established by laser diffraction.

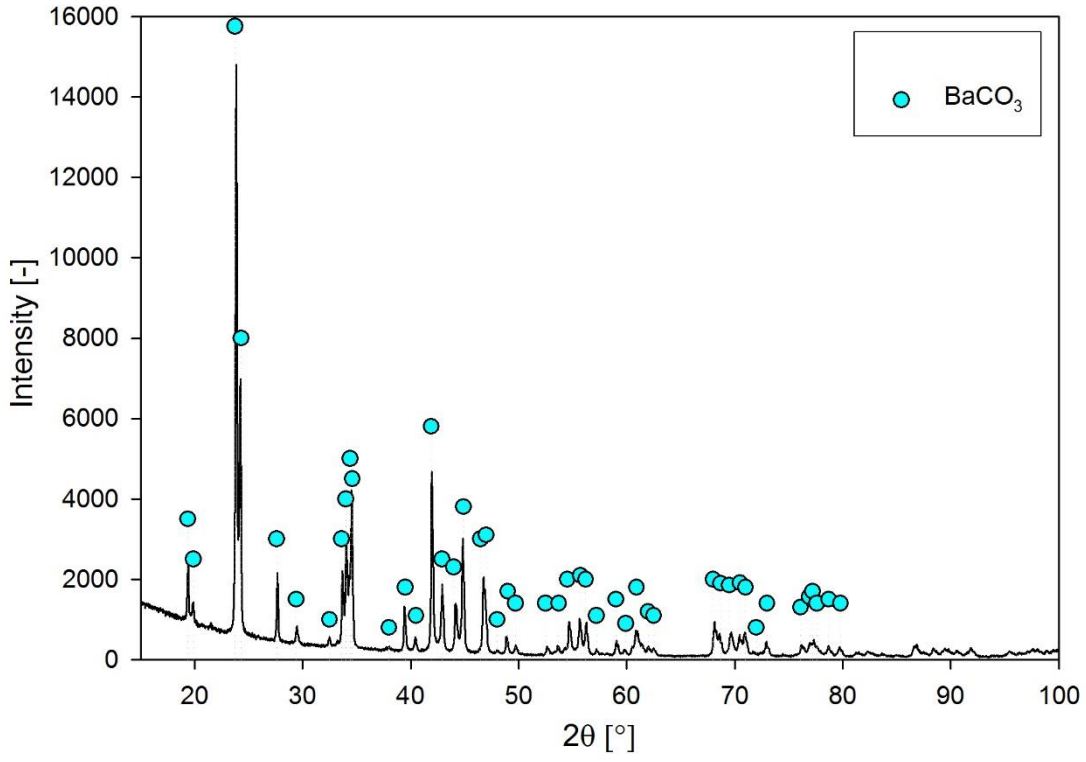

A-Fig. 14 XRD diffractogram of the single phase powder $BaCO_3$ (orthorhombic).

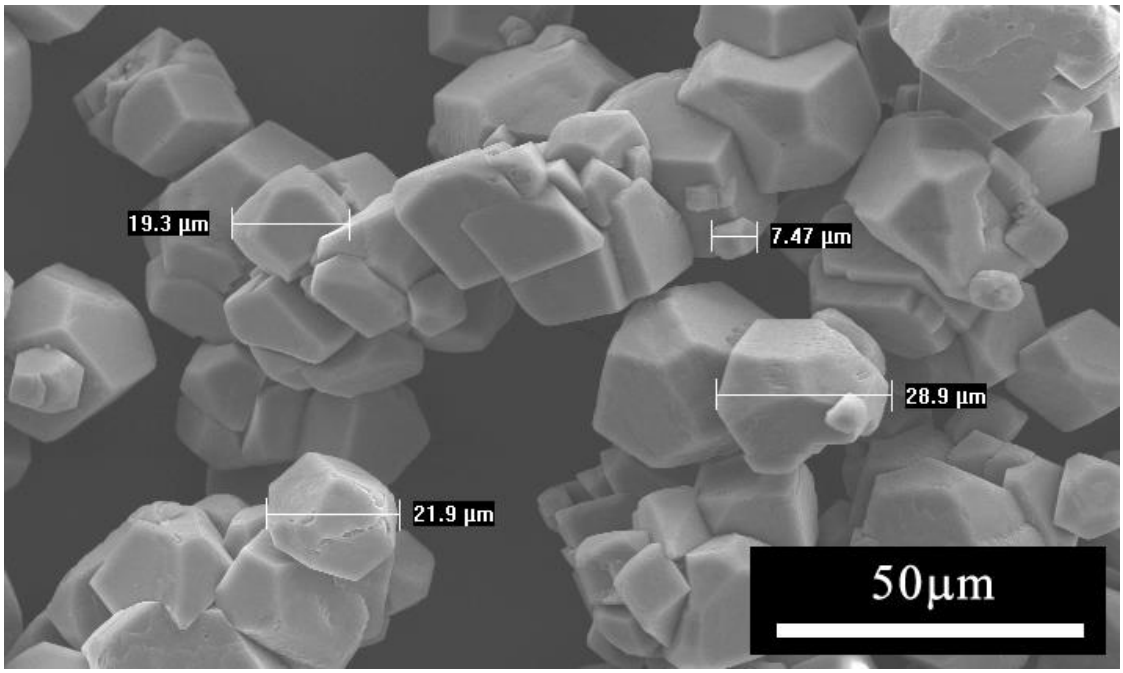

A-Fig. 15 Morphology of $CaCO_3$ powder by SEM.

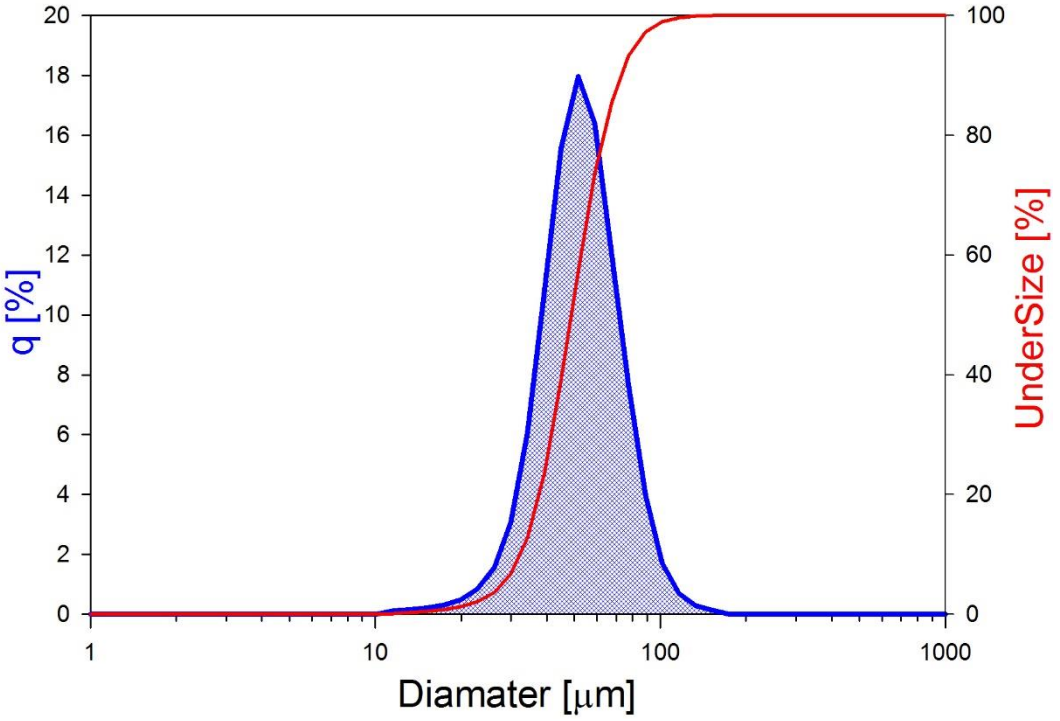

A-Fig. 16 Particle (agglomeration) size distribution of $CaCO_3$ powder established by laser diffraction

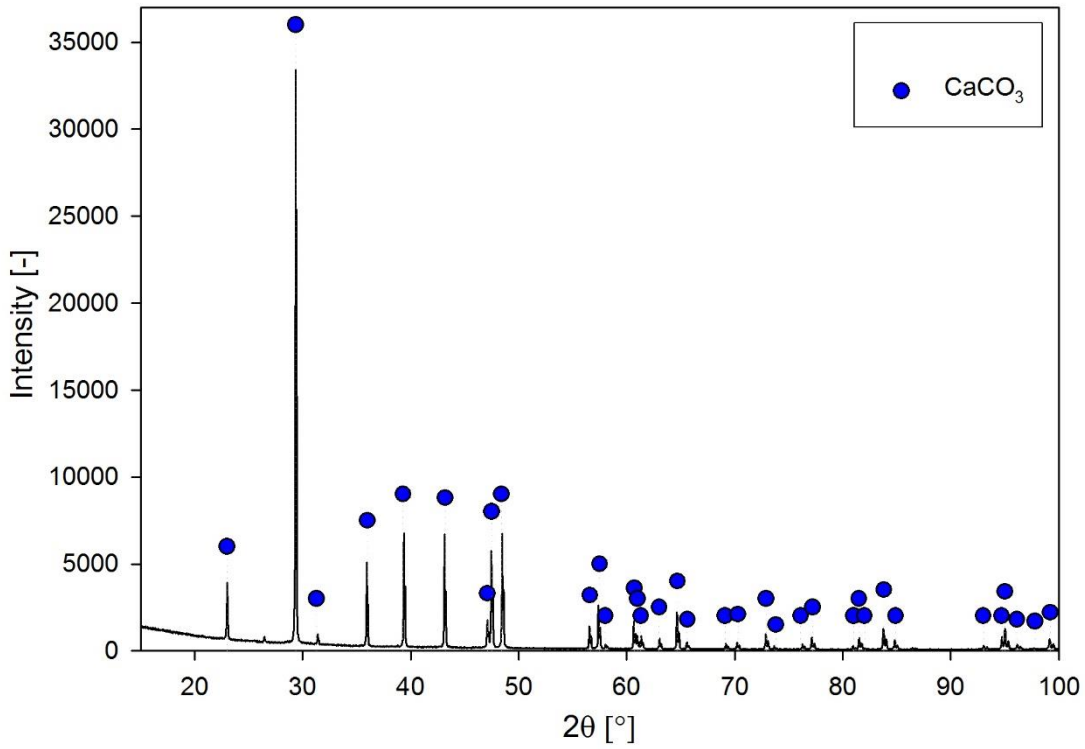

A-Fig. 17 XRD diffractogram of the single phase powder $CaCO_3$ (rhombohedral).

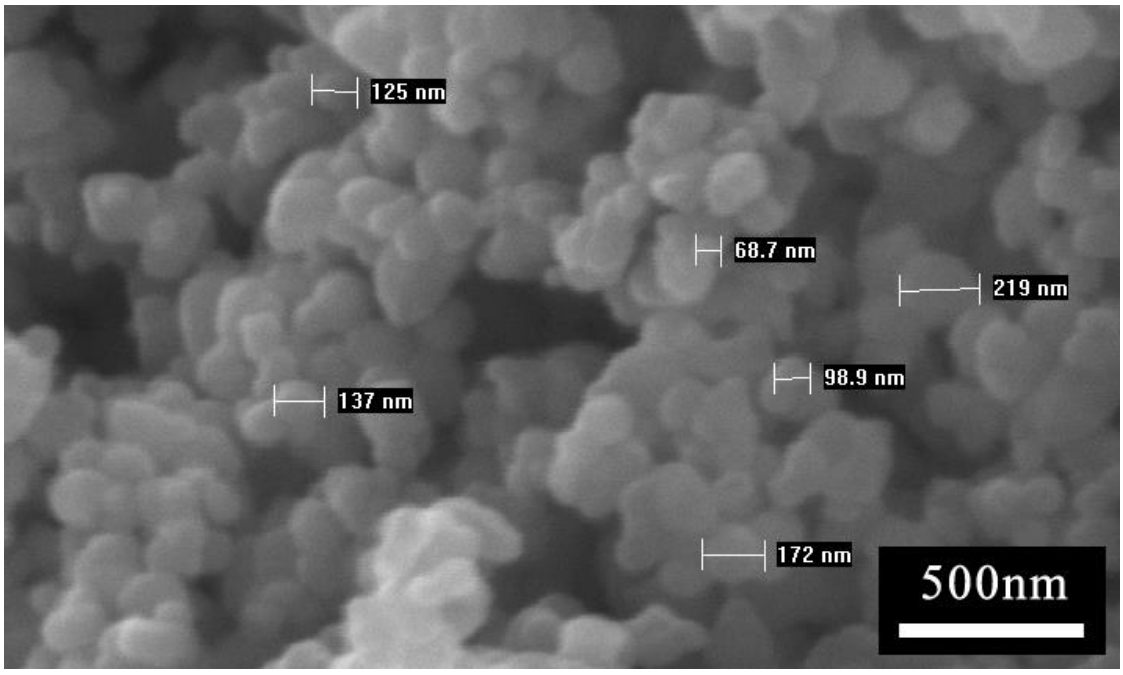

A-Fig. 18 Morphology of TiO_2 powder by SEM

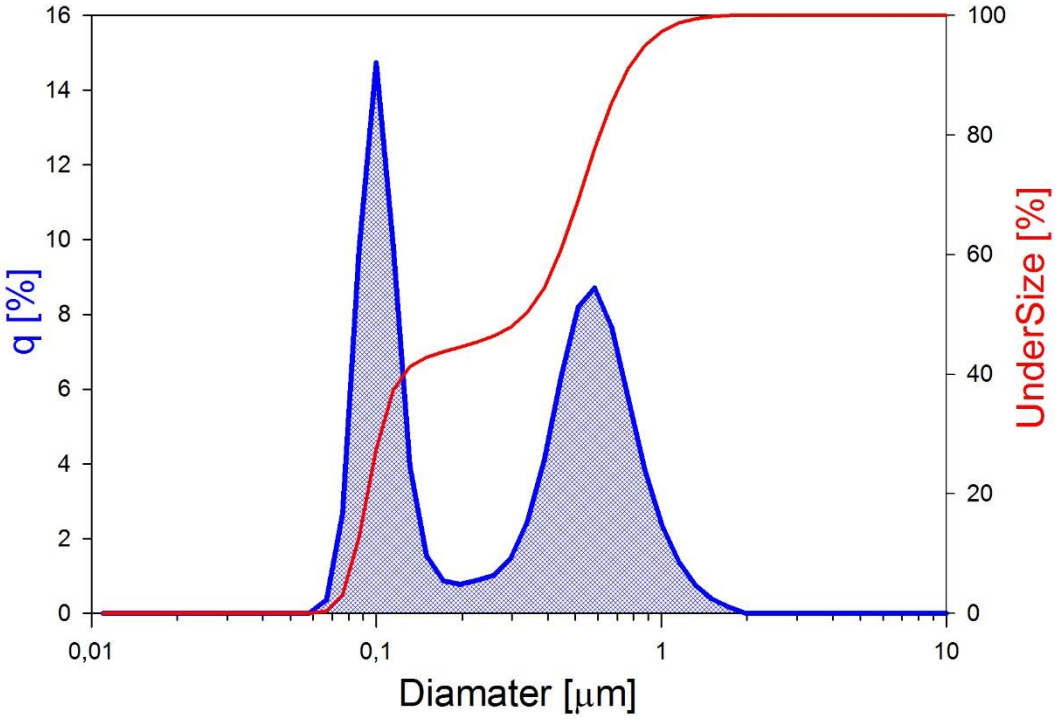

A-Fig. 19 Particle (agglomeration) size distribution of TiO_2 powder established by laser diffraction

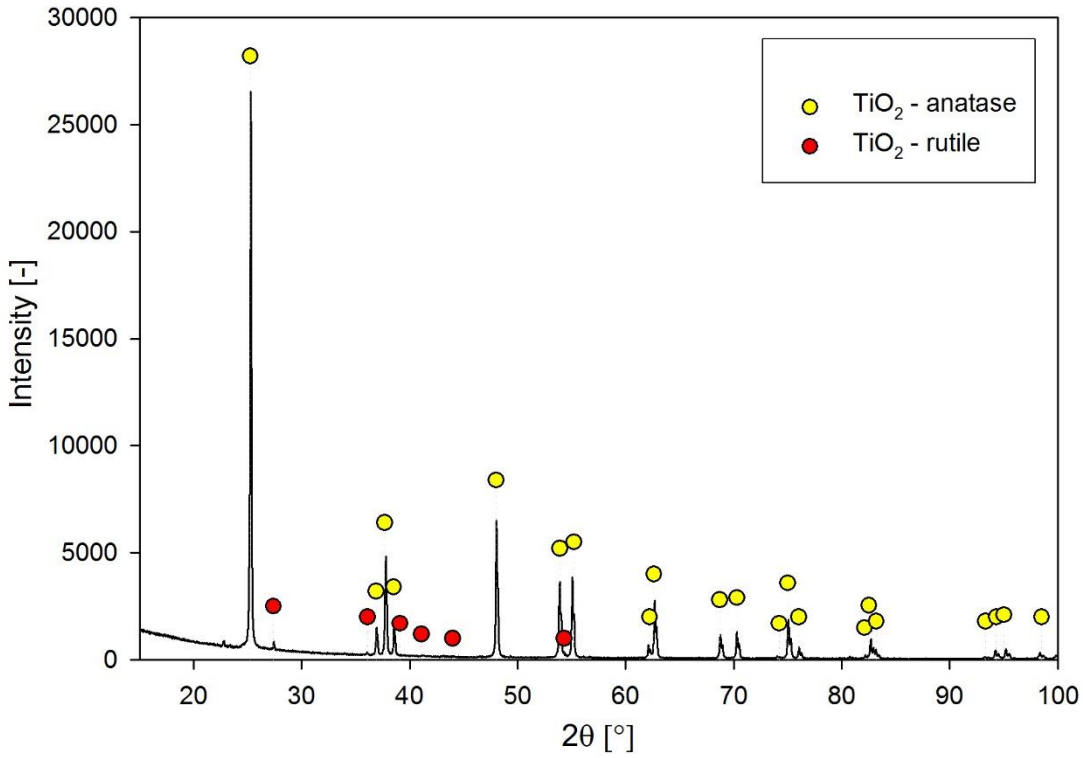

A-Fig. 20 XRD diffractogram of the TiO_2 powder (98 % of anatase and 2 % of rutile, both tetragonal)

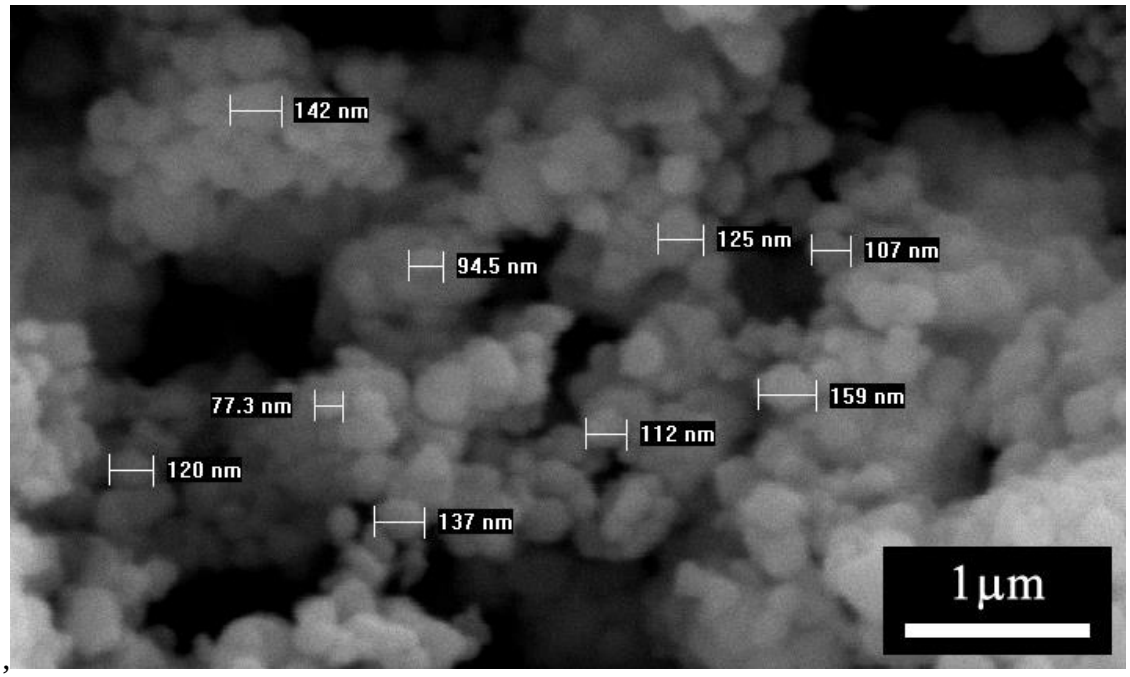

A-Fig. 21 Morphology of ZrO_2 powder by SEM

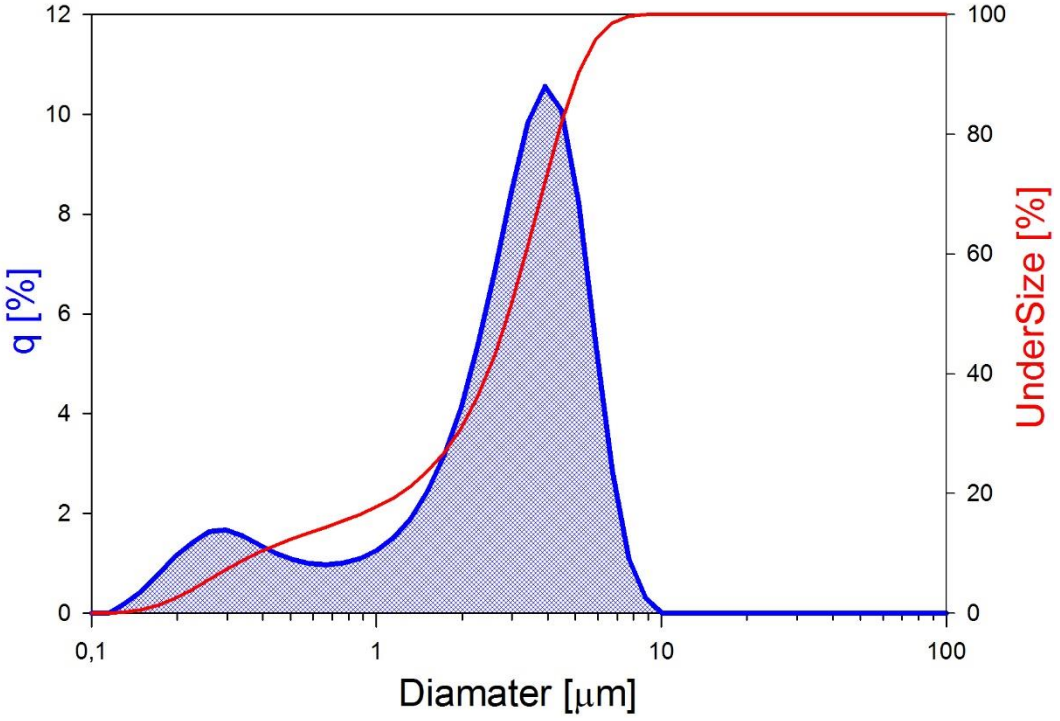

A-Fig. 22 Particle (agglomeration) size distribution of ZrO_2 powder established by laser diffraction

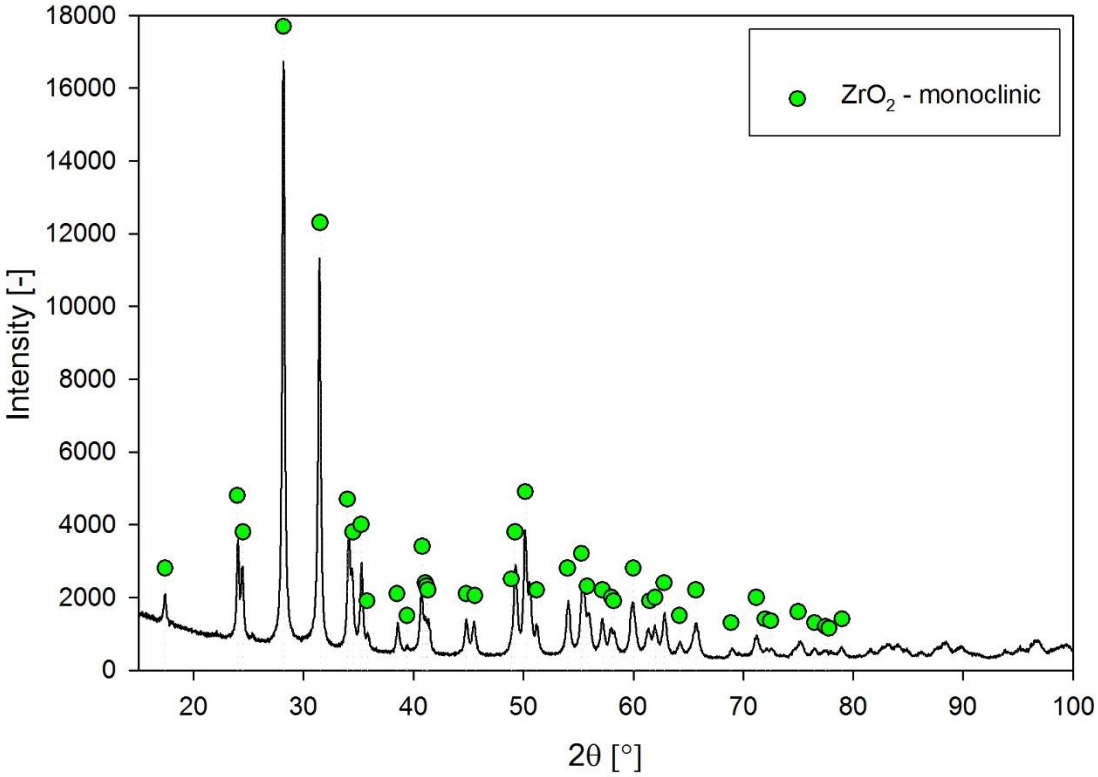

A-Fig. 23 XRD diffractogram of the single phase powder - monoclinic ZrO_2

List of abbreviations

AC – alternative current
CIP – Cold isostatic press
DC – direct current
EDX – Energy-Dispersive X-ray spectroscopy
ETO – Europium titanate
HIP – Hot isostatic press
HT – Hydrothermal
HTS – Hydrothermal synthesis
IR – Infrared
LD – Laser diffraction
ME – Magnetoelectric
MIX – Mixture
PA – Polyamide
RAM – random access memories
SEM – Scanning electron microscopy
SPS – Spark plasma sintering
TD – Theoretical density
TSS – Two-step sintering
UP – Uniaxial press
XRD – X-ray diffraction

List of figures

List of tables